Theses and Dissertations

Summer 2019

Bifacial photovoltaic (PV) system performance modeling utilizing ray tracing

Amir Asgharzadeh Shishavan
University of Iowa

BIFACIAL PHOTOVOLTAIC (PV) SYSTEM PERFORMANCE MODELING UTILIZING

RAY TRACING

by

Amir Asgharzadeh Shishavan

A thesis submitted in partial fulfillment
of the requirements for the Doctor of Philosophy
degree in Electrical and Computer Engineering in the
Graduate College of
The University of Iowa

August 2019

Thesis Supervisor: Assistant Professor Fatima Toor

To my wife, Sima,

who has always supported and encouraged me.

ABSTRACT

Bifacial photovoltaics (PV) is a promising technology which allows solar cells to absorb light and generate power from both front and rear sides of the cells. Bifacial PV systems generate more power per area compared to their monofacial counterparts because of the additional energy generated from the backside. However, modeling the performance of bifacial PV systems is more challenging than monofacial systems and industry requires novel and accurate modeling tools to understand and estimate the benefit of this technology. In this dissertation, a rigorous model utilizing a backward raytracing software tool called RADIANCE is developed, which allows accurate irradiance modeling of the front and rear sides of the bifacial PV systems. The developed raytracing model is benchmarked relative to other major bifacial irradiance modeling tools based on view-factor model. The accuracy of the irradiance models is tested by comparing with the measured irradiance data from the sensors installed on various bifacial PV systems. Our results show that the raytracing model is more accurate in modeling backside irradiance compared to the other irradiance models. However, this higher accuracy comes at a cost of higher computational time and resources. The raytracing model is also used to understand the impact of different installation parameters such as tilt angle, height above the ground, albedo and size of the south-facing fixed-tilt bifacial PV systems. Results suggest bifacial gain has a linear relationship with albedo, and an increasing saturating relationship with module height. However, the impact of tilt angle is much more complicated and depends on other installation parameters. It is shown that larger bifacial systems may have up to 20º higher optimum tilt angle compared to small-scale systems. We also used the raytracing model to simulate and compare the performance of two common configurations for bifacial PV systems: optimally tilted facing south/north ($Bi_{S/N}$) and vertically installed facing east/west ($Bi_{E/W}$). Our results suggest that in the case of no nearby

obstruction, $Bi_{S/N}$ performs better than $Bi_{E/W}$ for most of the studied locations. However, the results show that for high latitude locations such as Alaska, having a small nearby obstruction may result in having better yield for vertical east-facing system than south-facing tilted system. RADIANCE modeling tool is also used in combination of a custom tandem device model to simulate the performance of tandem bifacial PV systems. Modeling results suggest that while the energy gain from bifacial tandem systems is not high, range of suitable top-cell bandgaps is greatly broadened. Therefore, more options for top-cell absorber of tandem cell are introduced.

PUBLIC ABSTRACT

Conventional solar panels generate power due to light received only from their frontside. A promising technology called bifacial photovoltaics (PV) enables solar panels to generate power from both sides. As a result, bifacial PV solar panels produce more power per area compared to their monofacial counterparts. In this work, a raytracing model which allows accurate performance modeling of bifacial PV systems is presented. The model is validated by comparing the modeled values to outdoor measured data from various test sites. These results showed that our raytracing model has a higher accuracy than other available models in the industry. This model is also used to study the performance of bifacial PV systems under different installation conditions and configurations and the optimum installation parameters are derived based on this study.

TABLE OF CONTENTS

LIST OF TABLES

LIST OF FIGURES

1   INTRODUCTION

1.1   Motivation

Bifacial photovoltaic (PV) is a promising technology based on the utilization of both front and back sides of solar cells for light absorption. The major advantage of this technology is the higher energy yield per square meter of the PV modules [1]. Bifacial gain in energy (BGE) is a measure to calculate the additional energy a bifacial system generates compared to its monofacial counterpart and is calculated by the following equation:

$$BGE = \frac{E_b}{E_m} - 1 \qquad (1.1)$$

E_b: Energy yield of bifacial system

E_m: Energy yield of equivalent monofacial system

A wide range of bifacial gains have been reported for bifacial PV systems which stems from various system configurations, module types, ground albedo and other installation parameters. Reise *et al.* reported an annual bifacial gain of 5% to 15% for large commercial systems. [2] Modeling results by Yusufoglu *et al.* suggested that a bifacial gain of 5% to 25% is achievable. The world's first one megawatt bifacial PV power plant "Hokuto" in a snowy area in Japan showed a bifacial gain of almost 20% in 32 months of operation. [3] The importance of bifacial PV technology is easily perceptible by the bifacial gain values reported in these works.

Fabrication of bifacial solar cell and modules have become easier by introduction of new PV cell structures such as Passivated Emitter and Rear Cell (PERC), Passivated Emitter Rear Totally Diffused (PERT), and heterojunction (HJT) solar cell. These structures have open back contacts and only small additional cost is required to manufacture bifacial cells compared to traditional monofacial solar cells. These structures will be discussed in section 2.3.

1

Figure 1.1 illustrates the U.S. Department of Energy (DOE) SunShot goals until year 2030 [4]. The goals have been set to achieve 5 ¢/kWh, 4 ¢/kWh, and 3 ¢/kWh for residential, commercial, and utility scale systems, respectively by 2030. The determination to lower the levelized cost of energy (LCOE) have made bifacial PV technology one of the most favorable approaches to meet the SunShot goals [5].
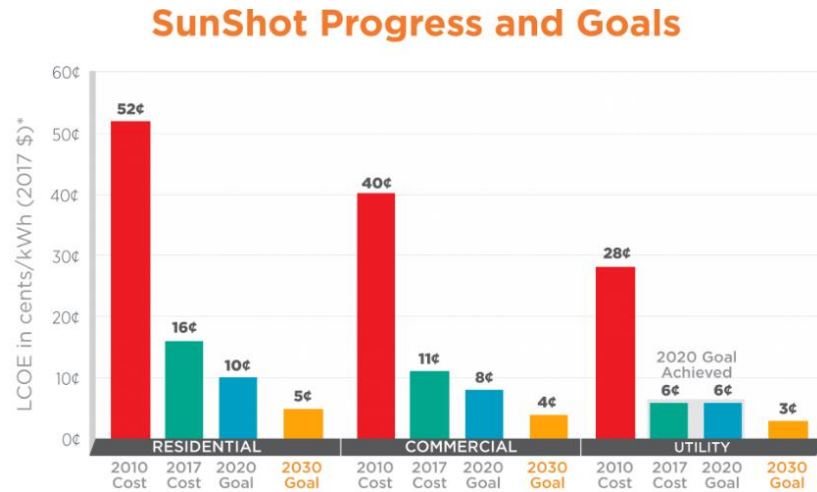
Figure 1.1. U.S. Department of Energy's SunShot goals for residential, commercial, and utility PV systems.

Technoeconomic analysis by Lux Research [6] showed that the bifacial technology provides clear cost reductions to achieve the U.S. DOE SunShot goals (Figure 1.2). In addition to the discussed benefits, the availability of bifacial modules in the market make this technology a good candidate rather than newer PV cell technologies to meet the SunShot goals in time.

2
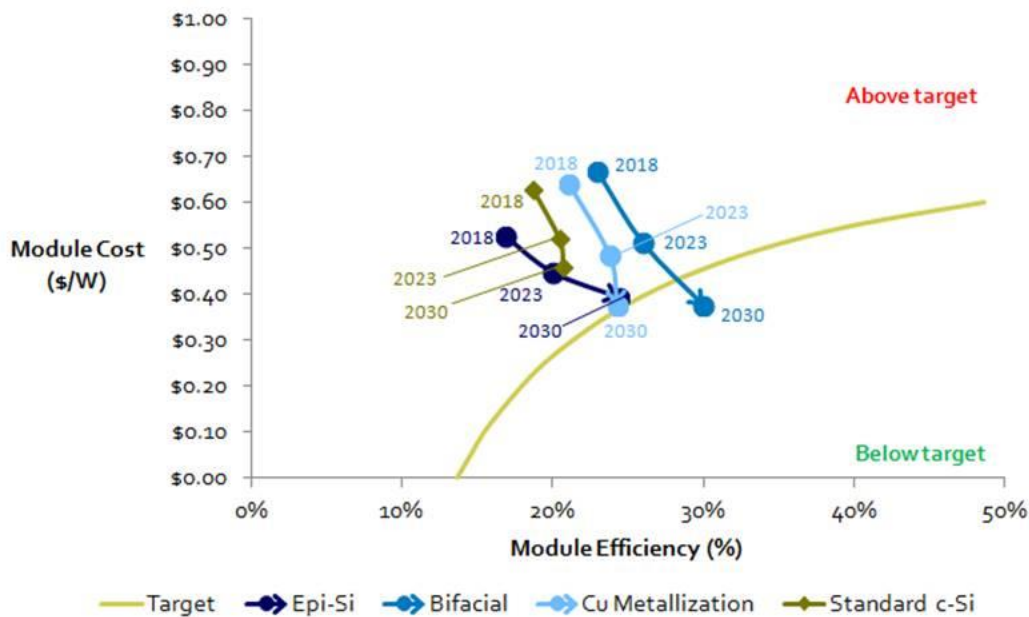
Figure 1.2. The low-cost advantage of bifacial PV systems with regards to SunShot cost targets.

By the end of 2017, the global installed bifacial PV capacity was around 1 GW [7]. The 2019 International Technology Roadmap for Photovoltaic (ITRPV) published by VDME predicts that the market share of bifacial modules will increase to more than 50% in 2029. [8]

Bifacial technology is growing fast. Major PV manufacturers have increased their investment in bifacial products. On the modeling side, many bifacial performance modeling tools have been developed or are under development. Bifacial workshops and conferences are held regularly, and the cutting-edge findings are presented. All these examples suggest that the PV industry is entering into a new era where bifacial systems will play an increasingly important role.

1.2 Objective of the Study

This work is funded by the SunShot National Laboratory Multiyear Partnership (SuNLaMP) program and is a collaborative work among Sandia National Laboratories, National Renewable Energy Laboratory (NREL) and the University of Iowa to remove the barriers for the growth of bifacial PV technology by assessing factors important to outdoor performance of bifacial

3

PV modules and systems, developing international standards for bifacial module characterization, and developing and validating computer modeling tools for estimating the performance characteristics of bifacial PV systems. The focus of this thesis is on the modeling of bifacial PV systems, validating such models and investigating the effect of multiple parameters on the performance of bifacial PV systems.

1.3   Dissertation Outline

Chapter 2 provides an overview on the fundamental operational mechanisms of the PV effect, solar PV cells and modules. Bifacial PV technology is next introduced and the differences between bifacial and monofacial PV cells and modules are discussed. Next, different installation options for utility-scale bifacial PV systems are shown. Finally, irradiance and weather data which are required for modeling the performance of PV systems are discussed.

In chapter 3, the challenges and obstacles for bifacial PV system modeling are discussed. Later in this chapter methods for irradiance, electrical and temperature modeling of bifacial PV systems are presented, and their characteristics are discussed.

In chapter 4, results of benchmark and validation analyses of four bifacial irradiance models are shown. Two fixed-tilt systems installed at Sandia National Laboratories in Albuquerque, NM, and one single-axis tracking systems at SunPower R&D ranch in Davis, CA are modeled and the measured irradiance data from installed sensors are compared with the modeling results.

Chapter 5 describes parametric simulation results for analyzing the impact of different installation parameters such as tilt angle, height of the system, and albedo on the performance of south-facing bifacial fixed-tilt systems. Optimization of these parameters to gain highest energy yield are shown and the impacts of the system size and weather conditions are discussed.

4

In chapter 6, a comparative study between vertical east/west facing and tilted south-facing bifacial PV systems for a few locations with different weather conditions around the world is shown. Next, the impact of nearby-object shading on this comparison is presented and the conditions in which one installation option outperforms the other is discussed.

In chapter 7, a spectrally resolved irradiance modeling method utilizing RADIANCE simulation software is presented. Higher resolution irradiance modeling is used in modeling tandem bifacial PV systems and benefit of such technology is discussed.

5

2   BACKGROUND

2.1   Conventional Solar Cell Structure and the Photovoltaic (PV) Effect

A solar cell is a device which absorbs the incident light (photons) to generate electricity. Solar cells are composed of organic or inorganic semiconductor materials (for example, silicon (Si), cadmium telluride (CdTe), copper indium gallium (di)selenide (CIGS), perovskite, among others) as the base material and Si is the most common semiconductor material for commercial PV cells and modules. If the energy of the absorbed photon is higher than of the band gap of the solar cell material, electrons are raised to a higher energy state and electron-hole pairs are generated.

To avoid recombination of the electron and hole pairs (which results in generating no current), these carries need to be collected using a p-n junction structure. A p-n junction is an interface between two types of semiconductor materials (p-type which has an excess of holes) and n-type (which has an excess of electrons). The electric field in such an interface keeps the carriers separated and prevents electron-hole recombination.

The more abundant and less abundant carriers in a semiconductor material are referred to as majority and minority carriers, respectively. For example, in a n-type material, electrons are majority carriers and holes are minority carriers. In a solar cell, after creation of the electron-hole pair, the minority carrier crosses the p-n junction interface (and becomes a majority carrier). However, the generated majority carrier flows in the external circuit and rejoins its pair in the cell and completes a circuit. Figure 2.1 shows the operation schematic of a p-type solar cell where majority carrier (electron in this case) flows in the external circuit and generates current.

6
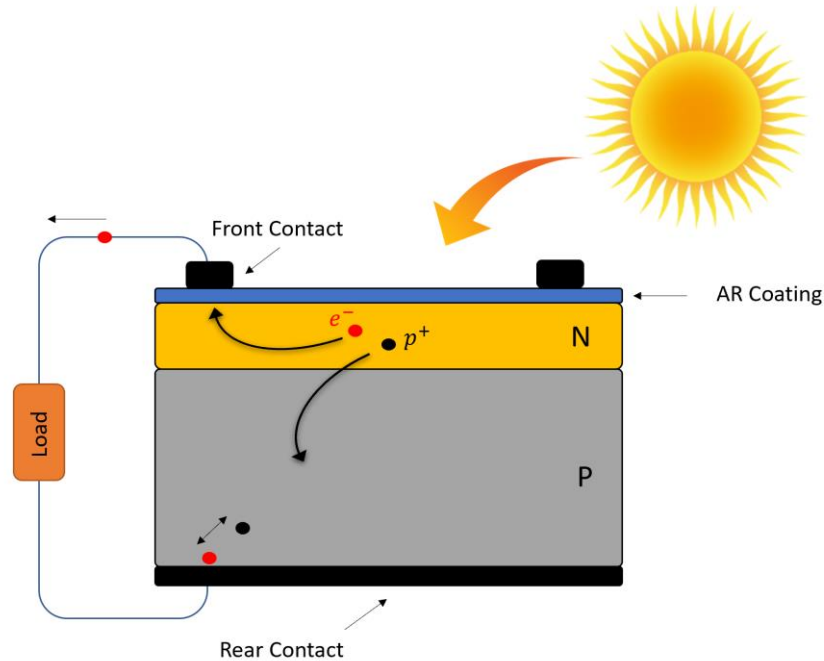
Figure 2.1. Solar cell operation for a p-type solar cell.

The operation discussed earlier is for an ideal solar cell. However, in real solar cells not all the generated electron-hole pairs contribute to the light-generated current. The probability that a carrier is collected by a p-n junction is called the collection probability which depends on the surface properties of the solar cell. This parameter also depends on the diffusion length compared to the distance a carrier needs to travel to generate current. The generated current density is given by the following equation.

$$J_L = q \int_0^W G(x)CP(x)dx \qquad (2.1)$$

J_L: light-generated current density

q: electron charge

W: thickness of the device

G(x): arbitrary generation rate

CP(x): collection probability

Arbitrary generation rate (G(x)) itself can be calculated as:

7

$$G(x) = \int a(\lambda)H_0\, e^{(-a(\lambda)x)}d\lambda \qquad (2.2)$$

a (λ): absorption coefficient which depends on the wavelength

H_0: number of photons at each wavelength

    A few methods are used to reduce reflection of the light from the surface of the solar cell. Without any modification solar cell will reflect a considerable amount of light. For example, bare Si has a high surface reflectance of 30 – 70 % [9] in the solar spectrum and absorbs a small fraction of the light. Using an anti-reflecting (AR) coating as a top layer of the cell [10] or modifying the surface texture will diminish the reflection off the solar cell surface significantly. An AR coat is a thin layer of a dielectric material (silicon nitride). Refractive index and the thickness of the layer is chosen such that the reflected light from the surface of the AR layer destructively interacts with the reflected light from the interface of AR and the semiconductor surface and hence reduces the total reflection to near zero. Figure 2.2 shows a schematic of the impact of AR coating on reducing the total reflection from the surface of a solar cell.
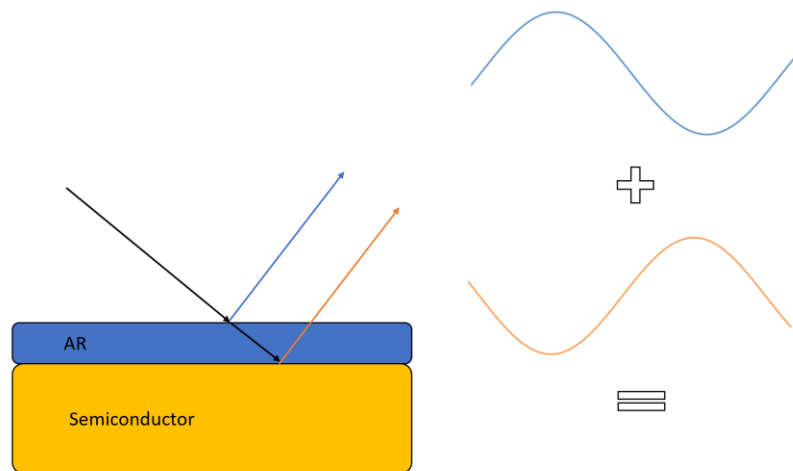
Figure 2.2. Impact of anti-reflecting coating in reducing the total reflection from the surface of a solar cell.

Another method for reducing the reflection from the surface of a solar cell is modifying the surface texture of the solar cell. It is known that by roughening the surface of any material, its surface reflectivity decreases. The reason is that reflected light from a rough surface has a higher possibility to bounce back into surface and get reabsorbed. Figure 2.3. shows examples of surface textures used in solar cells such as pyramid-texture [11], and inverted-pyramid texture [12, 13].

(a)　　　　　　　　　　　　　　　(b)
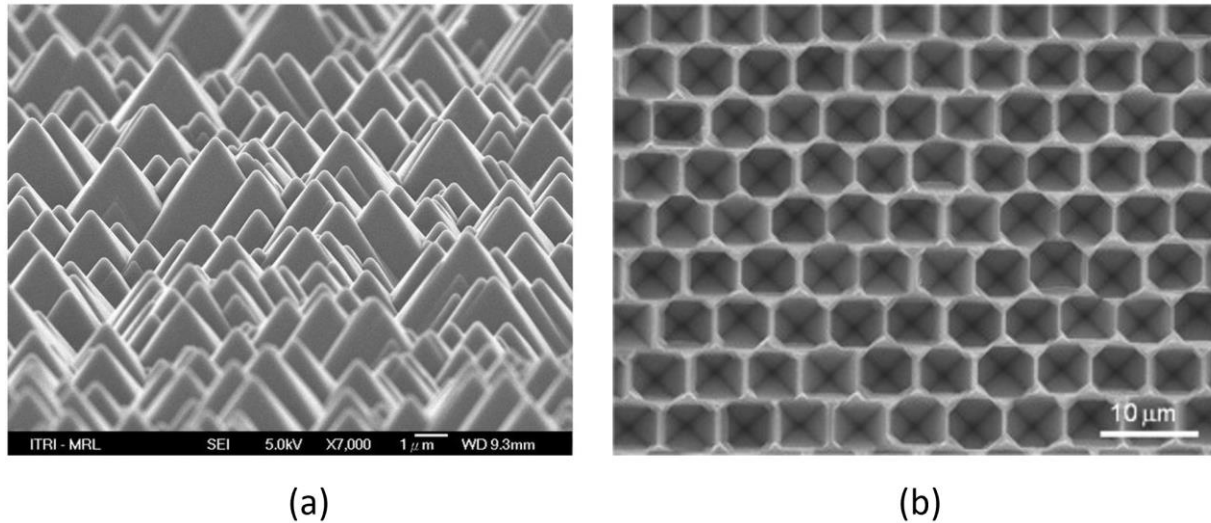
Figure 2.3. Scanning electron microscope (SEM) images of (a) pyramid [14] and (b) inverted-pyramid [15] surface texture of silicon wafers.

2.2   Conventional PV Modules Structure

PV Modules are comprised of electrically interconnected solar cells. To protect thin solar cells from mechanical damage, water ingress and corrosion, they are generally encapsulated between two layers (either glass and polymer backsheet or glass-glass). The most common material for the encapsulant is ethylene vinyl acetate (EVA).

PV modules have different sizes and nominal powers and are installed at residential, commercial and utility scales. The most common crystalline silicon (c-Si) PV modules include 60 (10×6), 72 (12×6), and 96 (12×8) cells connected in series. Figure 2.4 shows an example of a common 60-cell module configuration.

9

Most conventional PV modules contain a white opaque polymer backsheet, which reflects the transmitted light through and around the cells (which is not absorbed by cells) back to the solar cells and hence results in higher generated power in the modules. However, some modules use a black backsheet to create a uniform dark module, which is preferred for some aesthetic applications.
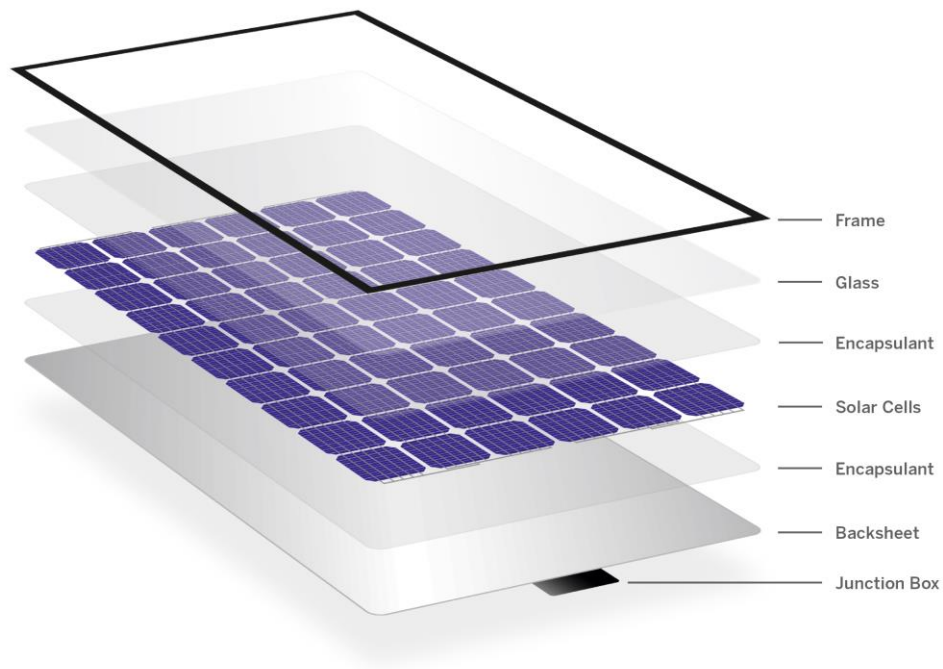
Figure 2.4. Conventional 60-cell PV module structure with opaque backsheet. (Figure from www.blog.ibc-solar.com).

In PV modules, shading or uneven illumination is common. It can occur from row-to-row shading, nearby structures or trees, or even from a fallen leaf or bird droppings on the module surface. Shaded cells produce lower power and can limit the current in the entire module (since cells in common PV module are connected in series). Furthermore, the extra energy generated by the high-performing cells can be released in the shaded, low-performing cell and can increase the temperature of the cell significantly and therefore can accelerate the material degradation over

10

time and damages the cells and other module materials. This effect is called hotspots. To avoid hotspots and reduction of the power from the entire module (due to one or more shaded, low-generating cells), bypass diodes are installed within each module. If cells are shaded, the bypass diode in that part of the module is activated and removes the low-performing cell string from the circuit. Ideally, bypass diodes should be installed for each cell. However, to keep the price of the modules low, only a few bypass diodes are typically installed per module, covering sub-strings of series connected cells. Figure 2.5 shows hot-spots captured by an IR camera in a PV system. Figure 2.6 shows two examples of cell damage related to a hotspot on a PV module. However, it will take further study to identify if this is a specific issue for bifacial systems.
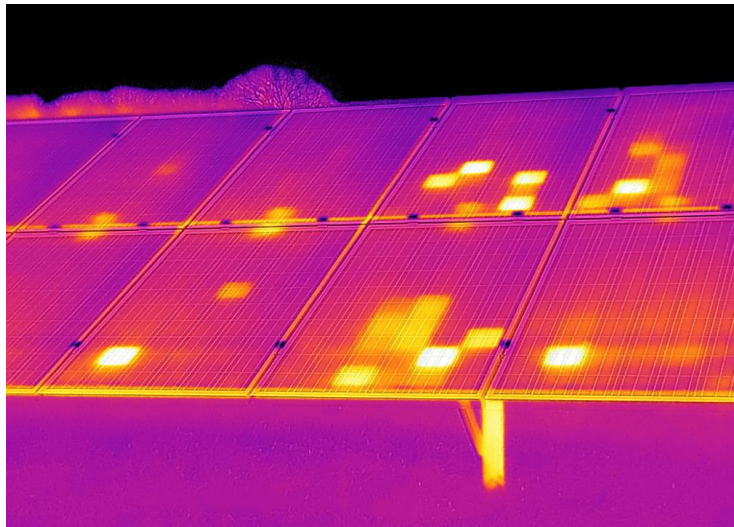
Figure 2.5. Hotspots on the PV Modules captured by an infrared camera. (Figure from www.monroeinfrared.com).

11
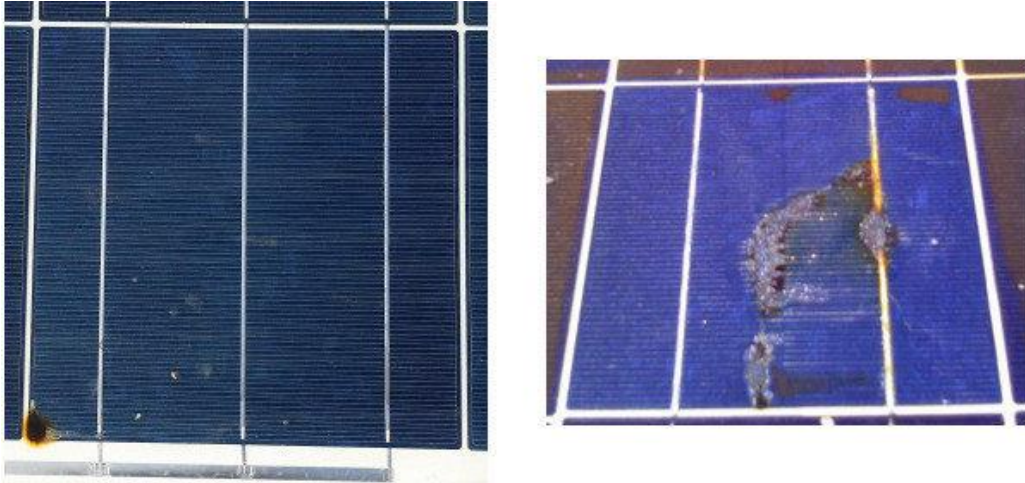
Figure 2.6. Examples of cell damage related to a hotspot on a PV module. (Figures from DNV GL and Dupont)

Figure 2.7 shows and example of a 60-cell module circuit with 3 bypass diodes. Each bypass diode covers two columns of series connected cells. Normally, the diodes are in reversed bias and have minimal impact on the module operation. If the occurrence of shading is extensive enough, then the bypass diode switches into the forward bias and conducts current and therefore bypasses the group of 20 cells.
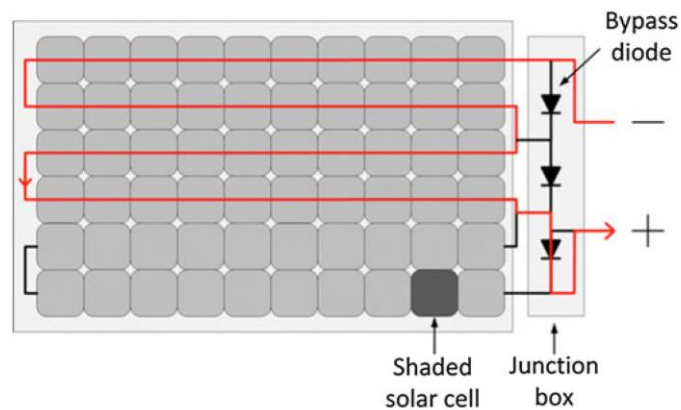
Figure 2.7. Shaded cell in the sub-string causes the bypass diode to be activated and the module loses the power from the cells in this sub-string and avoids hot-spot creations. [16]

2.3 Bifacial PV Technology, Cells and Modules

Bifacial PV [5] is a promising technology which allows solar cells to absorb light from the front and backside simultaneously. With a small cost increase resulting from modifying the solar cell and module structure, bifacial solar modules produce more power compared to their monofacial counterparts.

Bifacial solar cell's front design is usually same as monofacial solar cell. However, rear side structure is different. The main difference is the surface rear contact. In monofacial solar cells as shown in Figure 2.8 aluminum rear contact covers the entire backside of the module. However, in bifacial solar cells, a finger grid is used to allow the light onto the backside of the surface of the cell.
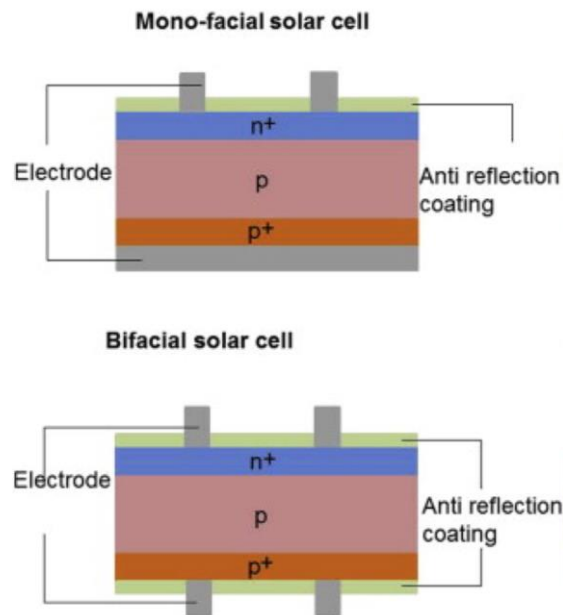
Figure 2.8. Standard monofacial and bifacial solar cell structures. [17]

Newer PV cell designs utilizing Passivated Emitter and Rear Cell (PERC) and Heterojunction (HJT) technologies are relatively easy to make bifacial due to their open back contacts. New techniques for implementing these technologies have allowed bifacial solar cells to achieve high efficiencies which are comparable to traditional monofacial solar cells. [18] Figure

13

2.9 shows four examples of such bifacial solar cell structures. Passivated Emitter and Rear Cell (PERC) technology utilizes a back-surface passivation layer and improves light capture near the rear surface and hence has higher efficiency compared to standard cell. [19] Passivated Emitter Rear Totally Diffused (PERT) cell technology uses a diffused rear surface and promises high and stabilized conversion efficiencies. [20] Unlike PERT, in Passivated Emitter with Rear Locally diffused (PERL) cells, the rear is locally diffused only at the metal contacts. In heterojunction solar cell (HJT), the highly recombination-active contacts are displaced from the crystalline surface by insertion of a thin film with a high band gap (usually hydrogenated amorphous silicon a-Si films are used in this cell structure).
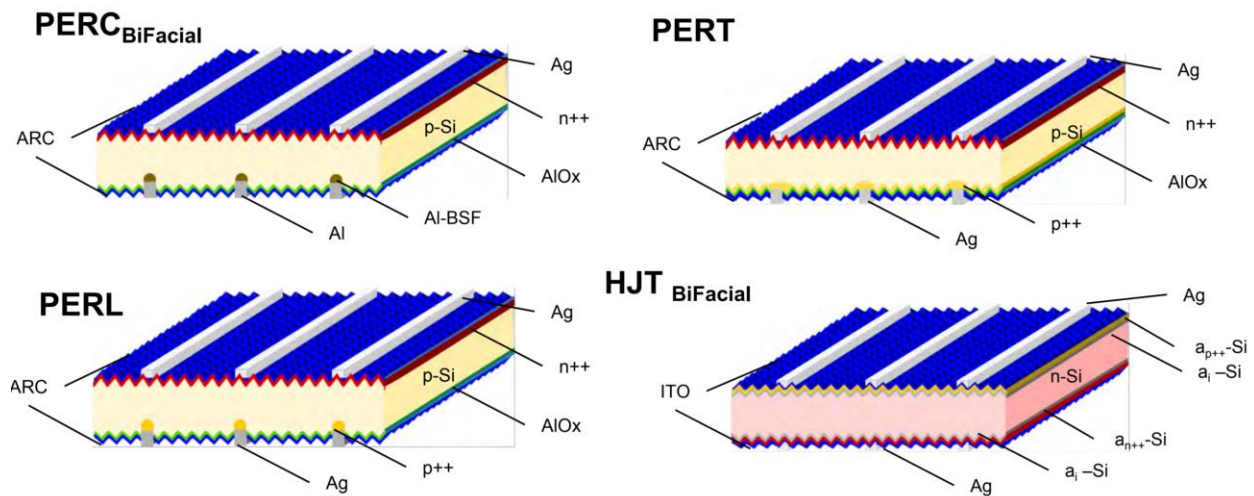
Figure 2.9. Four examples of bifacial solar cell technologies in the PV market: Passivated Emitter and Rear Cell (PERC), Passivated Emitter Rear Totally Diffused (PERT), Passivated Emitter with Rear Locally diffused (PERL), and Heterojunction (HJT) solar cells. [21]

In addition to solar cells, there are differences between the conventional (monofacial) and bifacial PV modules. Monofacial PV modules have opaque backsheets and are only able to absorb the light from the front side. On the other hand, bifacial PV modules, make use of glass-glass structure or transparent backsheets. Figure 2.10 shows the monofacial and bifacial PV systems and modules. As shown, some of the bifacial PV modules have no frame and hence cuts down the

14

material cost for the module. However, installation and handling of frameless modules requires higher effort and the cost savings in module materials may be offset by higher installation costs.
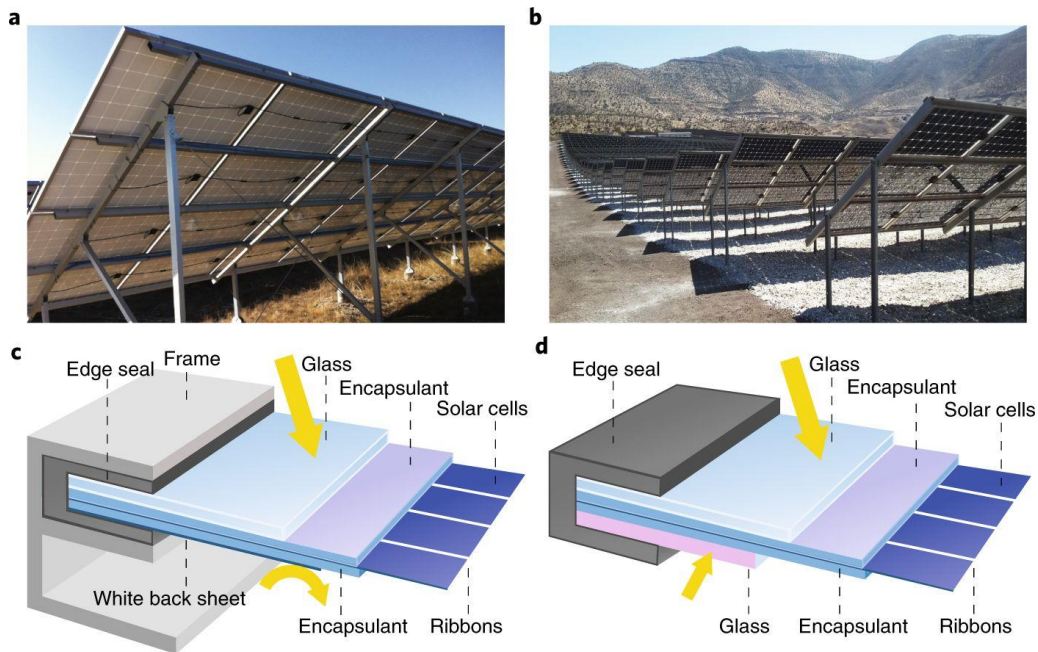
Figure 2.10. (a) Monofacial PV system, (b) bifacial PV system, (c) monofacial solar cell structure, (d) bifacial solar cell structure. [7]

Even though bifacial PV modules receive light from the both sides, the efficiency of the frontside and backside is not same. Backside efficiency is usually lower than the frontside efficiency. The *bifaciality factor* is calculated as the ratio of the backside power to the frontside power measured at standard test conditions (STC) (1000 W/m^2 and 25° C).

$$bifaciality\ factor = \frac{Rearside\ Power\ at\ STC}{Frontside\ Power\ at\ STC} \qquad (2.3)$$

The bifaciality factor is different for different module technologies. Passivated Emitter and Rear Contact (PERC), Passivated Emitter Rear Totally Diffused (PERT), and Heterojunction with Intrinsic Thin layer (HIT) bifacial PV modules can have a bifaciality more than 70, 90, and 95 %. [22]

2.4   PV Systems Configurations

PV systems including monofacial and bifacial PV systems are installed in different orientations. Fixed-tilt orientation is a very common installation option for both commercial monofacial and bifacial systems. In this configuration, PV arrays are tilted at a fixed angle and are installed with their front sides facing the equator (south facing for north hemisphere sites and north facing for south hemisphere sites). The tilt angle is usually chosen to maximize the annual energy yield of the system. A few studies have been conducted to calculate the accurate optimum angle for the fixed-tilt systems. Chang et. al. [23] and Talebizadeh [24] showed that there is a linear relationship between the optimum tilt angle and latitude. Jacobson, et. al. [25] showed that while the linear relationship is accurate for mid-latitude sites, it diverges for high latitudes in the Northern hemisphere. They suggested a third order polynomial fit function of latitude to calculate the optimum angle for fixed-tilt systems. The optimum tilt angle for bifacial systems is different than monofacial systems and will be discussed in chapter 5 in more details. Figure 2.11 shows an example of fixed-tilt carport system installed on campus of the University of Iowa.
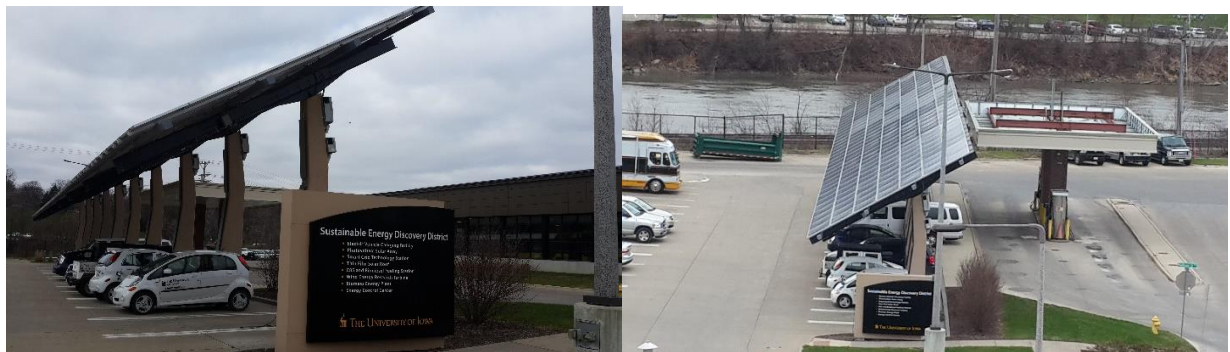
Figure 2.11. An example of fixed-tilt carport system installed on campus of the University of Iowa.

Single-axis tracking (SAT) is another common installation configuration for PV systems. As implied by its name, there is only one axis of rotation for such systems. The rotation axis can be horizontal, tilted angle or vertical. Horizontal single-axis tracking oriented along North-South

is the most common configuration among SAT system. In this configuration, PV modules face east in the morning then become flat during solar noon and then face west in the afternoon. Defined tracking algorithms in the system's controller governs what the tracking angle should be at each timestamp. Figure 2.12 shows an example of a bifacial single-axis tracking system.

Figure 2.12. An example of a bifacial single-axis tracking PV system. (Image from www.NEXTracker.com)

There are two major tracking algorithms for SAT systems; true-tracking and back-tracking algorithms. In true-tracking, the tracking angle is calculated only considering the relative Sun position. If the ground is flat, horizontal and there is no horizon shading, the ideal tracking angle, ω_{ID}, for true-tracking is calculated as following [26]:

$$\tan \omega_{ID} = \frac{x}{z} \quad (2.4)$$

Where x, y, z are the Cartesian coordinates of the Sun vector where points to west, south and zenith, respectively and are defined below:

$$x = \cos \gamma_s \sin \psi_s \quad (2.5)$$

$$y = \cos \gamma_s \cos \psi_s \quad (2.6)$$

17

$$z = \sin\gamma_s \qquad (2.7)$$

Where γ_s, and ψ_s are solar elevation and azimuth angles, respectively. As shown in Figure 2.13 a, true-tracking algorithm results in row-to-row shading during early morning and late afternoon when Sun is low in the sky and the modules are at the highest tracker angle. The length of the shadow, s, and the fraction of the shaded PV row, FS, can be calculated as following:

$$s = \frac{L}{\cos\omega_{ID}} \qquad (2.8)$$

$$FS = \max(0, L\left(1 - \frac{rtr}{s}\right)) \qquad (2.9)$$

Where L is the module length and rtr is the pitch (distance between two PV rows). It is also worthwhile to introduce another parameter called ground coverage ratio (GCR) which shows how compact the trackers have been built and is defined as following:

$$GCR = \frac{L}{rtr} \qquad (2.10)$$

As discussed in section 2.2, even partial shading of a solar cell can result in significant loss in power output of PV modules. Hence, a new tracking algorithm called back-tracking has been developed to avoid row-to-row shading of tracking systems. In addition to avoiding production loss, this algorithm helps to avoid hotspots and therefore damage to the modules. A correction to the ideal tracking angle needs to be made to avoid the row-to-row shading (Figure 2.13 b). Following equation shows the correction angle, ω_C and backtracking angle, ω_{IDC}:

$$\omega_C = \omega_{ID} - \omega_{IDC} \qquad (2.11)$$

$$L\cos\omega_C = rtr\cos\omega_{ID} \qquad (2.12)$$
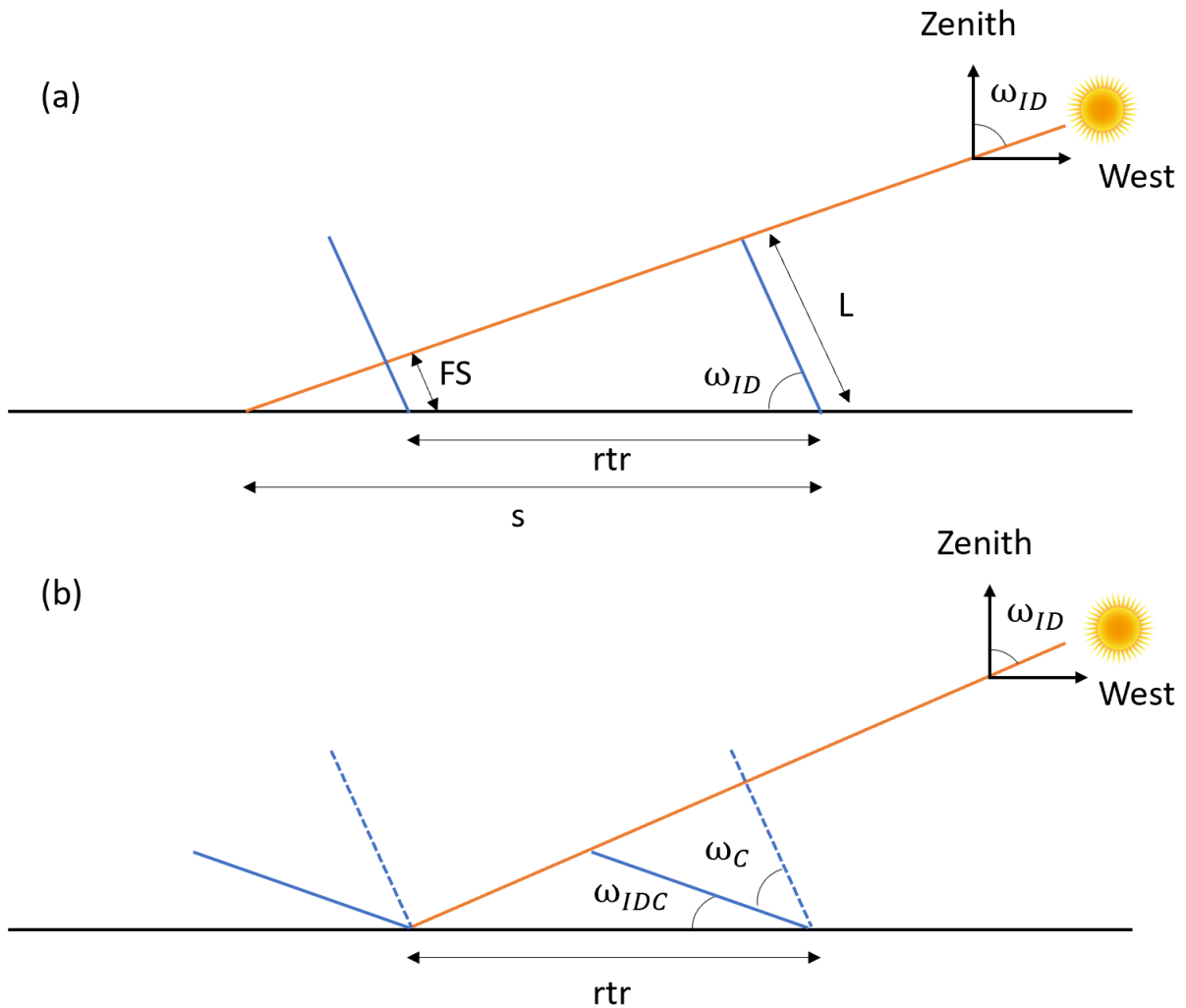
Figure 2.13. (a) Ideal (true-tracking) and (b) back-tracking angle for a N-S horizontal single axis tracker system.

However, it is not practical for solar trackers to rotate to very high angles because it can damage the tracker especially in harsh environment with high wind speed. Therefore, a limit is generally set for the maximum allowed tracking angle, which varies depending on the manufacturer and site conditions. Most common SAT systems have maximum tracking angle of $\pm45°$, $\pm50°$, $\pm60°$.

Two (dual)-axis tracking PV systems have more complex structures and are designed to point directly towards the Sun. This system configuration generally produces the highest energy

19

yield but is costly and large-scale deployment is challenging due to the need for more land area to avoid shading from other trackers.

Figure 2.14. An example of two-axis tracking PV system. (Figure from www. aurorasolarenergy.com)

Installing PV systems vertically is a rising trend and is a good candidate for certain applications such as building integrated PV or as a barrier along roads. This configuration offers benefits such as very low soiling [27] and snow losses. Bifacial PV is also a very good fit for this configuration and large systems with this orientation are being deployed. [28] Figure 2.15 shows a 28 KW vertical bifacial PV system installed in Saarland in Germany.

Figure 2.15. A 28 kW vertically installed bifacial PV system in Saarland, Germany.

20

2.5   Irradiance and Weather Data

Sun position is an essential data for modeling performance of a PV system and is usually described by following parameters and are shown in Figure 2.16:

- Sun elevation angle (θ_{el}): Altitude of the Sun which is the angle between the horizon and the center of Sun's disc.

- Sun zenith angle (θ_z): 90° - Sun elevation angle

- Sun azimuth angle (θ_A): Angle along the horizon which is usually measured from North (e.g., North = 0°, East = 90, South = 180, and West = 270).

θel = elevation angle, measured up from horizon   θz = zenith angle, measured from vertical   θA = azimuth angle, measured from North
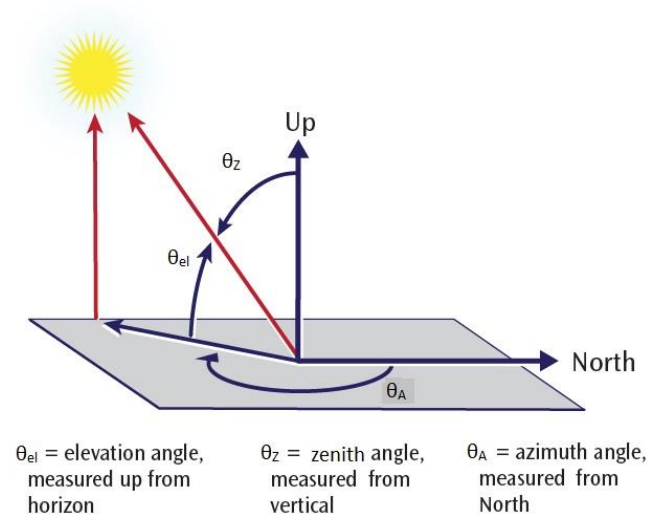
Figure 2.16. Sun position angles. (Figure from www. pvpmc.sandia.gov)

Sun position depends on the geographic location of the observation on Earth's surface (longitude and latitude) and time of the day and year. Figure 2.17 shows Sun path diagrams created by University of Oregon's Sun path chart program [29] for three locations with the same longitude (25°), but with different latitudes: 65 ° (Figure 2.17 a), 35 ° (Figure 2.17 b), and 5 ° (Figure 2.17 c). 65 ° latitude represents a high-latitude location in the northern hemisphere and close to the

21

North Pole. 5 ° latitude is a location in northern hemisphere and close to the Equator and 35 °

latitude is a midway location between previous two locations.
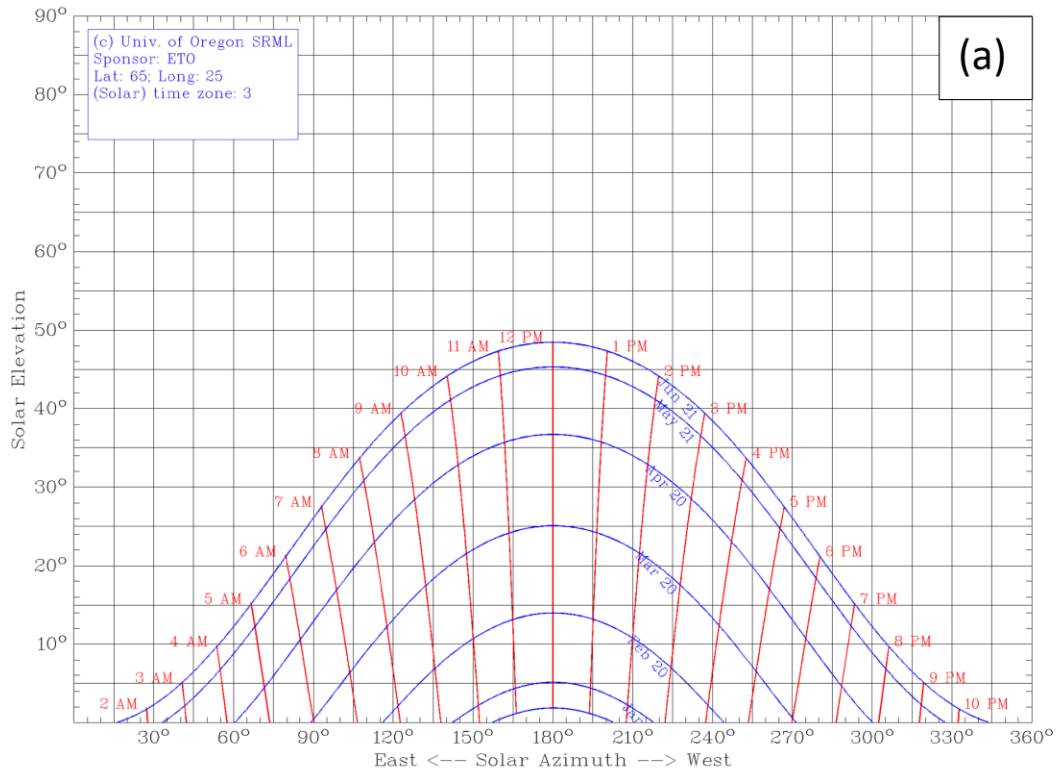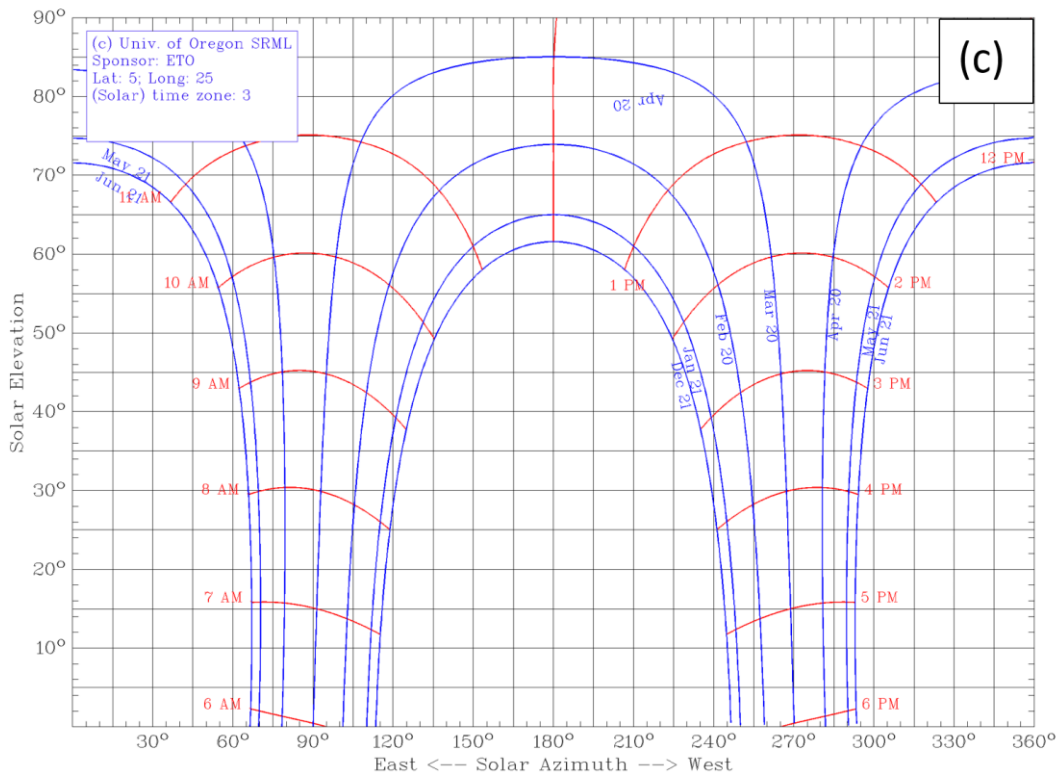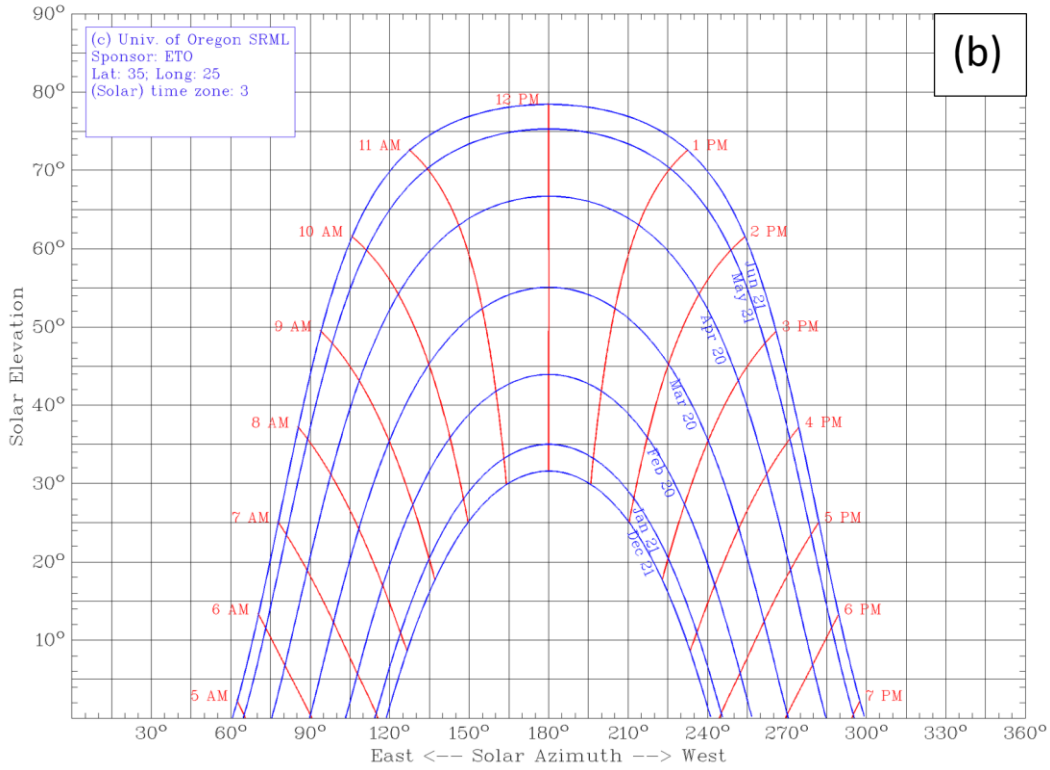
Figure 2.17. Sun path diagrams for three locations: (a) LAT: 65º, LONG: 25 º, (b) LAT: 35 º, LONG: 25 º, LAT: 5 º, LONG: 25 º.

23

As shown in Figure 2.17, for the location near the Equator (latitude of 5 °), Sun has the higher elevation angle compared to the locations farther from the Equator. The highest elevation angle for this location occurs around the two equinoxes (March 20 and September 20). As moving away from the Equator toward North, relative elevation angle of the Sun decreases and the azimuth angle variation range throughout a day (azimuth angle between sunrise and sunset) gets larger.

Air Mass is defined as the normalized path length which light takes before striking the Earth's surface. Normalization was done by dividing the actual path length by the shortest possible path which corresponds to when the Sun is directly overhead. AM quantifies the reduction in the power of the light absorbed by the molecules and dust in the atmosphere. Equation (2.13) shows AM can be calculated as a function of Sun's zenith angle (θ_z):

$$AM = \frac{1}{\cos \theta_z} \quad (2.13)$$

Solar radiation has a large spectrum from UV to deep infrared and this spectrum changes throughout the day and with location. However, standard spectra have been defined in order to compare the performance of PV devices from different manufacturers. Figure 2.18 shows three standards for solar spectrum. AM0 (ASTM E-490) is the standard spectrum for space applications which specifies the extraterrestrial irradiance and has an integrated power of 1366 W/m^2. Two standards are for terrestrial irradiance (ASTM G-173-03). AM 1.5 Global spectrum which has an integrated irradiance of 1000 W/m^2 and is designed for flat surfaces. AM 1.5 Direct and Circumsolar has an integrated irradiance of 900 W/m^2 and includes the direct irradiance from the Sun and the circumsolar irradiance form a 2.5° around the Sun.

24
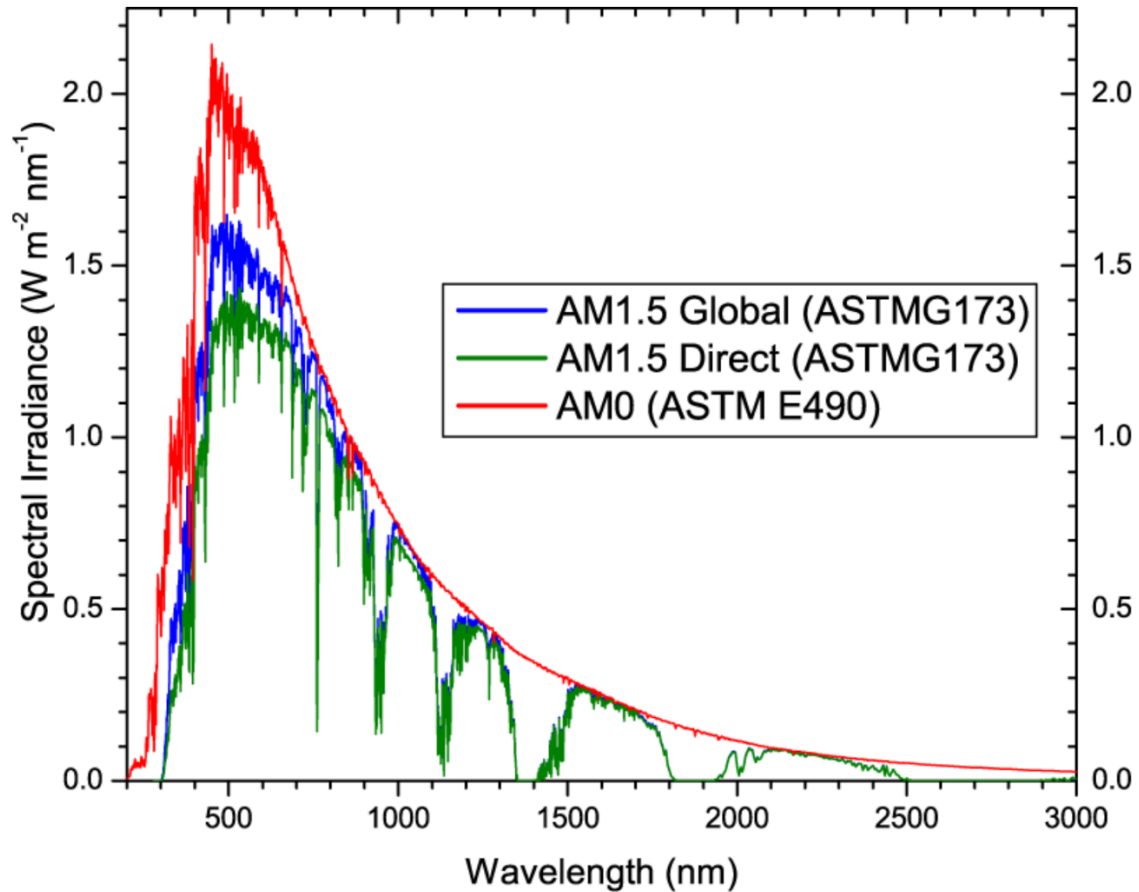
Figure 2.18. Standard extraterrestrial (AM0) and terrestrial (AM1.5 Global and AM1.5 Direct and Circumsolar) solar spectra. (Image from www.pveducation.org)

As shown, the spectral energy distribution of sunlight has a maximum in the visible spectrum and the bandgap of solar cell are designed such that they absorb most of the photons in this region.

Weather data includes time-series values for parameters such as irradiance, temperature, wind direction, and wind speed. Weather data is usually measured by a weather station installed close to the PV system. Acquisition of such data is essential for monitoring and performance modeling of PV systems. Figure 2.19 shows an example of weather stations installed by a PV system in Africa.

Figure 2.19. A SCADA weather station installed in Africa. (Figure from www. geosun.co.za)

Irradiance measurements are usually defined by the following identifiers:

- Global Horizontal Irradiance (GHI)

- Direct Normal Irradiance (DNI)

- Diffuse Horizontal Irradiance (DHI)

GHI is the terrestrial irradiance received by a horizontal surface on the ground. The most common instrument to measure the GHI is pyranometer (Figure 2.20 (a)). Pyranometer has a hemispherical view angle with a cosine response to the incident angle.

DNI is the direct normal irradiance received from the Sun and can be measured by a pyrheliometer (Figure 2.20 (b)). Light enters the pyrheliometer and is directed onto a thermophile which converts heat into an electrical signal.

DHI refers to the diffuse terrestrial irradiance scattered by the atmosphere and received by a horizontal surface. In other words, DHI is the fraction of GHI which does not come from the direct light of the Sun. Therefore, pyranometer can be used to measure DHI. However, in order to remove the beam contribution from the Sun, a ball or disc on a tracker is utilized to shade a 5°

26

field view concentric around the Sun. It is typical to only measure two of these irradiance components and calculate the third using the following relationship:

$$GHI = DNI*\cos(\theta_z) + DHI \quad (2.14)$$
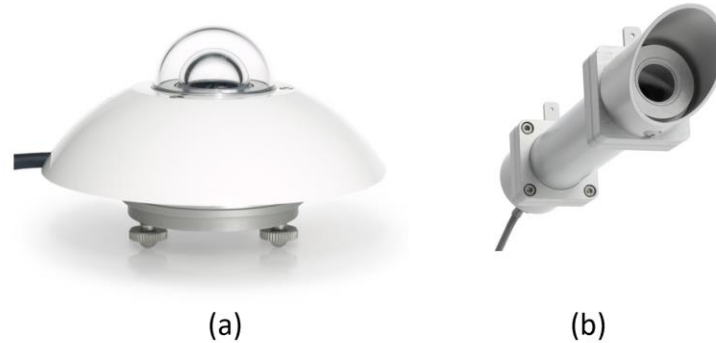
Figure 2.20. (a) Pyranometer and (b) pyrheliometer to measure GHI and DNI, respectively. (Figures from www.hukseflux.com)

One of the commonly used weather data formats for performance modeling of PV systems is typical meteorological year (TMY) data. [30] TMY data contains one year of hourly data (8760 hours) that best represent weather conditions over a multiyear period. In TMY data, measured solar radiation and meteorological data over a usually long period of time (20-30 years) is condensed into one year's worth of the most typical conditions. TMY data are not created simply by averaging the available data. However, special methods are used to create such files by considering solar resource data and weather data. After the analysis of the multiyear data, 12 months that best represent typical conditions are chosen. For example, a TMY developed from a set of data for the years 1998–2014 might use data from 1999 for January, 2013 for February, 2000 for March and so on.

3   BIFACIAL PV SYSTEM MODELING

While bifacial PV is not a new technology and dates back to 1960s [31], its application and market share in the PV industry has remained limited. Lack of accurate and validated models to estimate the energy yield of bifacial systems is one of the major barriers for bifacial technology and it negatively impacts the bankability of bifacial PV systems. Therefore, developing an accurate and valid bifacial PV modeling tool is very crucial to the industry. In this section, challenges for bifacial modeling are discussed and an overview of the major available modeling tools for bifacial systems, their methodology, characteristics, and accuracies are presented.

3.1   Bifacial PV Modeling Challenges

The fact that bifacial PV systems receive light from the backside as well as frontside makes the modeling of such systems more challenging and requires considering parameters that are not pertinent to conventional monofacial PV systems. Therefore, methods used for monofacial PV modeling are no longer valid and more precise tools must be developed.

The irradiance received by a PV surface (front or back) can be discretized into three components as shown in Figure 3.1; Direct irradiance from the Sun, diffuse sky irradiance, and the reflected irradiance from the ground or nearby objects. The challenge for modeling the backside irradiance comes from the fact that the majority of the irradiance on the backside comes from light reflected from the ground. The reflectivity of the ground (albedo) is therefore a critical factor for modeling the backside irradiance and needs to be determined accurately. However, the non-uniformity of the ground due to vegetation, shading from the nearby objects and more importantly shading by the module and its neighbors complicates the modeling approach.

28
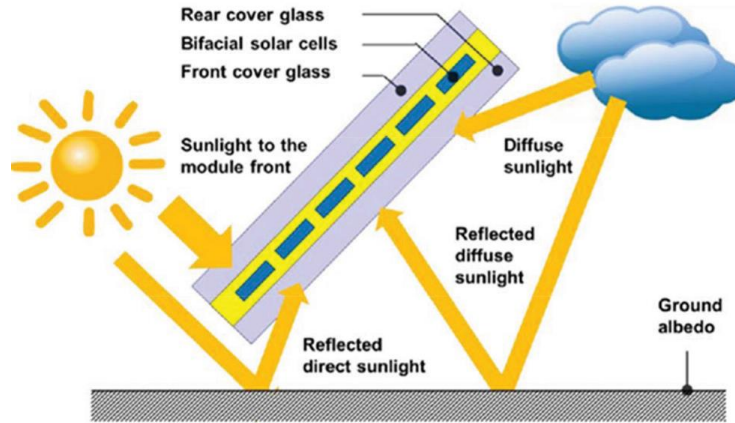
Figure 3.1. Irradiance components received by a bifacial PV module. (Copyright TÜV Rheinland Energy)

Approximated range of albedo for a few natural surfaces are shown in Table 3.1. [32] As shown, albedo range for each surface type is high and hence measured albedo values are needed to perform accurate bifacial PV modeling.

Table 3.1. Approximated range of albedo for a few natural surfaces.

Surface type	Approximated Albedo
Forest	0.05 – 0.2
Grassland and cropland	0.1 – 0.25
Dark-colored soil	0.1 – 0.2
Dry sandy soil	0.25 – 0.45
Dry clay soil	0.15 – 0.35
Sand	0.2 – 0.4
Granite	0.3 – 0.35
Light colored soil	0.4 – 0.5
Dry salt cover	0.5
Fresh deep snow	0.9

Albedo can be measured by an albedometer, which consists of two irradiance sensors. One of the sensors is facing up and measures the downwelling irradiance on the ground from the sky (global horizontal irradiance (GHI)), and the other sensor is facing down and measures the upwelling irradiance reflected from the ground. The ratio of these two readings (upwelling/downwelling) gives the albedo of the ground at each time. The sensor used in the albedometer can be a pyranometer (Figure 3.2 (a)) or a reference cell (Figure 3.2 (b)).
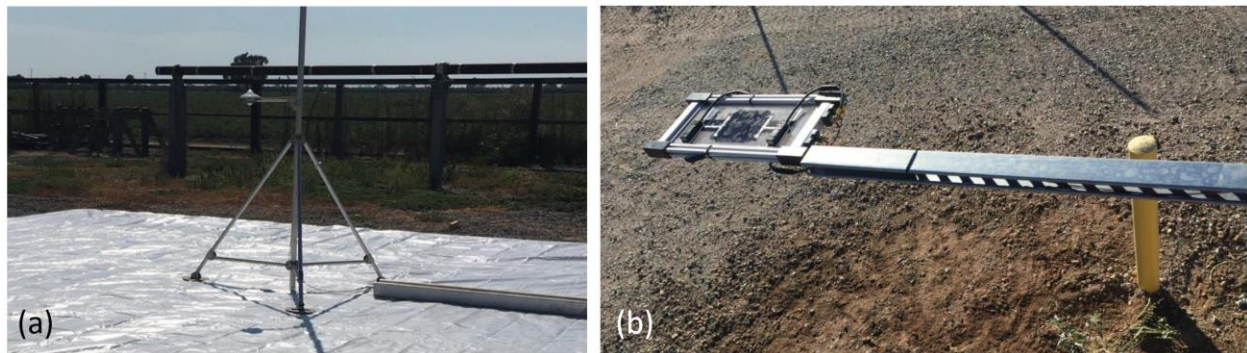
Figure 3.2. Albedometer with two pyranometers, (b) albedometer with two reference cells. (Copyright SunPower Corporation)

Even after measuring the albedo, selecting an accurate value for bifacial PV modeling is challenging. Albedo is not a fixed value and varies spatially and temporally throughout the year with changes in ground moisture, rainfall, snowfall and ground vegetation. Albedo also changes throughout the day with solar angle. Figure 3.3 shows albedo variation of the natural ground (gravel) and highly reflective ground (white tarp) measured by an albedometer (two pyranometers, one facing up and one facing down) at SunPower R&D Ranch in Davis, CA.
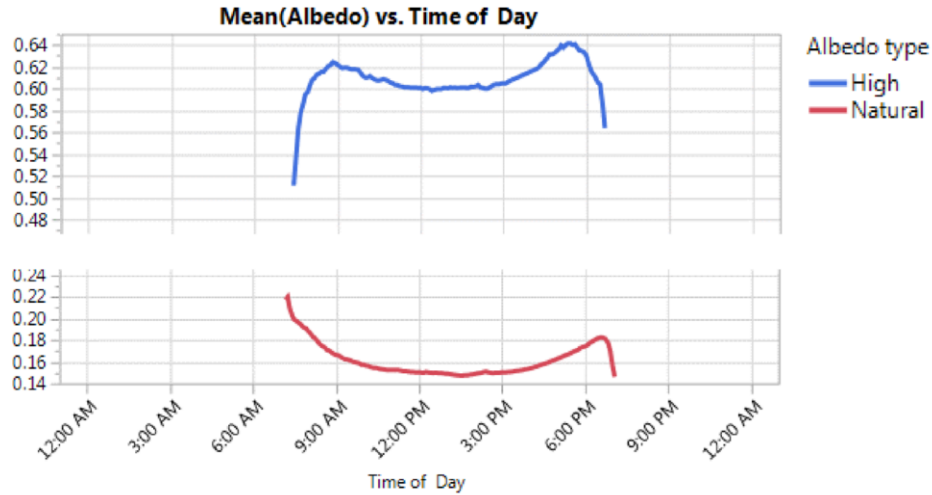
Figure 3.3. Hourly albedo variation of the ground at SunPower R&D Ranch in Davis, CA for natural and high albedo ground.

Furthermore, albedo is dependent on the wavelength and each material has a unique spectral reflectivity. Figure 3.4 shows the spectral albedo (solid line) and effective albedo (dashed line) for a few common materials. A study by Russel et. al. [33] showed that considering the spectral albedo is an important factor in modeling bifacial PV systems. This study suggested that considering spectral albedo of some materials (for example snow, white sand or green grass) results in higher expected power output for bifacial cells compared to the power output while modeling with effective albedo values. On the other hand, some other materials such as red brick and construction concrete exhibits lower output when considering the spectral albedo. This study also derived the ideal spectral albedo for maximum power output and minimum heat impact which can be used for development of artificial ground materials for bifacial PV applications.
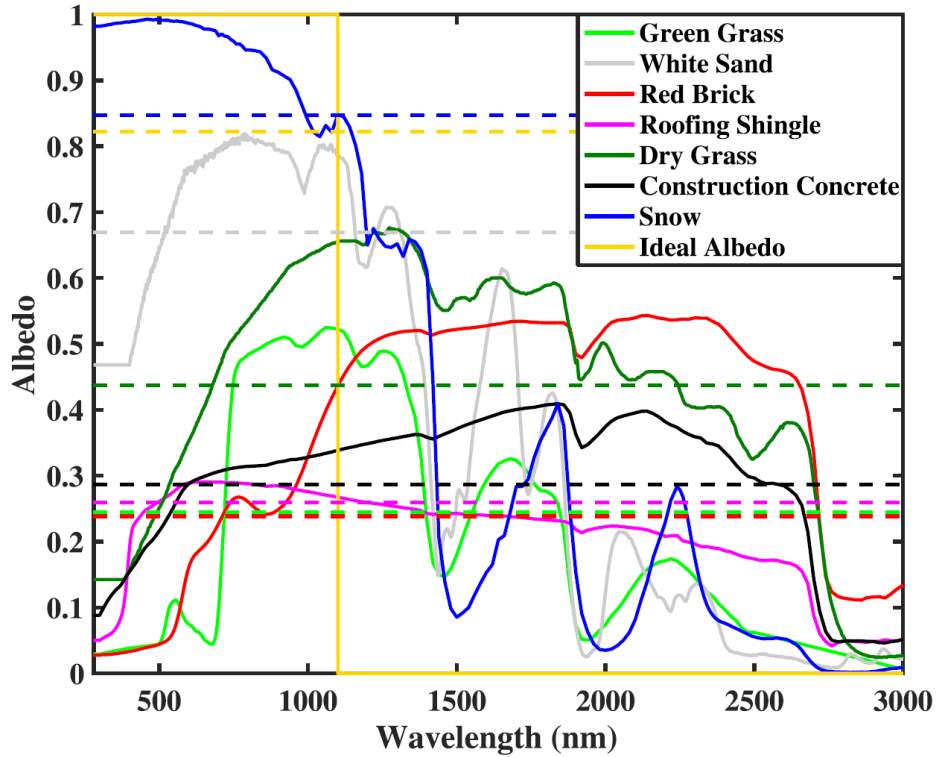
Figure 3.4. The spectral albedo for a few common materials. [33]

In addition to albedo uncertainty, there are other parameters which make the performance modeling of bifacial PV systems challenging. Unlike monofacial PV systems, performance of bifacial systems depends on the height of the modules above the ground. As will be discussed in section 5, increasing the height of the modules from the ground increases the field of view of the unshaded ground and hence increases the irradiance received from the backside of the modules. Therefore, bifacial models should be designed such that they account for this effect.

Furthermore, modeling the impact of nonuniform irradiance due to backside structures such as torque tube, rails, and wiring is difficult and requires utilization of complicated models such as raytracing tools which need high computational power. Nonuniform irradiance due to backside structures can lower the performance of bifacial systems. Bifacial models are expected to capture this effect.

www.manaraa.com

Even with little to no backside structures, different view factors of the PV cells to the ground can cause non-uniformity in the backside irradiance [34]. For example, as shown in Figure 3.5, cell 1 which is located on the lower side of the module sees more of the illuminated ground than cell 2 which is located at higher elevation from the ground. In this case, cell 1 receives higher backside irradiance from the ground compared to cell 2. However, as mentioned, ground reflection is not the only irradiance source of the backside and PV cells receive diffuse sky irradiance as well. Different view factors to the sky cause the cells to receive different fractions of the sky diffuse light. Backside non-uniformity is also visible along the length of the arrays. Modules on the edge receive higher backside irradiance than the modules in the middle due to larger view factor of the unshaded ground on the edges of the PV array. To accurately model the performance of bifacial systems, bifacial modeling tools should utilize a method which captures the impact of the backside non-uniformity.
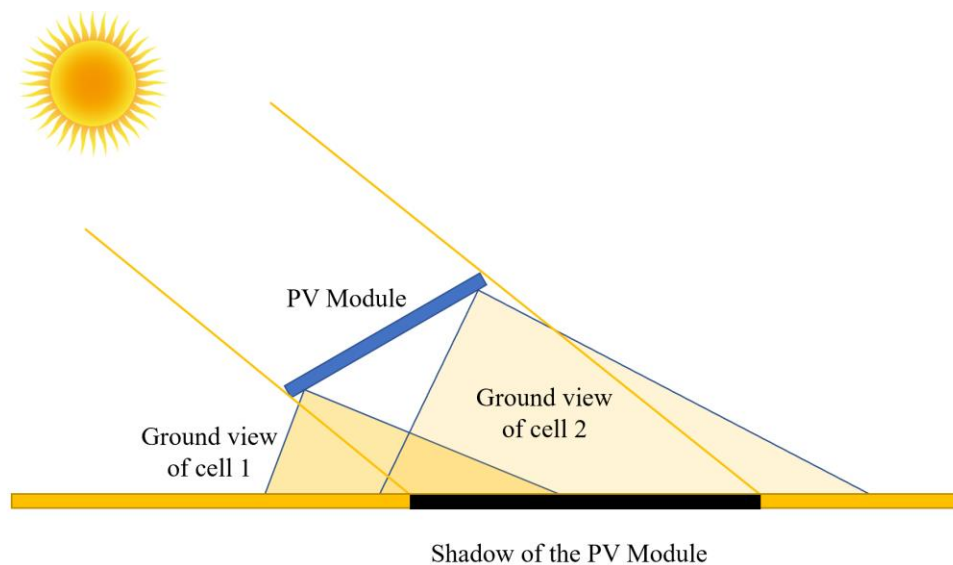
Figure 3.5. Schematic of the variation in ground view factor of the different cells on the modules.

3.2   Modeling Method

Figure 3.6 shows steps for energy modeling of a general PV system. As shown, weather data including irradiance, temperature, and wind speed, system and site specifications such as number of modules, number of rows, module dimensions, racking structure geometry, reflectivity of the objects in the scene (modules, ground, racking structure), pitch or GCR, height of the modules from the ground, tilt angle (for fixed-tilt systems), and tracking algorithm (true-tracking or back-tracking) are required for performing irradiance modeling. Irradiance models run simulations for each timestamp in a given weather file and calculate the irradiance received by the module (for bifacial systems, model outputs two irradiance values; frontside and backside). Calculated available irradiance on modules is used for performing electrical and temperature modeling of the PV systems. These models require specifications of the PV cells and modules such as series resistance, shunt resistant, nominal open-circuit voltage, nominal short-circuit current, configuration of cell interconnection and bypass diodes, cell working temperature, and bifaciality value for bifacial PV modules.
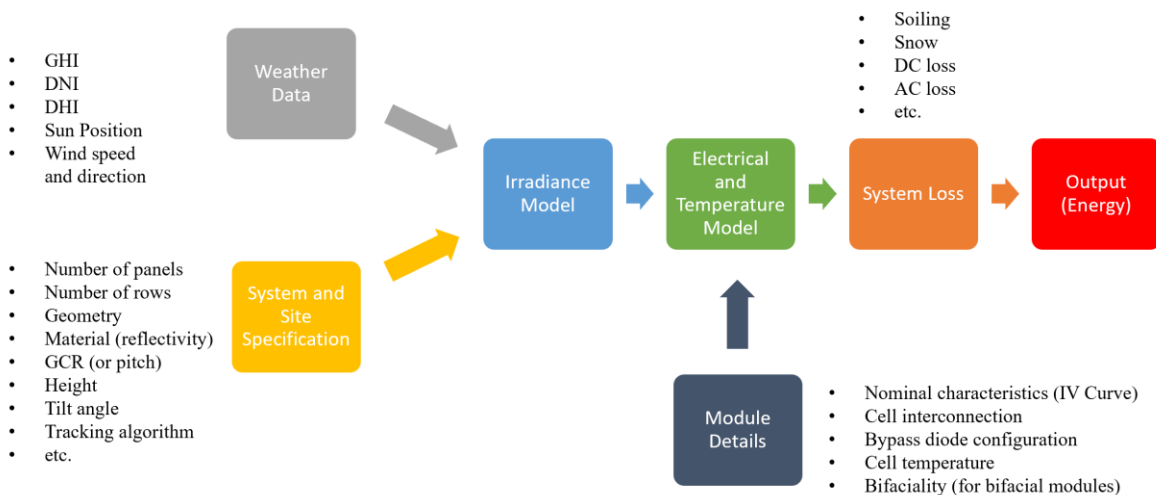
Figure 3.6. Flowchart for energy modeling of a PV system.

Output of the electrical and temperature models is DC current and voltage or power of the system without considering the additional losses which may be present in the system. PV systems experience additional losses such as soiling, snow, DC wiring, AC wiring, inverter, clipping, transformer loss, etc. Discussing the models accounting for theses loss factors is out of scope of this work. But a complete PV system modeling tool should be able to consider the impact of such system losses.

The most critical difference between modeling monofacial and bifacial PV systems is the irradiance modeling step. Monofacial irradiance models are incapable of modeling bifacial systems. For other modeling steps, similar concepts from monofacial PV models can be applied to bifacial PV models. Since focus of this work is on modeling bifacial systems, we discuss the bifacial irradiance models in detail. Later in this chapter, models for calculating the electrical and temperature response of PV system is discussed.

3.2.1 Bifacial Irradiance Models

As discussed in the previous section, developing an accurate and valid tool which can address the challenges faced in modeling of bifacial PV systems is crucial. In recent years, there has been an extensive research on developing irradiance modeling tools to estimate the performance of bifacial PV systems. The developed models can be classified into three categories: raytracing models, view factor models and empirical models.

3.2.1.1 Raytracing Models

Ray tracing is a rendering technique for generating images by tracing the light rays and simulating the way these rays interact with the defined virtual objects in the scene. A set of input control parameters such as number of released rays and number of allowed reflections are usually defined in these models. If a ray reaches the maximum number of allowed reflections or travels a

35

certain distance without any intersection, the ray ceases to travel and the value (irradiance) of the corresponding pixel is updated. There are two types of raytracing methods: forward ray tracing and backward ray tracing (Figure 3.7). In forward ray tracing (light ray tracing or photon tracing) technique, the light rays are followed from their source to the object. Even though this method is highly accurate, it can be very inefficient. The reason lies on the fact that only a small fraction of the traced rays contributes to the final rendered image. On the other hand, as shown in Figure 3.7, the rays can be traced in the reverse order (i.e. from the object to the light source). This method is called backward ray tracing (eye raytracing) and can cut down the simulation time significantly, because only the contributed rays in final image are computed.

For bifacial irradiance modeling, this method promises some benefits. It is capable of accurately modeling the shading patterns on the ground and accounts for direct and diffuse shading on both front and backside of the module. The 3D nature of this method allows capturing the backside non-uniformity, edge effects and the effect of racking on backside irradiance as they are pertinent to modeling of bifacial PV systems.
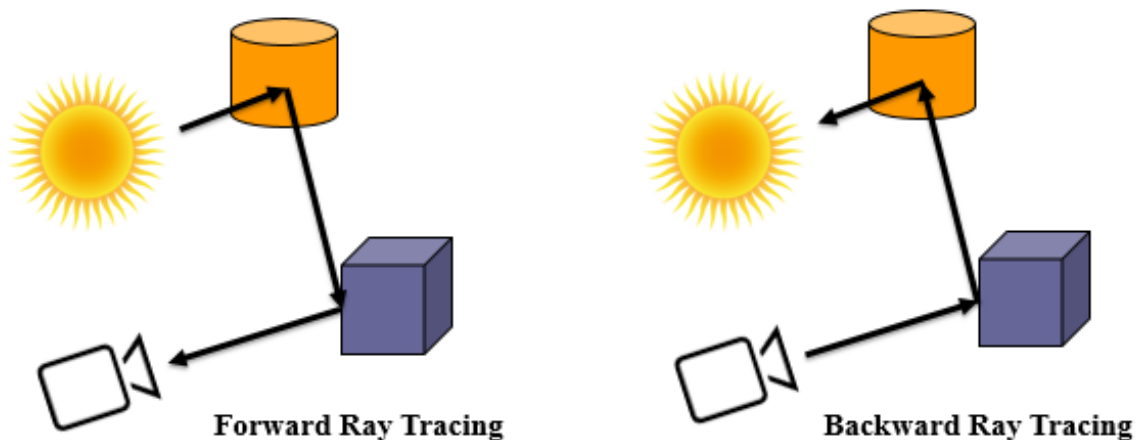
Figure 3.7. Schematics of forward and backward ray tracing.

The downsides of raytracing models are that they are complex and expensive in terms of computation compared to other models which will be discussed in later sections.

Multiple raytracing models have been developed and utilized for irradiance modeling of bifacial PV systems. Following are three well-known raytracing models.

- RADIANCE [35, 36]

- Ray tracing model by EDF Energy and EnerBIM [37]

- SunSolve by PV Lighthouse (forward ray tracing) [38]

Research conducted in this thesis mainly involves utilizing the RADIANCE simulation tool. This open-source software is a validated lighting tool, developed by Greg Ward at Lawrence Berkeley National Laboratory. RADIANCE has been used to simulate the bifacial PV systems previously by other researchers and its accuracy has been tested. [36, 39] Python wrapper functions have been written to facilitate using this model and are available in a package called bifacial_radiance on NREL's GitHub account. [36] In the most recent version, graphical user interface (GUI) has been developed to further facilitate working with this software. The procedure for running a successful RADIANCE simulation is shown in Figure 3.8 and is described as following:

- The geometries of the objects in the scene can be created by using binaries available in the RADIANCE package if the geometry is simple. For complex scenes it is recommended to develop the scene in a 3D modeling tool such as SketchUp, AutoCAD, or SolidWorks and covert it to the format readable by RADIANCE (RAD).

- The material of all the objects in the scene need to be defined. There are multiple available formats to define a wide range of materials. Reflectivity of the surface in 3 color channels; red, green and blue (RGB), roughness, specularity and other characteristics of a surface can be

37

defined. The identifier in these definitions should match to the modifier of the correspondent geometry defined in the previous section. Same as geometry files, the materials files need to be in RAD format.

- Sky files are the essential part of the irradiance simulations. In RADIANCE, sky files (RAD format) can be created by "*gendaylit*" command. *Gendaylit* creates a RADIANCE scene description based on an angular distribution of the daylight sources (direct and diffuse light) for the given atmospheric conditions (direct and diffuse component of the solar radiation), date and local time. The output is the luminance distribution of the sky integrated over the visible spectral range (380-780 nm). The diffuse angular distribution is calculated using the Perez All-Weather Sky Model [40].

The Perez All-Weather Sky Model is a mathematical model used to describe the relative luminance distribution of the sky dome. This model uses real data gathered from various weather stations all over the world and has become the de facto standard model for daylighting calculations. The two parameters in the Perez Model are *delta* (representing sky brightness) and *epsilon* (representing sky clearness). These parameters are determined from the measured diffuse horizontal and direct normal irradiance values for specific sites and date/time combinations. Epsilon variations express the transition from a totally overcast sky (epsilon=1) to a low turbidity clear sky (epsilon > 6). Delta variations reflect the thickness of the clouds and can vary from 0.05 (dark sky) to 0.5 (very bright sky).

- The next step is to combine all the RAD files generated in the previous steps and create a single octree file for each timestamp of the simulations. This step is done using "oconv" command in RADIANCE.

38

- The final step is to render the octree file. By defining coordinates of the points on the front and back sides of the module (usually center of the cells is chosen) and using "rtrace" command, rays can be traced from these points and the irradiance can be calculated on them. It is worthwhile to mention that this process is stochastic in nature and simulations with the same input parameters may have small differences in results.
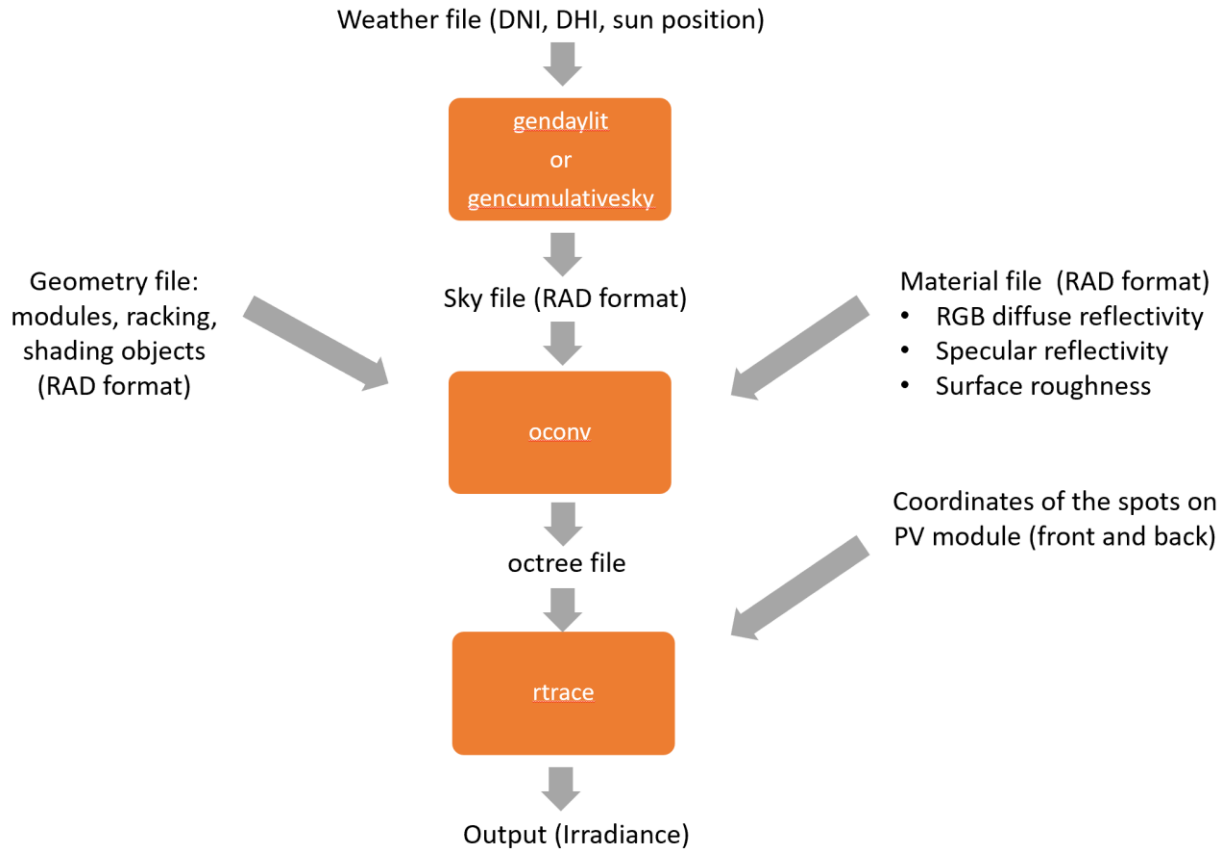
Figure 3.8. Flowchart for running bifacial irradiance simulations using RADIANCE.

As mentioned before, the downside of this detailed and complex model is that it is computationally expensive, and it takes more time to run simulations compared to other models which will be discussed next. So, running hourly-based simulations to calculate the annual energy yield will require significant amount of time and resources. To overcome this disadvantage, cumulative sky approach [41] within RADIANCE can be utilized to downsize the computation

time significantly with only a minor drop in accuracy. The command is called "gencumulativesky". It involves discretizing the sky dome into 145 patches and using the Perez model to calculate the radiance at the centroid of each patch for a given hour. Patches closer to the Sun have higher radiance values. For modeling the Sun, a binned set of suns can be defined discretely, or the radiance of the patches where Sun is located can be increased. The latter is more computationally efficient. After creating the sky radiance distribution for each hour (shown as an example for a day in Figure 3.9), these distributions are aggregated for the period of interest (one year for our case) to create a "cumulative" sky. An example of the cumulative sky diffuse radiance distribution is shown in Figure 3.10 which is based on 10 years of solar data for Oslo, Norway. The center of the circle in this figure represents the top of the sky dome (zenith angle of 0°) and the outer ring is the section of the sky near horizon.
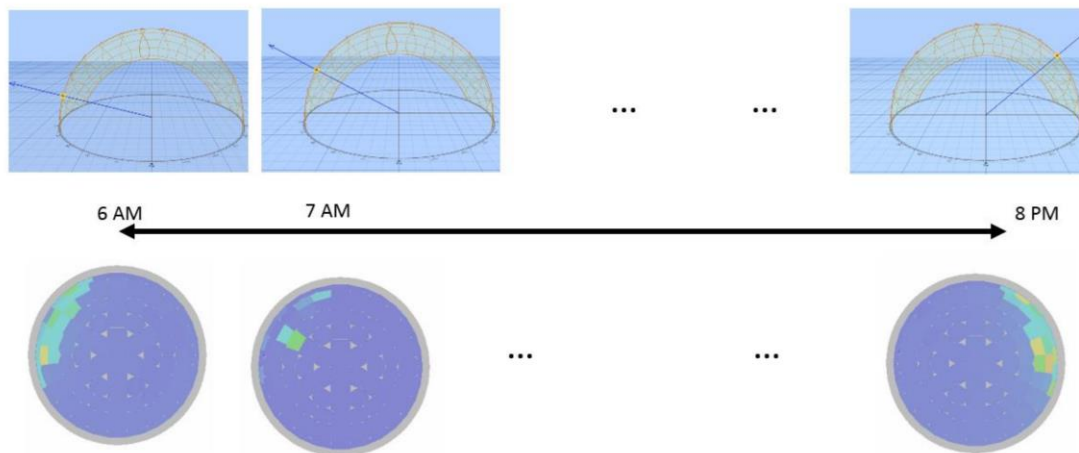
Figure 3.9. Radiance distribution over the sky dome calculated using Perez model for each hour. These distributions can be added to create a cumulative sky radiance distribution. [42]

40
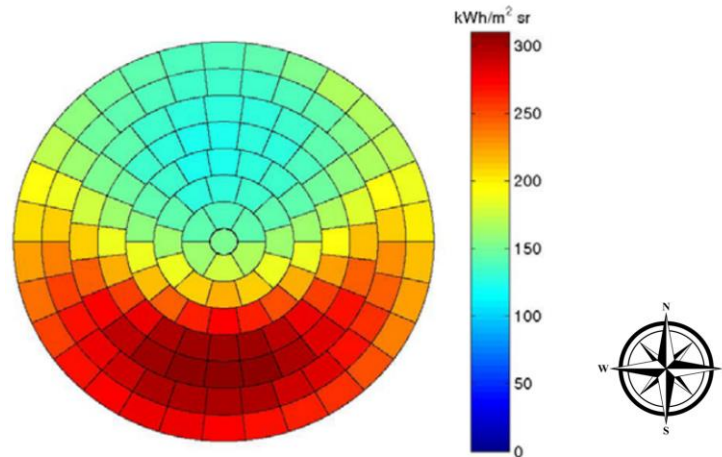
Figure 3.10. Cumulative diffuse sky radiance distribution for Oslo (based on 10 years mean solar data) [41]. The center of the circle represents the top of the sky dome (zenith angle of 0º) and the outer ring is the section of the sky near horizon.

3.2.1.2 View Factor Models

View factor (configuration factor) models are based on radiative transfer calculations of the amount of radiation leaving a surface (A) that strikes on the receiving surface (B) and is shown as $VF_{A \to B}$ in the following equation:

$$VF_{A \to B} = \int_{A_1} \int_{A_2} \frac{\cos \theta_1 \cos \theta_2}{\pi s^2} \, dA_2 \, dA_1 \qquad (3.1)$$

where θ_1 and θ_2 are the angles between the normal vectors to surfaces dA_1 and dA_2 respectively as shown in Figure 3.11.

41
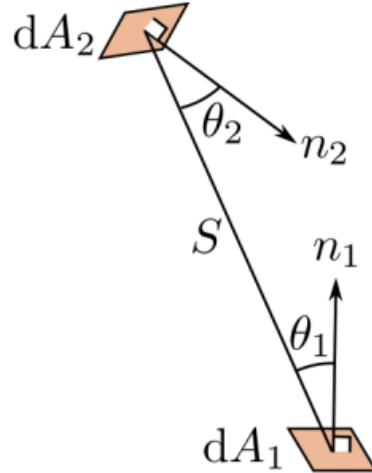
Figure 3.11. Calculation of view factors for two surface elements.

The view factors are based on the two simple assumptions; isotropic scattering of radiation from any surface and the conservation of radiation. After calculating the view factors for the surfaces of interest, the irradiance on each surface (I_B) can be calculated by the following equation:

$$I_B = \sum F_{A \to B}\, I_A \qquad (3.2)$$

where I_A is the irradiance reflected from surface A and equals the incident irradiance on it multiplied by the reflectivity of the surface. To calculate the radiation on all surfaces, a system of linear equations is solved mathematically.

Multiple view factor models have been developed to estimate the performance of bifacial PV system. Following is the list of the major view factor models:

1. bifacialvf [43]

2. Sandia_bifacial_viewfactor (3D view factor model) [44]

3. PVsyst [45]

4. pvfactors [46]

5. Purdue University Bifacial Module Calculator (PUB) [47]

42

The view factor method is easy to implement. It is also very efficient in terms of the computation and annual simulations can be run in a few seconds. However, most of the view factor models are 2D models and this assumption casts some doubt on their applicability for certain system types. The 2D view factor models assume infinitely long PV rows due to the inability to model the third dimension. This means that they assume a consistent irradiance along the PV rows. While, this is a fair assumption for large PV plants, it results in high errors for smaller system. As discussed for bifacial PV systems, the modules on the edges usually receive more irradiance due to larger unshaded view factors (edge effect). However, 2D models assume to have the same ground shading impact for all the modules along the row and cannot capture this effect. Another downside of this model is the difficulty in modeling the structure and the irregular geometries which is impactful on the backside irradiance. Aggregation of these errors result in having lower accuracy for the view factor models than raytracing methods.

3.2.1.3 Empirical Models

Simple models based on combination of measured and simulated data are developed to calculate the bifacial gain approximately using limited number of variables. These models are not climate sensitive and have a relatively low accuracy. Two most well-known models are the following:

- Prism Solar [48]

    In this model, an equation for bifacial gain in energy (BGE) is fitted to a set of measured data from bifacial PV systems (with different installation parameters) and is shown as following:

$$BGE\ (\%) = a.\beta + b.H + c.albedo(\%) \qquad (3.3)$$

43

where β, and H are tilt angle and clearance of the module from the ground, respectively. Curve fitting coefficient values (a, b, and c) are shown in Table 3.2. This model is valid for fixed-tilt south-facing modules only and is suggested for locations with latitudes of 21° to 51 °.

Table 3.2. Curve fitting coefficients for Prism Solar's empirical bifacial model.

Coefficient	Value
a	0.317/degree
b	12.145/m
c	0.1414/%

- SolarWorld [49]

This empirical model is based on system-level raytracing simulations [50] and has input parameters such as albedo, bifaciality factor, ground coverage ratio (GCR), and normalized module height (H = $\frac{h}{W}$) where h is the module clearance from the ground and W is the module width). The equation for calculating BGE is as following:

$$BGE\ (\%) =\ albedo\ (\%)\ .\ bifaciality\ factor\ .\ s\ [\ a\left(1 - \sqrt{GCR}\right)(1 - e^{-b.H.GCR}) +$$

$$c\ (1 - GCR^4)] \qquad (3.4)$$

The constant values a, b, c, and s are described in Table 3.3.

Table 3.3. Coefficients for SolarWorld's empirical bifacial model.

Coefficient	Value
a	1.03
b	8.69
c	0.12
s	0.95

3.2.2 Electrical and Temperature Models

Output of the irradiance models (irradiance values) is used as input for electrical models to calculate the electrical response of the PV system and compute the possible mismatch between the modules. Most of the electrical models are based on either of two circuit models for PV cells; single-diode model or two-diode model. The electrical model combines the electrical response of each cell (I-V curve) with the response for other cells and bypass diodes within the module to calculate the I-V curve of the module. Next, the response of all the modules in each string are combined and the overall I-V curve of the system is calculated.

3.2.2.1 Single-diode Model

The single-diode model of a solar cell is shown in Figure 3.12. The diode is meant to represent the P-N junction used in the solar cell. The I_{ph} is the photon generated current produced by the photovoltaic effect. This current depends on the amount of the light absorbed by the cell. R_s is the series resistance and depends on the contact resistance and surface defects of the cell. R_p is the shunt resistance which controls any leakage current in the cell. Ideal solar cell exhibits zero R_s and infinite R_p.
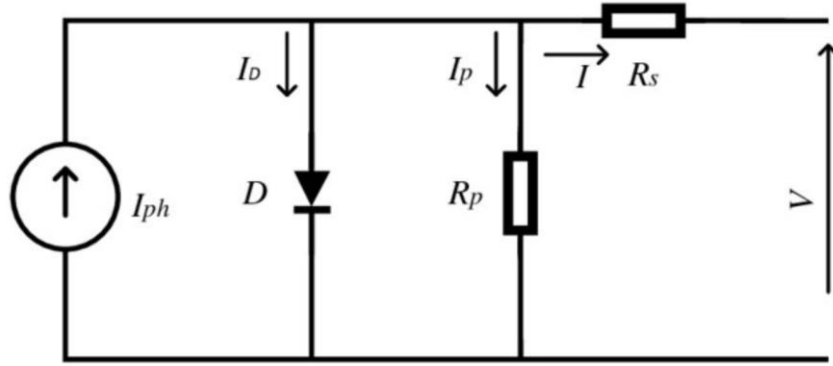
Figure 3.12. Single-diode model of a solar cell. [51]

The I-V characteristic of this model can be described as below:

$$I = I_{ph} - I_0 \left[\exp\left(\frac{V+IR_s}{nV_T}\right) - 1\right] - \frac{V+IR_s}{R_p} \qquad (3.5)$$

$$V_T = \frac{kT_c}{q} \qquad (3.6)$$

Where:

I_0:   Diode reverse saturation current (A)

V_T: Thermal voltage (V)

K: Boltzmann's constant ($1.38064852 \times 10^{-23}$ J/K)

T_c: Temperature (K)

q: Elementary charge ($1.602176634 \times 10^{-19}$ C)

n: Ideality factor of the diode

3.2.2.2 Double-diode Model

Two-diode model [52] offers higher accuracy especially for crystalline silicon solar cell.

Figure 3.13 shows the schematic of this model.
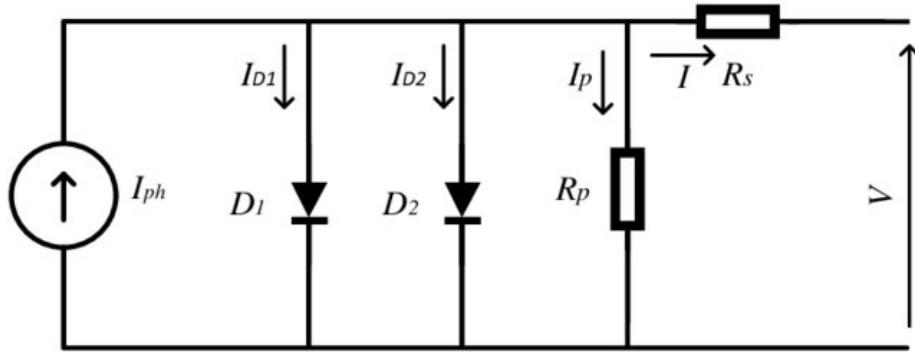
Figure 3.13. Double-diode model for a solar cell. [51]

I-V characteristic of the double-diode model for solar cell is as following:

$$I = I_{ph} - I_{01}\left[\exp\left(\frac{V+IR_s}{n_1 V_T}\right)-1\right] - I_{02}\left[\exp\left(\frac{V+IR_s}{n_2 V_T}\right)-1\right] - \frac{V+IR_s}{R_p} \qquad (3.7)$$

As implied by its name this model has two diodes. First diode represents diffusion and surface recombination. On the other hand, second diode models the recombination in the depletion region. It is a common practice to set the ideality factor of the first diode to one and the second diode to two.

Mentioned electrical models uses the circuit model for each cell and can calculate the overall response of a PV module with non-uniform irradiance on the cells, Therefore, these models can be used to capture backside non-uniformity in the bifacial PV modules. Mentioned electrical models can be used for bifacial PV systems with slight modification and bifaciality factor should be considered in calculating effective irradiance on the cells. One of the suitable electrical models for this purpose is PVMismatch [53]. PVMismatch is based on the two-diode electrical model of a solar cell and is capable of electrical modeling of a PV system based on the irradiance distribution, cell parameters, circuit design and the cell working temperature.

Figure 3.14 shows an example for the evaluation of the effect of backside struts on the performance of a bifacial module using RADIANCE and PVMismatch. Irradiance modeling was

47

performed by RADIANCE. CAD models of the module and the support structure were imported into the RADIANCE and irradiance simulations were run using typical meteorological weather data (TMY) for Cedar Rapids, Iowa. A high albedo of 0.6 was assumed for this study.

The PVMismatch uses the irradiance map from the RADIANCE simulations and calculates the IV curve for the module. For the specific case shown in Figure 3.14, a double strut on the backside of the module decreases the maximum power (P_{mp}) of the bifacial module by 12.6 W.
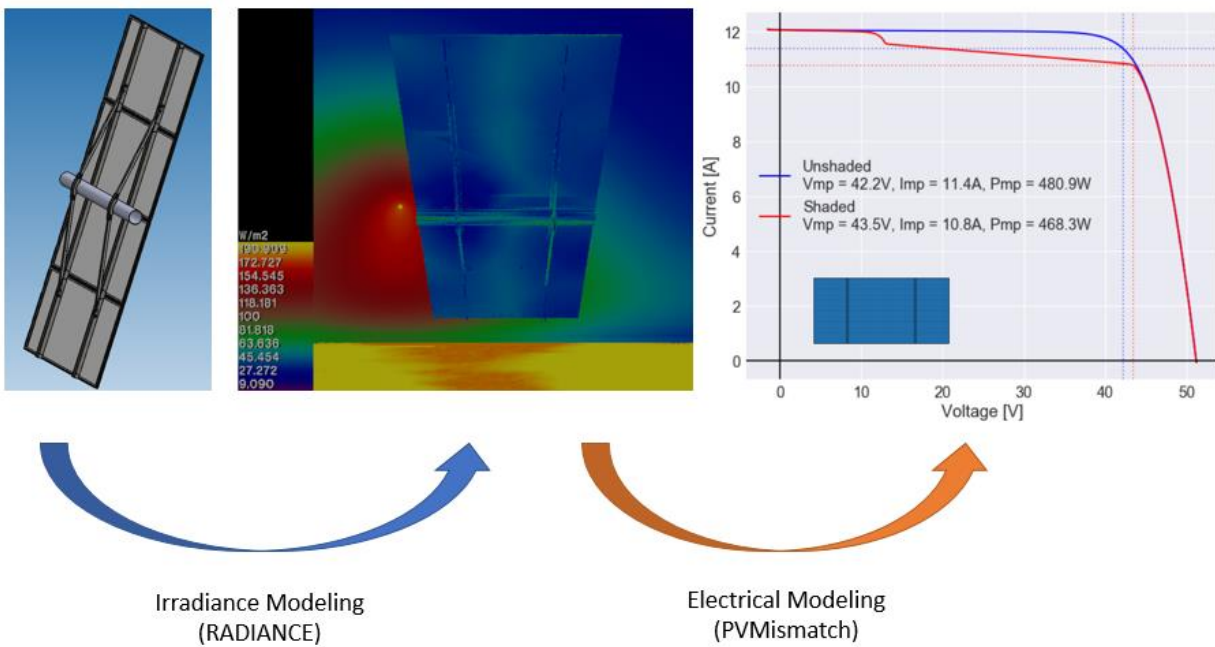
Figure 3.14. Combined irradiance and electrical modeling by RADIANCE and PVMismatch to evaluate impact of strut shading on the backside of a bifacial module in Cedar Rapids, Iowa.

4   BENCHMARKING AND VALIDATION OF BIFACIAL PV IRRADIANCE MODELS

While there are a few available bifacial irradiance models, not enough validation studies have been conducted. Validation is crucial to assess the accuracy and applicability of the models to real world system deployments. In this section, a few of the major bifacial irradiance modeling tools are used to model real bifacial PV systems. Irradiance measured by the installed sensors (pyranometer or reference cells) at sites was compared with the simulated irradiance values to validate these models. Furthermore, a benchmark between view factor and raytracing models was performed, and model results were compared.

4.1   Fixed-tilt Systems Case Studies

As the first case study, fixed-tilt string-level, bifacial PV arrays at Sandia National Laboratories (Sandia), Albuquerque, NM were simulated using RADIANCE (bifacial_radiance). Figure 4.1 (a) shows the system. It consists of four rows with different tilt angles (15°, 25°, 35°, and 45°). Each row has two strings of eight modules (one monofacial and one bifacial). Each row also has three reference cells near the middle of the row: one for front and two for the back side. Backside reference cells are installed on top and bottom of the middle module in the row as shown in Figure 4.1 (b).
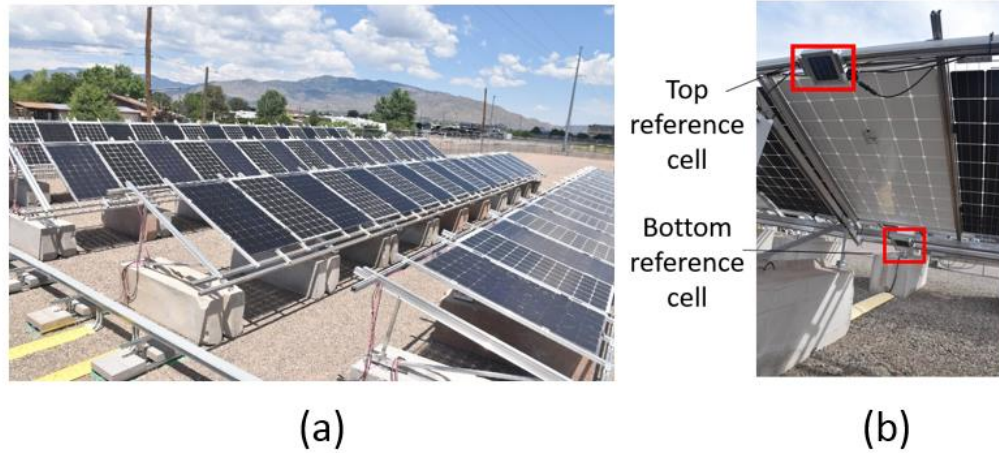
Figure 4.1. (a). Sandia's fixed-tilt string-level arrays. (b) Each row has two backside reference cells (top and bottom).

Using the raytracing model, we were able to simulate not only the modules but also the concrete blocks used for the array footings and the racking system to account for all the possible reflection or shading (diffuse or direct) caused by these objects. Figure 4.2 shows the rendered image using the model. In the rendered scene, irradiance was calculated on the same sensor location where the measurement readings performed.
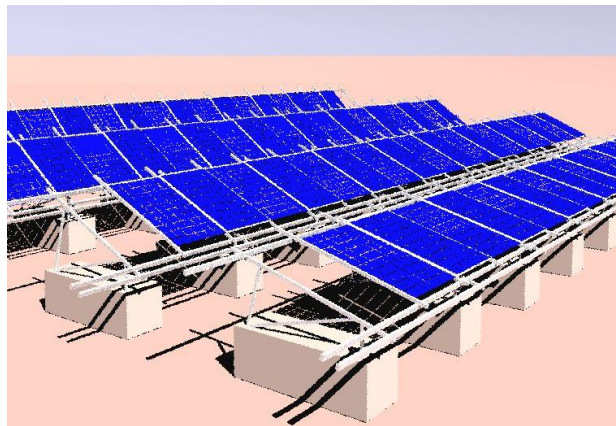
Figure 4.2. Rendered image using RADIANCE raytracing tool.

Simulated irradiance was compared to field measurements for a clear day on March 1st, 2017 (measured albedo of the site for this day was 0.21). Figure 4.3 and Figure 4.4 show the comparison between measured and simulated data for frontside and backside irradiance,

50

respectively. The comparison shows a good match between the measured and simulated data. For each case, RMSD (root mean square deviation) and NRMSD (normalized RMSD) was calculated to compare the simulated data to the measured data. Lower RMSD value means a better match to the measured data.

$$RMSD = \sqrt{\frac{\sum_{t=1}^{n}(x_{1,t} - x_{2,t})^2}{n}} \quad (4.1)$$

$$NRMSD = \frac{RMSD}{x_{1,max} - x_{1,min}} \quad (4.2)$$

x_1:   Measured data

x_2:   Modeled data

n: Number of data points

For frontside the NRMSD range is between 4.5% and 6.8%. For backside irradiance this range is larger and is between 4.3% and 16.4%. Considering the backside irradiance data (Figure 4.4), we observe that top and bottom reference cells receive different irradiances. This non-uniformity in the backside irradiance causes power mismatch and decreases the performance of the system. By increasing the tilt angle, non-uniformity decreases, because modules receive more uniform irradiance from the sky than the ground.

The mismatch between the measured and simulated data may be due to the optical properties of the materials set in the simulations. In the next section, a more recent validation will be presented on this model. In that simulation, very detailed optical properties of the objects were used, and the mismatch is shown to be lower.

Furthermore, the discrepancy between the modeled and measured data may be due to the fact that we didn't apply an angle of incidence (AOI) correction in the RADIANCE simulations. AOI loss is the optical loss resulting from non-normal incidence of the light on the module surface (and hence higher reflection loss). On the other hand, the reference cells used to measure the

irradiance include AOI loss, since they are built similarly to PV modules. Therefore, we speculate that some degree of overestimation for both modeled frontside and backside irradiance may be due to the inability of the model to account for AOI loss. However, this hypothesis requires future investigations.
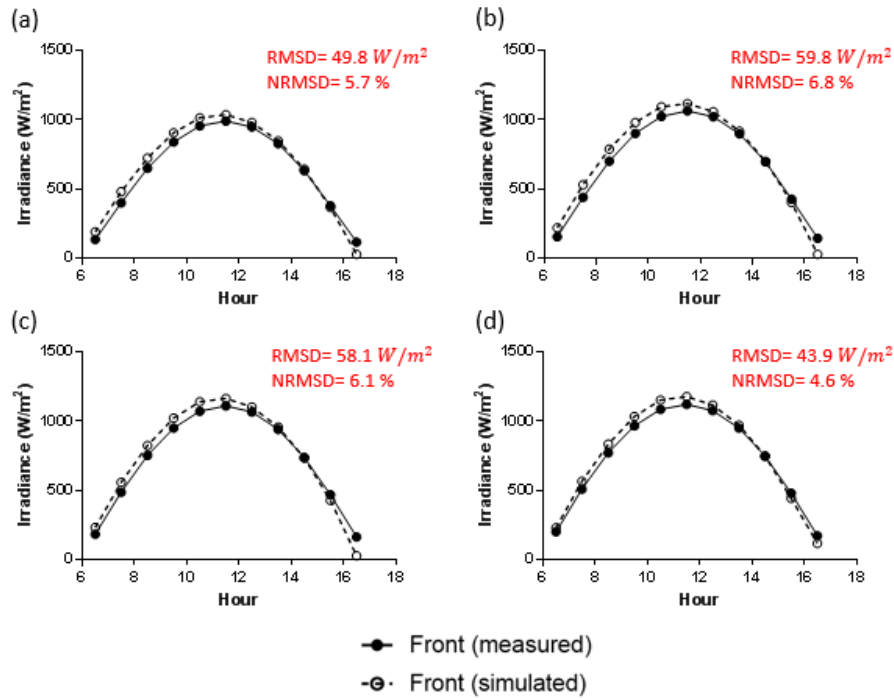
Figure 4.3. Simulated versus measured frontside irradiance for (a) first row (15°), (b) second row (25°), (c) third row (35°), and (d) fourth row (45°) of Sandia's fixed-tilt string-level arrays.
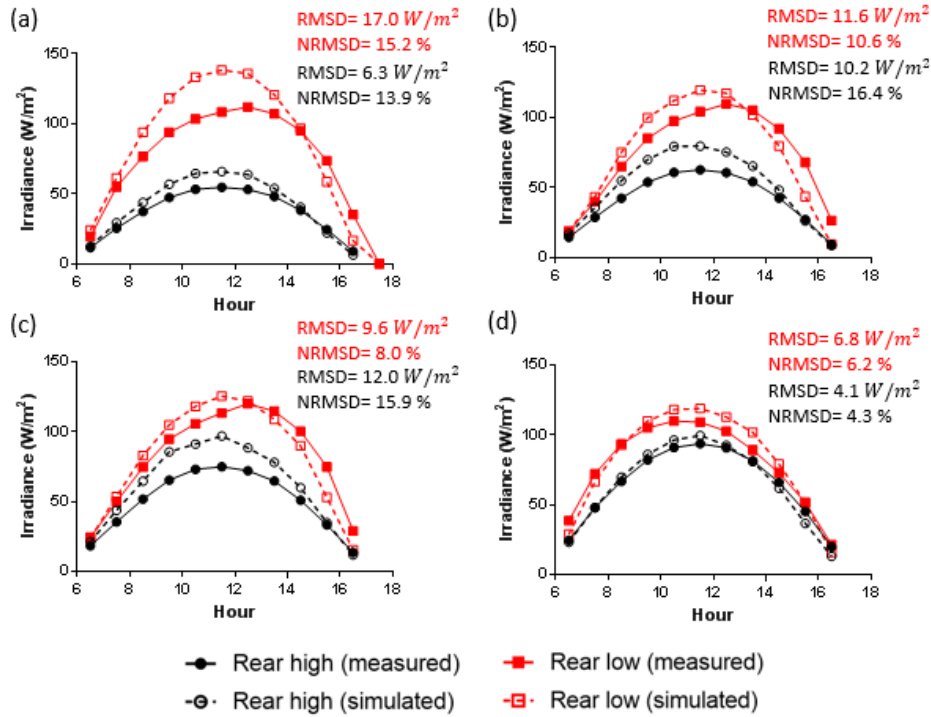
Figure 4.4. Simulated versus measured backside irradiance for (a) first row (15°), (b) second row (25°), (c) third row (35°), and (d) fourth row (45°) of Sandia's fixed-tilt string-level arrays.

During my internship at SunPower Corporation, I performed benchmark and validation for four major bifacial irradiance models in the PV industry. One of the purposes of this task was to validate and increase the accuracy of the company's in-house bifacial model (pvfactors) by comparing the results and the methodology of this model with other bifacial models and implementing the necessary methods in the model. Four bifacial models including bifacial_radiance (v0.2.1), bifacialvf (v0.1.6), pvfactors (v0.1.5) and PVSyst (v6.7.4) were used to simulate two test sites using measured weather data. The first system is installed at Sandia National Laboratories in Albuquerque, NM and is composed of four strings, each with four modules (the system is eight-modules long in two Up landscape configuration). The system is installed at a fixed tilt angle of 35° and an azimuth orientation of 180° (facing south). Figures 4.5 (a) and (b) show the system, layout and the locations of two European Solar Test Installation (ESTI) irradiance sensors (reference cells) fabricated and calibrated by PV Evolution Labs. One reference cell is

53

mounted in the plane of array (POA) adjacent to the system on the west side. The other ESTI reference cell is mounted facing the same direction as the rear side of the modules and is located in the middle of the array.

(a)
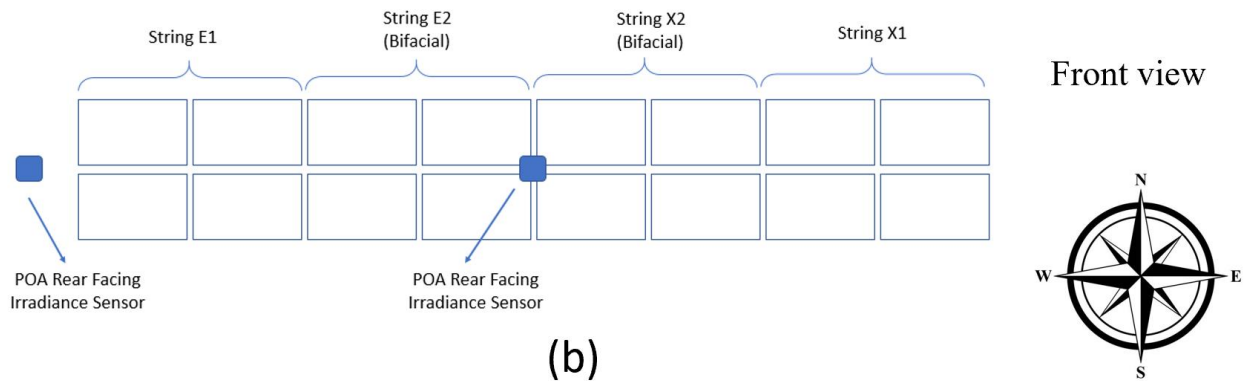
(b)

Figure 4.5. (a) Image from the system installed in Albuquerque, NM. (b) Layout of the test array and the installed sensors.

Measured weather data including GHI, DNI, DHI, albedo, and Sun position was used to model the system using the four irradiance models. To achieve the highest accuracy from the raytracing model, in addition to the general input data such as the system configuration, tilt angle, azimuth orientation, height, and reflectivity of the ground (albedo), the CAD model of the modules, racking, and concrete footings was imported to the RADIANCE to account for all possible direct and diffuse shadings. The material definition for the modeled modules was based

54

on the measured reflectance data of SunPower E20 solar panel, provided by MIT Sustainable Design Lab [54] which includes measured diffuse and specular reflectance values for the visible spectrum. Table 4.1 shows the reflectance values used to define the material of PV modules in the RADIANCE scene.

Table 4.1. Reflectance values used to define the material of PV modules in the RADIANCE scene for the four-string fixed-tilt system installed in Albuquerque, NM.

Parameter	Reflectance
R-reflectance	3.6 %
G-reflectance	3.83 %
B-reflectance	5.32 %
Specular reflectance	2.99 %
Total reflectance	3.87 %

The rendered images using RADIANCE are shown in Figure 4.6. In addition to regular simulations, the same system without the racking system is also modeled to analyze the impact of racking system on the yield of the system. The simulation results as well as measured irradiance data for both front and back sides of the system are shown in Figure 4.7 and Figure 4.8, respectively for a single clear day (June 22, 2017). Measured albedo from the albedometer on the site for this day was 0.21.
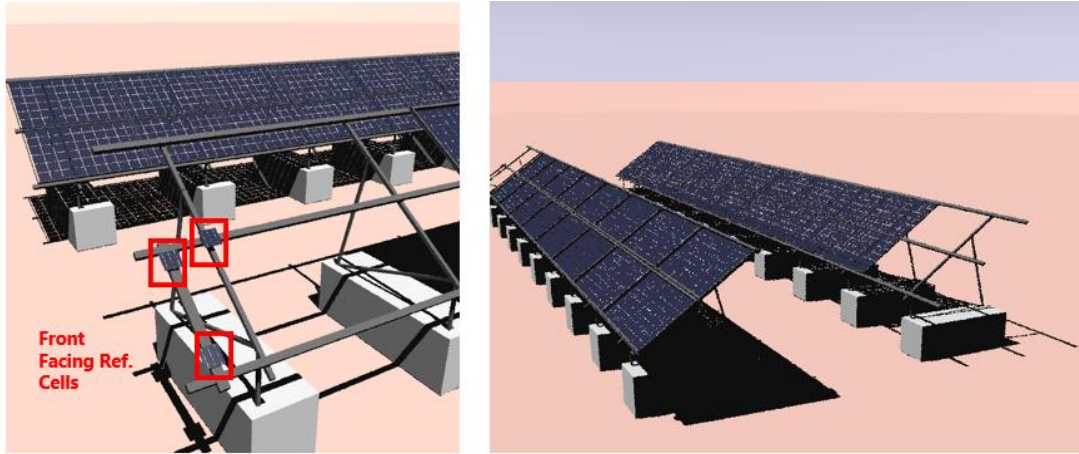
Figure 4.6. Rendered images from the RADIANCE for the four-string system installed at Sandia National Laboratories, Albuquerque, NM.
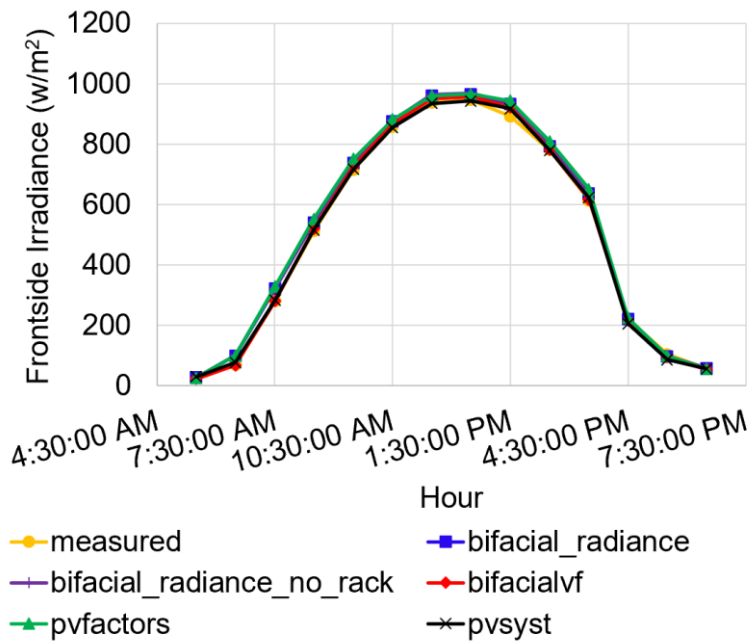
Figure 4.7. Comparison of the modeled irradiance data with the measured irradiance for frontside of the fixed-tilt array installed at Sandia National Laboratories in Albuquerque, NM on June 22, 2017.
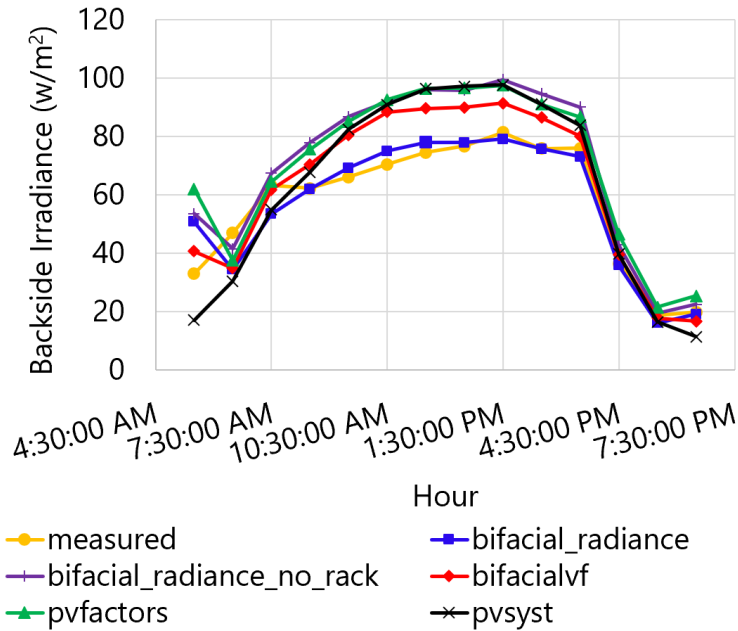
Figure 4.8. Comparison of the modeled irradiance data with the measured irradiance for backside of the fixed-tilt array installed at Sandia National Laboratories in Albuquerque, NM on June 22, 2017.

RMSD and normalized RMSD values were calculated for each simulation to evaluate the deviation of the modeled results from the measured data (Table 4.2).

Table 4.2. RMSD and NRMSD values for the modeled frontside and backside irradiance of the fixed-tilt system installed at Sandia National Laboratories, Albuquerque, NM on June 22, 2017.

Model	Frontside RMSD (W/m^2)	Frontside NRMSD (%)	Backside RMSD (W/m^2)	Backside NRMSD (%)
bifacial_radiance	23.4	2.5	6.7	10.7
bifacial_radiance_no_rack	25.2	2.7	15.5	24.8
bifacialvf	10.6	1.2	10.2	16.3
pvfactors	30.1	3.3	16.0	25.5
PVSyst	10.1	1.1	14.3	22.8

57

As seen in Figure 4.7 and Table 4.2, the frontside irradiance from the modeled data matches well to the measured data (NRMSD value for all the models is less than 3.3 %). We observe that among the models, bifacialvf and PVSyst have higher accuracy in modeling frontside irradiance compared to bifacial_radiance and pvfactors. The most probable reason is that these two view factor models apply AOI correction to the calculated irradiance and as a result have a better match to the measured irradiance from the reference cells. However, future investigations and studies are needed to test this hypothesis.

NRMSD for the backside irradiance (Figure 4.8 and Table 4.2) is higher compared to the frontside (the range for backside NRMSD is 10.7 % to 25.5 %). While the raytracing method (bifacial_radiance) seems to have a better match to the measured backside irradiance, due to the significantly higher amount of time needed to run such detailed simulations, it is not practical unless powerful computers and clusters are utilized for running such simulations. The view factor models are simpler and take considerably less time to run but have slightly lower accuracy compared to raytracing models. Even though the NRMSD values are higher for the backside irradiance, comparing the RMSD values we observe that backside RMSD values are lower than the frontside RMSD (except for PVSyst). This observation shows that the uncertainty contribution from rear irradiance to total irradiance is actually lower than the frontside irradiance uncertainty.

Comparing the results from the two bifacial_radiance simulations (with and without racking) shows the impact of such racking systems. Modeling the system without racking system results in an about ~25% overestimation in the backside irradiance (compared to ~11% overestimation when the racking is present). As mentioned in the previous sections, the current view factor models don't account for the racking and this is one of the major reasons for their overestimation of the backside irradiance. As shown in Figure 4.8, bifacial_radiance_no_rack

58

simulation results match very well to the view factor modeling results and confirms that major overestimation of view factor models comes from their inability to model racking systems and backside shading structures. This is an important result because one might argue that by neglecting edge effects, the 2D view factor models might underestimate backside irradiance for this small system. But in fact, these models overestimate backside irradiance because they do not include the effects of the racking.

4.2   Single-axis Tracking System Case Study

Bifacial irradiance models used to simulate the fixed-tilt system at Sandia (bifacial_radiance, bifacialvf, pvfactors and PVSyst) are used also to model a single-axis tracking system installed at SunPower R&D Ranch in Davis, CA (Figure 4.9). This system consists of three rows of PV modules which are installed in either 2-portrait or 4-landscape configurations. Ground material covering the area under it is gravel with a measured albedo of ~0.15. There are multiple irradiance sensors (pyranometer and reference cell) installed on the front and backside of this system. However, only two reference cells (EETS RC01) are used for this study. These sensors are installed on the front and back side of the most centered module in the middle row. The rear facing reference cell is installed between the ground and torque tube and therefore is not impacted by the shading of the torque tube. (Figure 4.10).

Figure 4.9. Single-axis tracking system installed at SunPower R&D Ranch in Davis, CA.
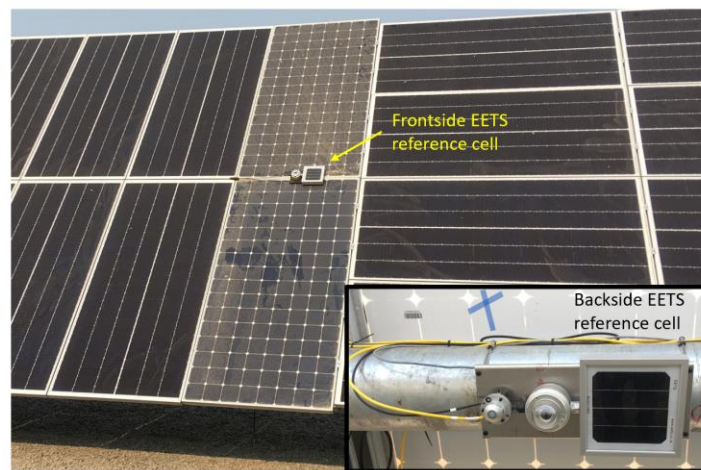
Figure 4.10. Installed location of two EETS reference cell on the front and backsides of the single-axis tracker systems installed at SunPower R&D Ranch, Davis, CA.

Measured weather data (GHI, DNI, DHI, and albedo) was used to run simulations for a clear day on October 8, 2018. On this day, the trackers were on the back-tracking mode. Figure 4.11 and 4.12 show the comparison of modeled frontside and backside irradiance data to the measured data from the reference cell sensors on the site.

60
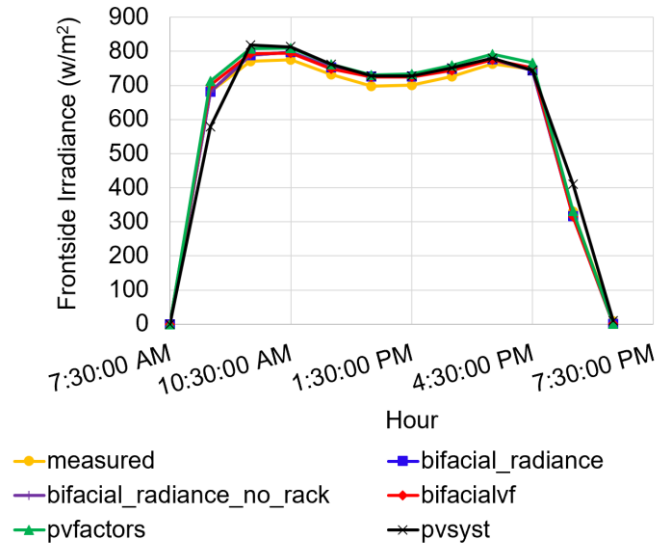
Figure 4.11. Comparison of the modeled irradiance data with the measured irradiance for frontside of the single-axis system installed at SunPower R&D Ranch in Davis, CA on October 8, 2018.
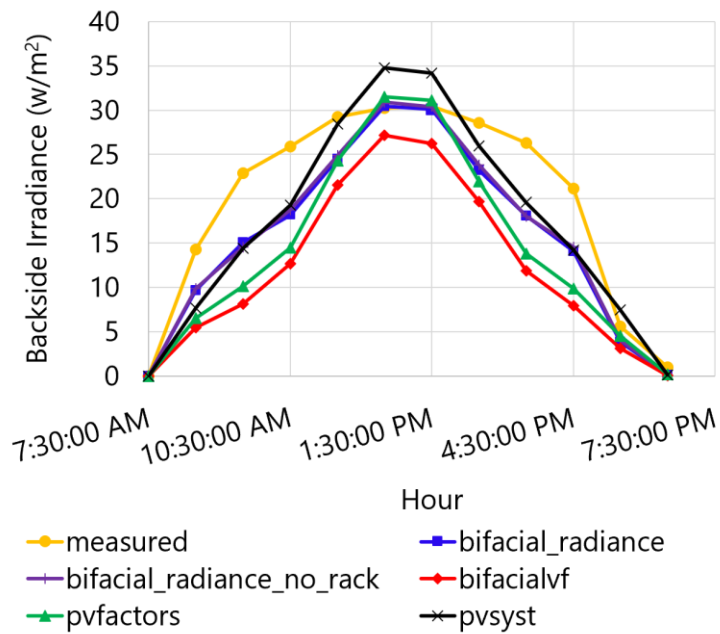
Figure 4.12. Comparison of the modeled irradiance data with the measured irradiance for backside of the single-axis system installed at SunPower R&D Ranch in Davis, CA on October 8, 2018.

61

First observation from the comparison between modeled and measured irradiance data is that the racking system's shadow on the ground has negligible impact on the backside irradiance. As shown in Figure 4.12, bifacial_radiance and bifacial_radiance_no_rack simulations resulted in similar backside irradiance. The reason is that in single-axis tracking systems, the shadow from the backside structure is almost hidden in the shadow casted by the modules themselves and therefore doesn't significantly reduce reflected light from the ground. However, this doesn't mean that backside structure can be avoided in simulating single-axis tracking systems. In this study we have simulated the irradiance on a reference cell which is not directly impacted by the racking structure. It is obvious that backside structures such as the torque tube can cause diffuse shading on the backside of bifacial modules and reduce the irradiance on them.

A second observation can be made from Figure 4.12. As shown, modeled backside irradiance curves don't match very well to the measured data curve during mid-morning, and mid-afternoon (the period in which the trackers are at the highest angle) and models underestimate the backside irradiance during these times intervals. This behavior is visible on other days during the test as well. Future investigation is required to understand the discrepancy between the modeled and measured data in this study. The discrepancy may be due to the error in modeling reflectivity of the modules, uncertainty of the reported tracker angle, error in irradiance measurements or other factors.

It is also worthwhile to discuss the uncertainty of the measurement while comparing the modeled data with measured data. As an example, an uncertainty analysis is performed for the irradiance measurement taken at SunPower R&D Ranch in Davis, CA on the single-axis tracker system. The uncertainty of such irradiance measurement depends on the uncertainty of other parameters:

62

- Uncertainty of the reference cell (according to the specification sheet) (U_{ref})

- Uncertainty in the albedo measurement (U_{albedo})

- Uncertainty in the installed location of the sensor (U_{height})

- Uncertainty in the measurement of collection unit ($U_{collect}$)

- Uncertainty of the tracker angle (U_{angle})

In this study we assume that other than U_{ref}, U_{albedo}, and U_{height}, other uncertainty values are negligible. According to the specification sheet of the reference cell (EETS), the stated uncertainty is ~3%. However, reference cells usually have a fixed uncertainty offset as well. Since this value is not mentioned in the manufacturer's sheet, a fixed value of ±5 W/m^2 is used similar to the uncertainty study performed on a test system at NREL [42]. Therefore, the total uncertainty for the reference cell is ±5 W/m^2 +3% of the reading value. At lower irradiance, the fixed 5 W/m^2 offset value dominates the total uncertainty and therefore at lower irradiance levels, U_{ref} has a higher value. Using the equation, we calculate U_{ref} for two irradiance levels of 20 W/m^2 and 80 W/m^2 to be 28%, and 9.25%, respectively. The irradiance measurement was performed on a low albedo of ~0.15. Analyzing the measured albedo values during a clear day gives a high albedo uncertainty of 14%. Since, in our setup there is only one reference cell which is fixed at a location, we couldn't calculate U_{height} directly. However, a typical value of 4% is used according to the study in [42].

As shown in [55], the total uncertainty can be calculated as shown in equation (4.3), assuming a coverage factor of 2.

$$U_{tot} = 2 \times \sqrt{\left(\frac{U_{ref}}{\sqrt{3}}\right)^2 + \left(\frac{U_{albedo}}{\sqrt{3}}\right)^2 + \left(\frac{U_{height}}{\sqrt{3}}\right)^2} \quad (4.3)$$

Using this equation, we calculated that the uncertainty of the reference cell irradiance measurement for irradiance levels of 20 W/m^2 and 80 W/m^2 is 36.4% and 19.9% respectively.

5   STUDY OF THE IMPACT OF INSTALLATION PARAMETERS

5.1   Methodology and Simulation Setup

Due to high accuracy of the RADIANCE (raytracing) model, we have used this model to study the impact of different installation parameters on the performance of bifacial systems. Please note that systems considered for this study are fixed-tilt south-facing (azimuth of 180°) systems. Therefore, a similar sensitivity study should be performed for other system configurations such as single-axis tracking and two-axis tracking systems.

As discussed before, unlike monofacial PV systems, dependence of a bifacial PV system's yield on the installation parameters is much more complex and a precise study should be performed to understand the impact of different parameters such as tilt angle, albedo, height, and size of the system. This sensitivity analysis helps to determine the optimum installation parameters for bifacial PV systems.

A few research groups have studied the impact of some installation parameters on the performance of bifacial systems. Using measured data, Castillo-Aguilella *et al*. studied the impact of installation parameters such as tilt angle, height above ground and albedo on the energy yield of small bifacial PV arrays. [48] However, this study didn't consider the effect of size of the system. Yusufoglu *et al.* conducted a comprehensive performance analysis of a single bifacial module [56]. However, more realistic scenarios include a larger number of modules and multiple rows. For these systems, the large shadowing areas cast by the modules on the ground can negatively impact their performance. Kreinin *et al.* studied the design factors such as the height, albedo, and the row spacing in bifacial PV systems and suggested that gains of above 40% are achievable utilizing optimal design parameters [57]. In our work, in addition to studying the impact of parameters such as tilt angle, height and albedo, we examined the impact of system

64

configuration and size on the sensitivity of the performance to each installation parameter. We published this work in IEEE Journal of Photovoltaics [58].

Using RADIANCE raytracing tool (bifacial_radiance), we modeled three systems with different sizes in south-facing configurations, which is the most common way of installing monofacial and bifacial systems. The three systems are as following:

1. Single module

2. A row consisting of five modules (one-row)

3. Five rows, each with five modules (multi-row)

Since the modeling of multiple module configurations requires significant computational resources, we made our analysis feasible by considering the performance of only the middle module in each array. The row spacing for the multi-row case was defined using a value obtained for the shadow length of the row of modules on Dec 21st (winter solstice) when the Sun is the lowest in the sky and casts the longest shadow on the ground; using this length ensures that the modules will be shadow free during the solar window from 9 AM to 5 PM for the entire year [59]. Figure 5.1 shows the three simulated systems with the representative modules in the multi-module systems indicated by red rectangles.
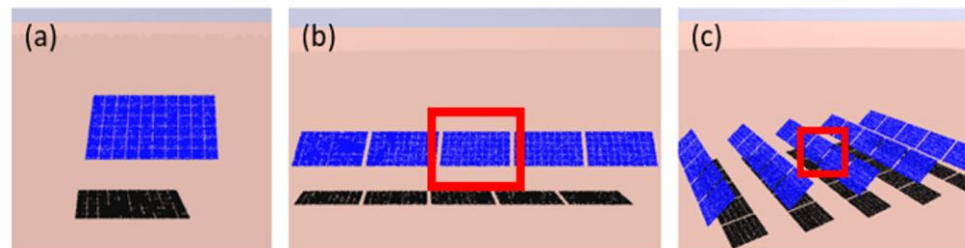
Figure 5.1. Three south-facing PV systems consisting of (a) a single module (b) a row of five modules and (c) five rows of five modules each, were simulated to study the impact of the size on the system performance.

65

In our model, we utilized the dimensions and electrical characteristics of Prism Solar's Bi60-368BSTC bifacial module (front and backside efficiencies of 17.4% and 15.6%, respectively, which is equivalent to a bifaciality factor of ~90%). NREL's National Solar Radiation Data Base (NSRDB) [60] was used to derive typical meteorological year version 3 (TMY3) hourly weather data for Albuquerque, NM (35° N) for global horizontal irradiance (GHI), diffuse horizontal irradiance (DHI) and direct normal irradiance (DNI). Solar azimuth and zenith angles (also hourly data) were calculated using Sandia National Laboratories' PV_LIB Toolbox [61].

Parametric sweeps over three parameters affecting PV system performance were made to study their individual and combined effects. Tilt angle was varied from 5° to 90° (with steps of 5°). Module height above the ground, which is defined as the height of the lower edge of the module, was varied from 0.2 m to 3 m (with steps of 0.2 m). Typical height for ground-mounted systems is 1 m while car-port systems have heights around 3 m. We included three ground materials with different albedos: light soil (21%), beige roofing material (43%) and a white ethylene propylene diene monomer (EPDM) roofing material (81%), which can also represent snow-covered ground. The albedo values for each of the materials were measured at NREL.

We ran hourly simulations sweeping parameters mentioned above around three representative dates of the year: the summer solstice, winter solstice, and fall equinox. Sun position for any day of the year is between the Sun position on the summer solstice and winter solstice, and for the fall equinox the length of the day and night are equal, so the analysis of these three days helps determine the seasonal and annual trends. For each case, we also considered one clear day and one cloudy day to study the impact of cloudy weather condition on the system performance. By comparing the GHI values in TMY3 weather data with the GHI data obtained from Ineichen clear sky model [62, 63], we can determine the clearness of sky for specific days. A parameter

66

called clear sky index (Kc) which is measured GHI divided by clear sky GHI indicates the extent to which the sky was clear on a particular day. Figure 5.2 shows the comparison of GHI data (TMY3 versus clear sky model) for the clear (a, c, e) and cloudy (b, d, f) days around the summer solstice, fall equinox and winter solstice, respectively. Kc values of close to unity in Figure 5.2 (a, c, e) show that the sky on June 20th, September 20th, and December 22nd was clear with a good approximation. However, from Figure 5.2 (b, d, f), we see that the sky on June 23rd was partially cloudy, and on September 23rd and December 21st, it was overcast.
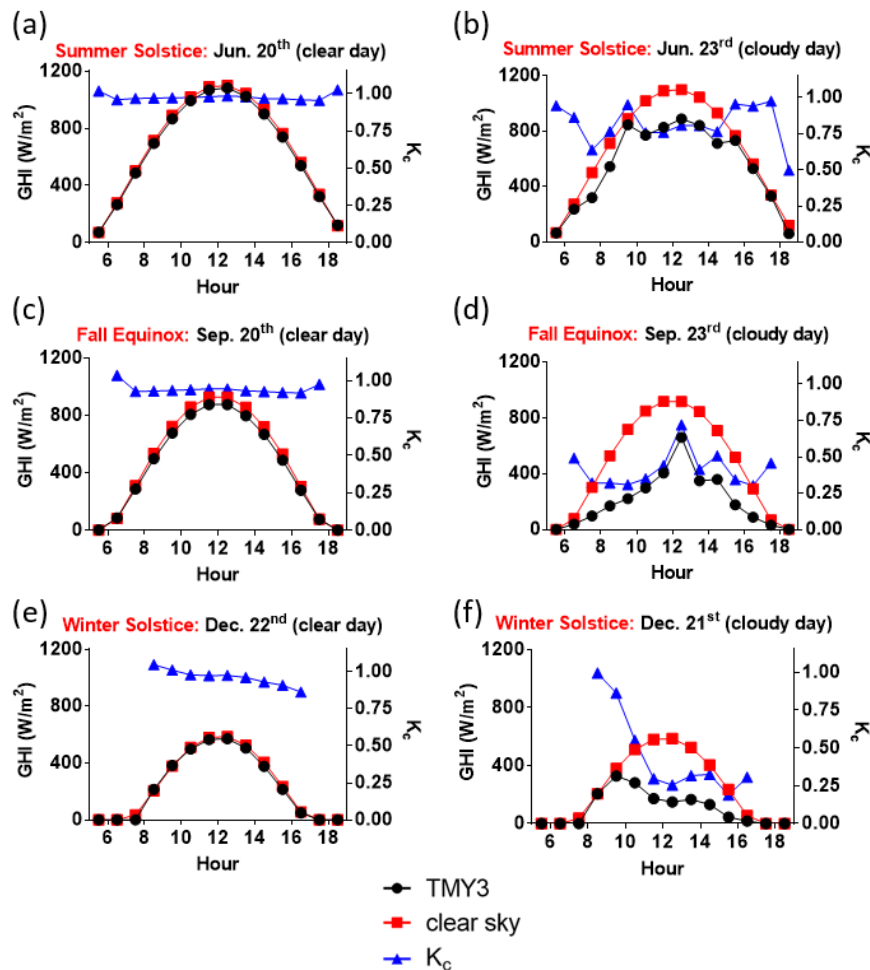
Figure 5.2. Comparison of GHI values of TMY3 weather data and Ineichen clear sky model for the six days in the study.

In this study, in addition to calculation of energy yield, "bifacial gain in energy" (BGE) is also calculated for each case. To calculate daily energy yield and BGE, we used the irradiance data for each of the 60- cells (front and back) in the module at each time step and averaged these values. The average value was multiplied by the effective area of the module and power conversion efficiency value to calculate the power generated by the module. Multiplying the power with the time step (one hour) gives the energy of that particular time period in Watt-hours (Wh). For modeling bifacial modules, we added the front and backside energy to obtain total energy generated by the module. It is important to note that by averaging cell irradiance data, we neglected impact of backside non-uniformity. First, we present and compare the impact of installation parameters on energy yield and bifacial gain of the three PV systems discussed earlier for three clear days shown in Figure 5.1. The effect of cloudy sky condition will be discussed later.

5.2 Tilt Angle

In this section, we investigate the impact of tilt angle on the performance of discussed bifacial PV configurations. Figure 5.3 presents the energy yield and bifacial gain (BGE) as a function of tilt angle for the single module (dotted line), the one-row system (dashed line), and the multi-row (solid line) systems with the albedo of 21% (light soil) and the height of 1.0 m. These plots illustrate that optimum tilt angles for single-module and one-row systems are 5°, 35°, and 65° on summer solstice, fall equinox, and winter solstice, respectively. However, the optimum tilt angles for the multi-row system are higher and are 10°, 40°, and 75° on summer solstice, fall equinox, and winter solstice, respectively. The optimization of tilt angle based on annual results and the reason for higher optimum tilt angles for larger systems will be disccused later in section 5.5.

68

Another important observation from the Figure 5.3 is the anomalous increase (outlined by circles) in the energy yield and BGE of the multi-row system which occurs at tilt angles of 50º, 65º, and 75º for the summer solstice (Figure 5.3 a), fall equinox (Figure 5.3 b), and winter solstice (Figure 5.3 c), respectively. The increase in the BGE indicates that the backside irradiance at these tilt angles is higher for the multi-row system (compared to other configurations). The only reason which can justify this effect is the specular reflection of the light from the modules in the back rows which boosts the backside irradiance.

Figure 5.3. Energy yield and BGE for the single module, one-row system, and multi-row systems as a function of the tilt angle for the albedo of 21% and height of 1 m for clear days around (a) the summer solstice, (b) fall equinox, (c) winter solstice. The circles are added to the data curves to highlight the anomalous increase in the energy yield.

To investigate and quantify the contribution of the reflection from the back rows, we plotted the backside irradiance of multiple cases for the multi-row system on the winter solstice

www.manaraa.com

(Figure 5.4). First, we changed the color of the modules to black (0 % reflectivity in R,G, anf B channels). After simulating the scene, we observed that the backside irradiance decreases but the local maximum at 75° tilt angle still remained (purple diamond curve in Figure 5.4); this was because while we turned the color of the module black, we only effectively eliminated the impact of diffuse reflection. However, the specular reflection from the modules which causes glare [64] and increases the backside irradiance was not eliminated. By changing the texture and material properties of the PV modules, we were able to eliminate the specular reflection as well. Simulating the new scene confirms that the increase of the backside irradiance in a certain tilt angle was due to the specular reflection from the back rows (black cross curve in Figure 5.4) because it elminiates occurance of maximum at 75° tilt angle.
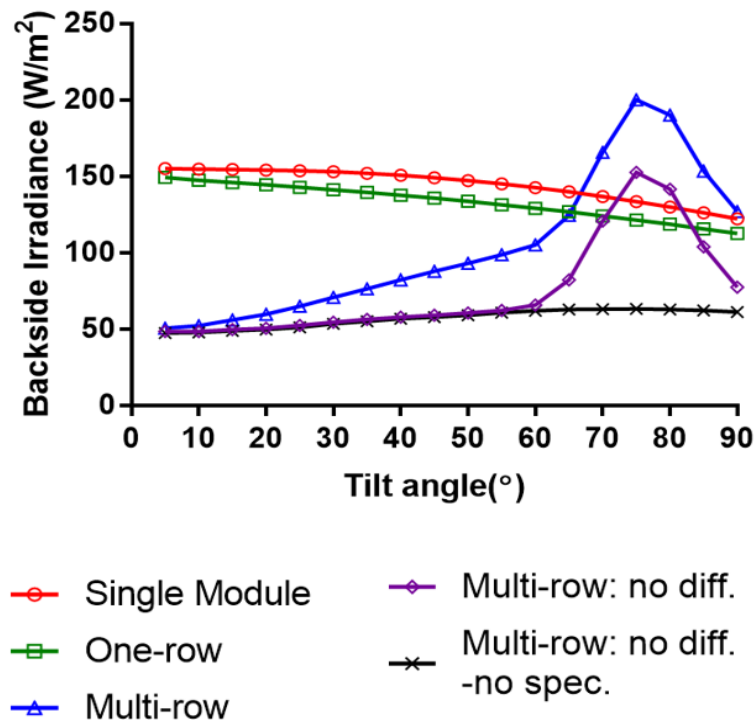
Figure 5.4. Backside irradiance for the single module (red circle), one-row (green square), multi-row (blue triangle), multi-row without diffused reflection (purple diamond), and multi-row without diffused and specular reflection (black cross) for albedo of 21% and height of 1 m in winter solstice.

70

Figure 5.3 shows that the anomalous increase occurs at different tilt angles for different times of the year. For our particular test case, these angles are 50º, 65º, and 75º for the summer solstice, fall equinox, and winter solstice, respectively. However, these angles depend on the row spacing and length of the system as well.

5.3   Height

The height of a bifacial module from the ground also impacts its performance. When the bifacial module is installed close to the ground, backside irradiance is greatly reduced by self-shadowing; by increasing the clearance from the ground, the backside of the module gets more light from both the sky and the ground. However, a saturating effect occurs after certain heights, where the energy yield and BGE do not increase as the installation height increases.

Figure 5.5 shows height dependence of energy yield and BGE of a bifacial PV module for an albedo of 21% and tilt angles of 5º, 35º, and 65º for the summer solstice, fall equinox, and winter solstice, respectively. These tilt angles are chosen because they are close to the seasonal optimum tilt angles for modules with a reasonable clearance (~1 m) from the ground (As will be discussed later, the dependence on the height decreases after a certain height; for clear days, this height value is around 1 m). The data indicate that the rate at which energy yield changes with height for the multi-row system for large installation height values (greater than 1.0 m) is higher compared to the single module and one-row systems, which indicates that the saturation height for larger systems is greater than the smaller systems. In this case, increased height is required to reduce the impact of larger shadowing area and to have a larger field view of the unshaded ground. However, due to the limited extent of the multi-row system, results have been impacted by the edge effect at large heights. To mitigate the impact of this effect, a larger number of rows and modules should be used.

71
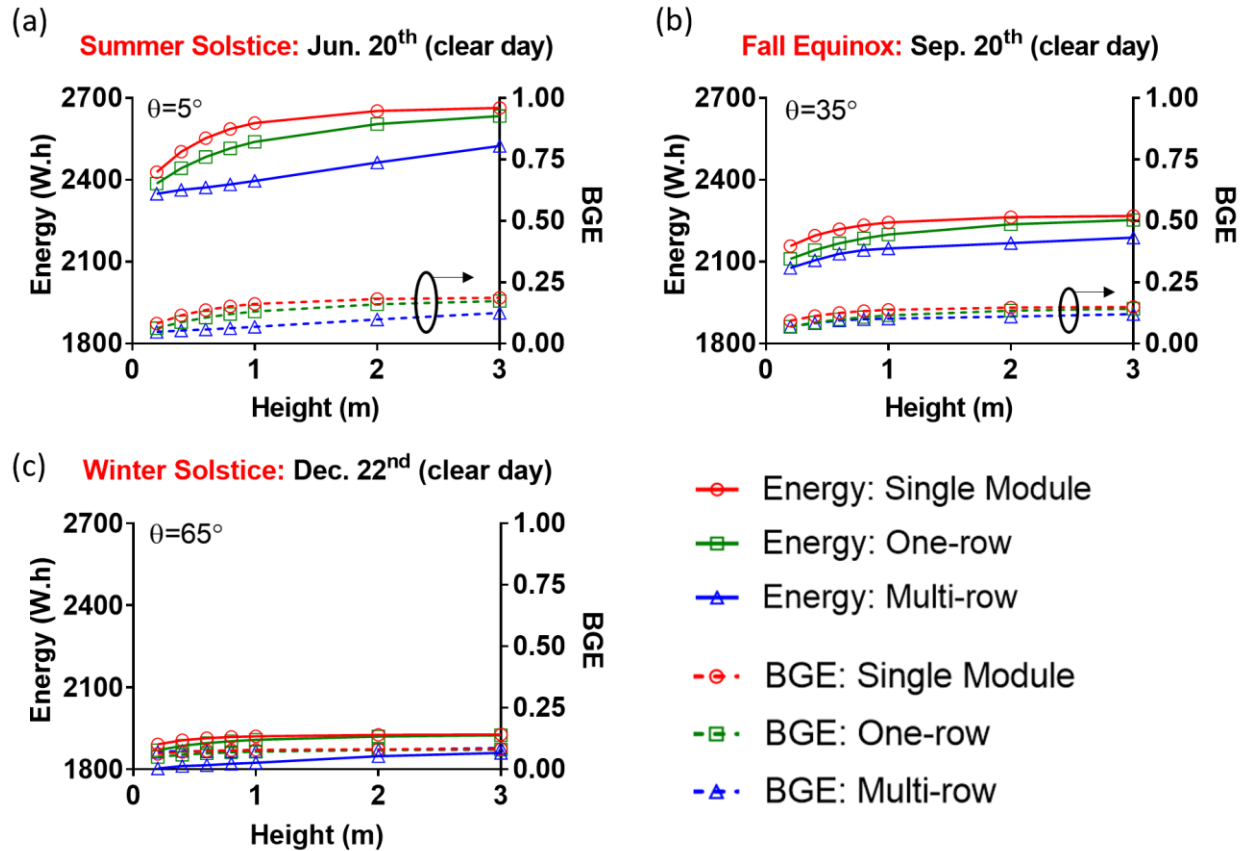
Figure 5.5. Energy yield and BGE for the single module, one-row system, and multi-row systems as a function of the height for the albedo of 21% and tilt angles of 5°, 35°, and 65° for clear days around (a) the summer solstice, (b) fall equinox, (c) winter solstice, respectively.

5.4   Albedo

Increasing the reflectivity (albedo) of the ground increases the intensity of the reflected rays reaching the front and back sides of the module and increases the bifacial system's performance. Figure 5.6 shows dependence of energy yield and BGE for the three system configurations. The results shown in Figure 5.6 are for the height of 1.0 m and the tilt angles of 5°, 35°, and 65° for clear days around the (a) summer solstice, (b) fall equinox and (c) winter solstice, respectively. As shown, there is a linear increase in energy yield and BGE as ground albedo increases. We observe that the slope of the energy yield versus albedo (%) is lower when the

72

module has lower tilt angles. This is due to increased self-shading which reduces ground reflected irradiance's contribution at lower tilt angles.

We also observe lower slope for the multi-row system in Figure 5.6, compared to the one-row and single module systems. The reason is that larger shadowing area due to the multiple numbers of modules reduces the effective albedo in the modules' field of view.
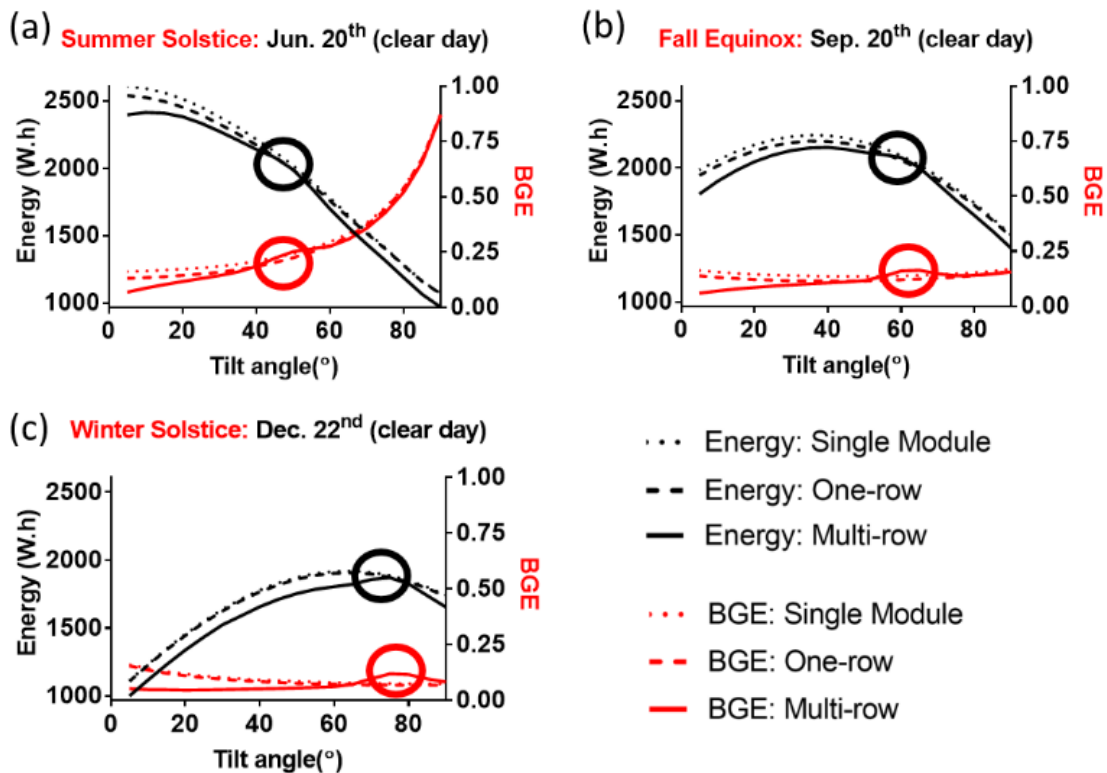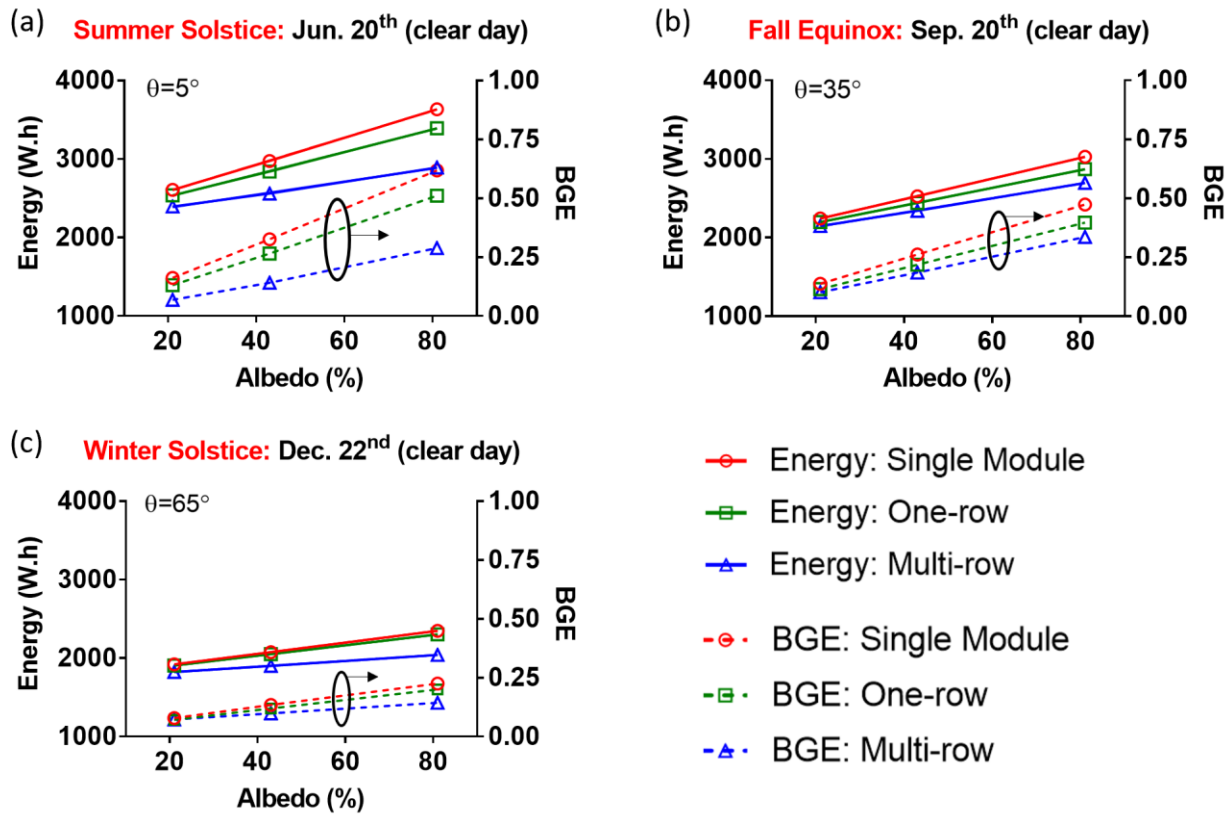

Figure 5.6. Energy yield and BGE for the single module, one-row system, and multi-row systems as a function of the albedo for the height of 1 m and tilt angles of 5°, 35°, and 65° for clear days around (a) the summer solstice, (b) fall equinox, (c) winter solstice, respectively.

5.5   Optimization

The data analysis presented so far indicates that to achieve the highest energy yield, modules need to be installed over the highest possible albedo and the height should be high enough to minimize the self-shadowing effect. However, the seasonal optimum tilt angles vary as a function of time and the specific conditions at the site. We interpolated the simulation data to get a resolution of one degree for tilt angle and determined the seasonal optimum tilt angle on each day of the simulations for different conditions. Figure 5.7 shows the seasonal optimum tilt angle for the three system configurations (single module, one-row, and multi-row systems) for different height and albedo values and for both clear (Figure 5.7 a, c, e) and cloudy (Figure 5.7 b, d, f) days around the summer solstice, fall equinox, and winter solstice, respectively. Seasonal optimum tilt angles for monofacial counterparts of bifacial systems were also calculated theoretically [65] and showed on the plots in Figure 5.7.

The global tilted irradiance includes direct beam, diffuse sky, and diffuse ground-reflected radiation. Their contributions vary depending on PV orientation, location and weather. Comparing the daily optimum angles for clear days (Figure 5.7 a, c, e) with cloudy days (Figure 5.7 b, d, f) shows that the optimum tilt angle for modules not too close to the ground is lower on cloudy sky conditions for both monofacial and bifacial modules (except for the summer solstice in which the optimum tilt angle is slightly higher (3°-5°) on the cloudy day). On cloudy days, the most significant light component received by the modules is the sky diffuse irradiance. By lowering the tilt angle, frontside of the modules see a larger portion of the sky and therefore receive higher sky diffuse irradiance.

74
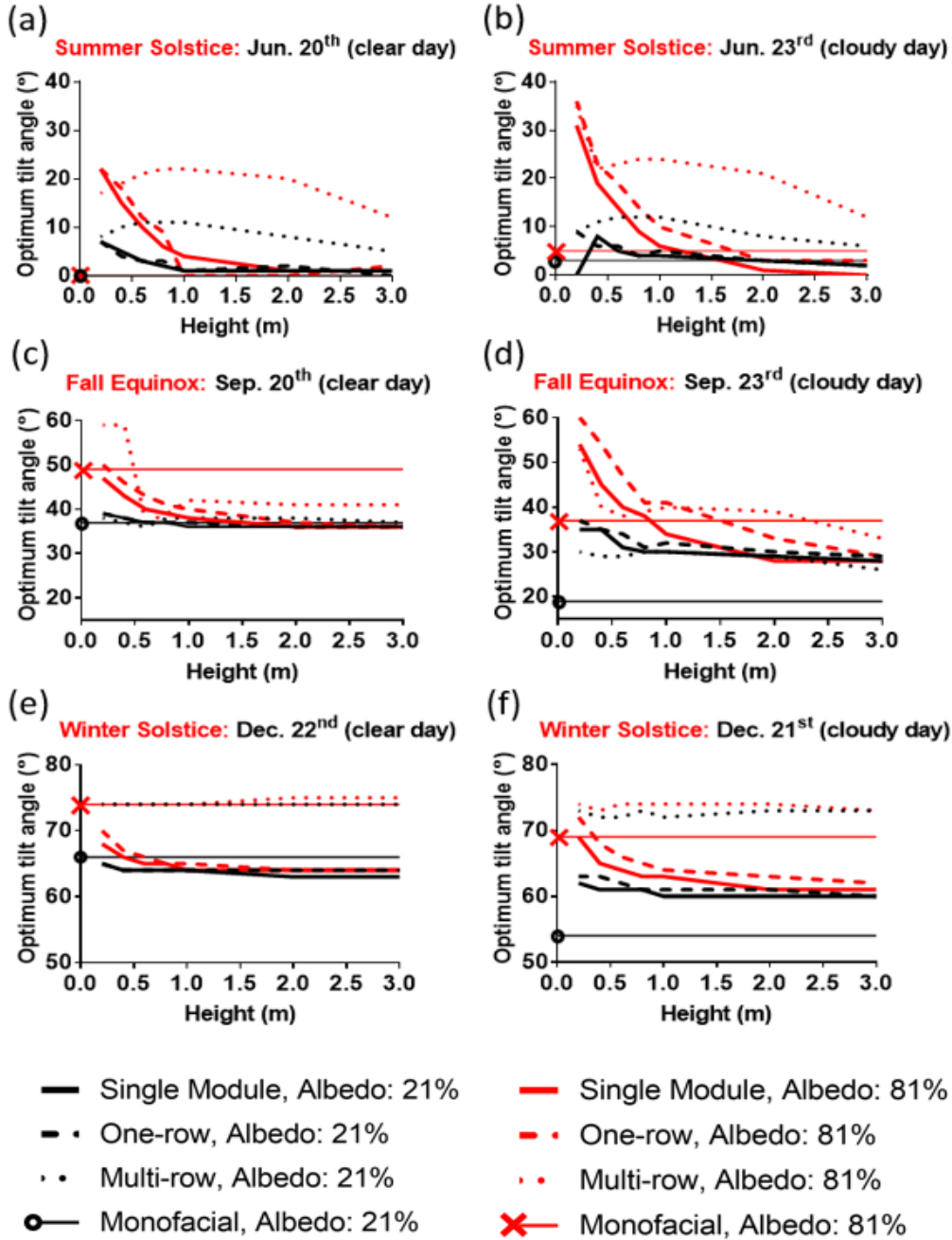
Figure 5.7. Seasonal optimum tilt angle as function of height and albedo for clear (a, c, e) and cloudy (b, d, f) days around the summer solstice, fall equinox and winter solstice. Results are depicted for bifacial single module, one-row and multi-row systems and their monofacial counterparts.

Figure 5.7 also shows that for lower module heights when the system size is not large (single module or one-row system), the seasonal optimum tilt angle for bifacial modules is higher

compared to monofacial modules. The bifacial modules installed close to the ground face large portion of their own shadow and by increasing the tilt angle, the backside of the module receives more light from the ground and sky and sees less of the dark shadowing area. On the other hand, optimum tilt angle of the monofacial modules is not dependent on the height.

Increasing the albedo of the ground increases the ground reflected irradiance that the modules receive. However, for south-facing tilted modules, the amount of this irradiance component is higher on the backside than the frontside. Plots in Figure 5.7 indicate that the higher albedo leads to higher optimum tilt angle for monofacial and bifacial modules (especially in lower height values). Because at higher tilt angles modules receive higher ground reflected irradiance on both frontside and backside.

Another important observation is that, for multi-row bifacial systems, optimum tilt angle can be up to 20º greater than for small-scale bifacial systems. By increasing the number of modules, shadowing area gets larger and to receive more irradiance, tilt angle needs to be higher to diminish the shadowing effect. Unlike bifacial modules, the optimum tilt angle of the monofacial modules is not dependent on the size of the system. The data also indicates that the dependence of the optimum tilt angle (slope) on the height decreases as the height increases and after a certain height the optimum tilt angle is approximately constant. For clear days, this height value is around 1.0 m. However, for cloudy days, this value is usually higher (2.0-3.0 m).

Finding the seasonal optimum tilt angle would be beneficial for the systems with a control on adjusting the tilt angle. A controller can be designed to adjust the tilt angle with respect to the weather condition and the position of the Sun. However, for the fixed-tilt systems, it is more relevant to perform annual simulations to find the annual fixed optimum tilt angle for the system. Using cumulative sky approach within RADIANCE, we conducted annual simulations to find the

76

energy yield of the systems. To study the dependence of the systems' performance on the latitude and climate type, two different locations were chosen (Table 5.1). Climate types are according to the Köppen climate classification. [66]

Table 5.1. Characteristics of the sites used in the study of finding annual optimum tilt angle.

Location	Latitude	Climate Type
Albuquerque, NM	35.1º	BSk: cold semi-arid climate
Anchorage, AK	61.2º	Dfc: Subarctic climate

Figure 5.8 (a) and Figure 5.8 (b) show the annual optimum tilt angle for the single module and multi-row systems in Albuquerque, NM, and Anchorage, AK, respectively. A clear difference is observable between the optimum tilt angles of the two systems. For both locations, the dependence of the optimum tilt angle on the height is negligible for heights larger than one meter. In Albuquerque, the optimum tilt angle for the single module is ~35º (for heights higher than one meter) which is the latitude of the site. This analysis shows that the optimum tilt angle of a bifacial single module would be similar to the monofacial equivalent system in Albuquerque. However, the multi-row system which consists of 25 modules have higher optimum tilt angle and this value is dependent on the albedo. For albedos of 21%, and 81%, the optimum tilt angle is ~36º and 40º, respectively. For grounds with high albedo, the tilt angle needs to higher because of the reasons explained earlier in this section. For a higher latitude location like Anchorage, the trend is opposite. Multi-row systems have lower optimum tilt angles than the single module. The reason is that the row spacing for these systems are chosen to be equal to the row spacing of the systems in Albuquerque. This means that the modules are not shadow-free for the entire year and they experience partial shading on the frontside, especially in the winter (to have a shadow-free system for the entire the year in Anchorage, the row spacing should be very high (~12 m) which is not

77

practical and economical). Lower tilted modules cast a shorter shadow on the ground and reduce the frontside shading which is why the optimum tilt angle for larger systems is lower than the single module systems.
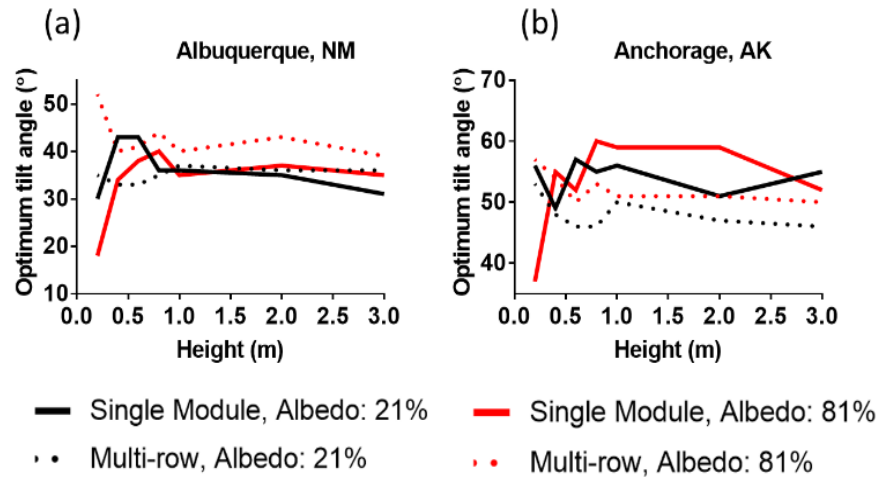
Figure 5.8. Annual optimum tilt angle for systems in (a) Albuquerque, NM and (b) Anchorage, AK.

5.6   Impact of Size of the System

Using the optimum tilt angle for the module height of 1.0 m and albedo of 21%, we compared the energy yield and BGE of the three PV configurations for Albuquerque, NM. The data is shown in Figure 5.9. Energy and BGE values of the equivalent monofacial system (single module) are also shown for the same height and albedo values. The results indicate that by increasing the number of modules, energy yield decreases significantly. The middle module in the multi-row system has about 7% lower energy yield than the single module system on the summer solstice. This value for fall equinox and winter solstice is about 4% and 3%, respectively. We found from our simulation data (not shown here) that for the albedo of 81%, modules in large PV arrays can have up to 14% lower performance compared to single module systems. Figure 5.9 also shows that highest bifacial gain is for the single module system and drops as the system size gets larger.
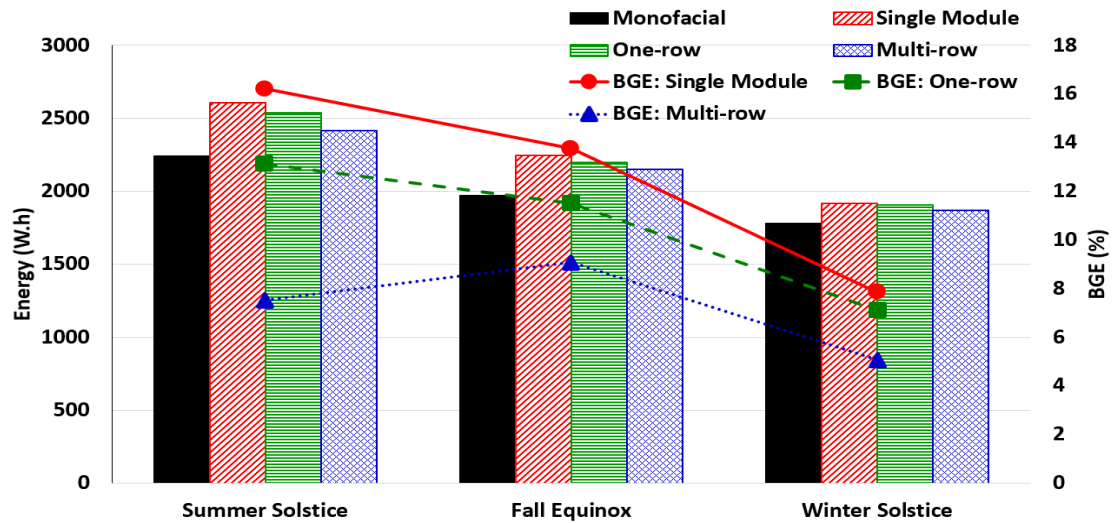
Figure 5.9. Energy yield and BGE of the single module, one-row and multi-row PV systems for optimum tilt angle at the module height of 1 m and albedo of 21% for clear days on the summer solstice, fall equinox and winter solstice.

The decrease in the performance of the larger systems can be because of various reasons. First, larger systems cast larger shadows on the ground, and it reduces the backside irradiance and the total performance of the system. The second reason is the blocking of the direct and diffuse irradiance by front and back rows of the module. As mentioned earlier, the spacing between the rows is large enough and ensures that the modules are shadow free during the solar window from 9 AM to 5 PM the entire year. This guarantees that there is only a minor reduction in total energy because of direct blocking of the sunlight onto the modules, and the modules can only block diffuse and reflected rays from the ground during the most time of a day. Quantifying the losses due to these reasons requires decoupling the shadowing and blocking effects. To do so, we conducted a few more simulations. These simulations were run for Albuquerque, NM (Sep. 20th). First, we mapped the shadow pattern of the multi-row system onto the ground while simulating the scene for only a single module (Figure 5.10). This eliminates the blocking effect of the front and back rows while keeping the shadowing effect unchanged. Subtracting the results of the multi-row

79

system from the results of this simulation gives us the loss due to the horizon blocking. However, as we saw earlier, reflection from the surrounding modules (especially the back row) would increase the irradiance to some extent. To account for this effect, we simulated another multi-row scene with non-reflective (black and textured) modules. Table 5.2 shows the results of the simulations for the different scenes on Sep. 20th (with the same installation parameters: height =1.0 m, albedo = 21%, and tilt angle = 35°).
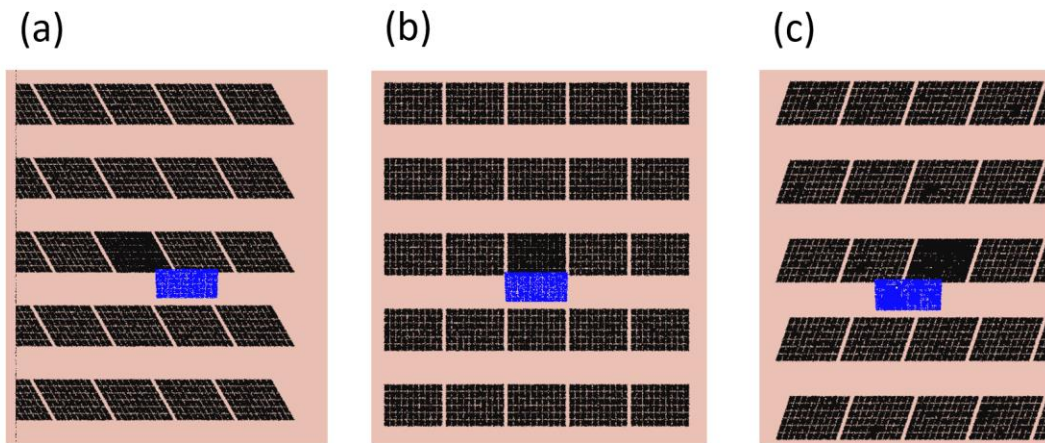
Figure 5.10. Single module with mapped shadow pattern of the multi-row system on the ground at (a) 10 am, (b) 12 pm, and (c) 2 pm.

The difference in the performances of the scenes 1 and 2 (95 Wh) is the total loss in the energy yield of the middle module in the multi-row system, compared to a single module. The difference between the daily energy yield of the scenes 2 and 3 (34Wh) represents the energy gain of the multi-row system due to the reflection from the back-row modules. The difference between the performance of the scenes 3 and 4 shows the horizon blocking effect of the surrounding modules (45 Wh). This analysis shows that while the multi-row system produces 34 Wh more energy than the single module due to the reflection from the modules in the back row, it generates 45 Wh, and 85 Wh less energy due to the horizon blocking and shadowing effects, respectively (which results in a total of 95 Wh lower energy yield than the single module system).

80

Table 5.2. Energy yield of the simulated scenes to identify the reasons for lower production of larger bifacial systems.

Scene	Daily Energy Yield (Wh)
1. single module system	2244
2. multi-row system	2149
3. multi-row system- no reflection	2115
4. single module- with mapped shadow	2160

6 PERFORMANCE COMPARISON OF VERTICAL EAST/WEST FACING VS TILTED SOUTH/NORTH-FACING SYSTEMS

Since the emergence of bifacial PV technology, vertical modules have always been considered as an interesting and feasible installation option. In this section, a comparison between the performance of two popular installation configurations for bifacial modules was performed:

1) Optimally tilted south/north-facing module ($Bi_{S/N}$)

2) Vertical east/west-facing module ($Bi_{E/W}$)

A few research groups have studied the performance of vertical bifacial PV systems. Guo, *et al.* compared the performance of vertical east/west-facing modules to the traditional monofacial PV systems and showed that depending on the latitude, diffuse fraction and the albedo, vertical bifacial PV systems may have higher energy yield than south-facing monofacial PV systems [17]. In [67], it was shown that for a reasonable clearance from the ground (one meter), $Bi_{S/N}$ always performs better than the $Bi_{E/W}$. However, these results assume that there is no direct and diffuse shading due to the surrounding objects. Presence of such objects may block the direct and diffuse light from getting absorbed by the modules and reduce their performance. In this work, we study the effect of surrounding objects on annual energy yield of both $Bi_{S/N}$ and $Bi_{E/W}$ and compare their performance under different shading conditions. We seek to determine that under what shading conditions $Bi_{E/W}$ will outperform the $Bi_{S/N}$.

6.1 Shade-free Simulations

Before studying the impact of surrounding objects on the performance of bifacial PV modules, the performance of $Bi_{S/N}$ and $Bi_{E/W}$ without any objects in their surroundings are modeled for multiple locations listed in Table 6.1.

For both cases of $Bi_{S/N}$ and $Bi_{E/W}$, we simulated a single bifacial module with a height of 1 m above the ground and albedo of 21% (light soil) using RADIANCE. As in the previous section, we used Prism Solar's Bi60-368BSTC bifacial module's characteristics in our simulations. As shown before, optimum tilt angle for south/north-facing modules depends on multiple parameters such as height, albedo of the ground, and size of the system. However, a good approximation of optimum tilt angle for a reasonable height from the ground (1 m) and albedo (21 %) is the latitude of the location. Therefore, in the simulations, we set the tilt angle of $Bi_{S/N}$ to be equal to site's latitude. It is worth noting that this study did not consider the effects of multiple modules per row nor multiple rows of modules and associated row to row shading. The rendered scenes for $Bi_{S/N}$ and $Bi_{E/W}$ systems are shown in Figure 6.1.

Table 6.1. Coordinates of the sites used in the RADIANCE simulations to compare performance of $Bi_{S/N}$ and $Bi_{E/W}$ systems.

Location	Latitude	Longitude
Singapore, Singapore	1.17º N	103.50º E
Hawaii, USA	19.73º N	156.05º W
Cairo, Egypt	30.04º N	31.24º E
Albuquerque, USA	35.09º N	106.61º W
Beijing, China	39.90º N	116.41º E
Paris, France	48.86º N	2.35º E
Anchorage, USA	61.22º N	149.90º W
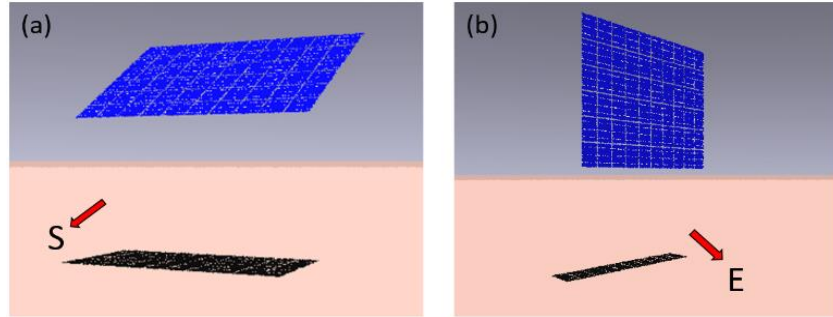
Figure 6.1. Optimally tilted south/north-facing module (a), and vertical east/west-facing module (b) rendered scenes in RADIANCE.

Figure 6.2 shows the results of RADIANCE simulations for locations listed in Table 6.1. We observe that for all locations, except Singapore, the $Bi_{S/N}$ performs better than $Bi_{E/W}$. Because of a very low latitude in Singapore (1.17°) and therefore a very low tilt angle for $Bi_{S/N}$, performance of this system is adversely affected by self-shading and therefore the yield of $Bi_{S/N}$ is slightly lower than $Bi_{E/W}$ for Singapore. Also, that for high latitudes, the energy yield of $Bi_{S/N}$ and $Bi_{E/W}$ as well as their difference is lower, because global horizontal irradiance is usually lower for the high latitude locations compared to sunnier locations with lower latitude.
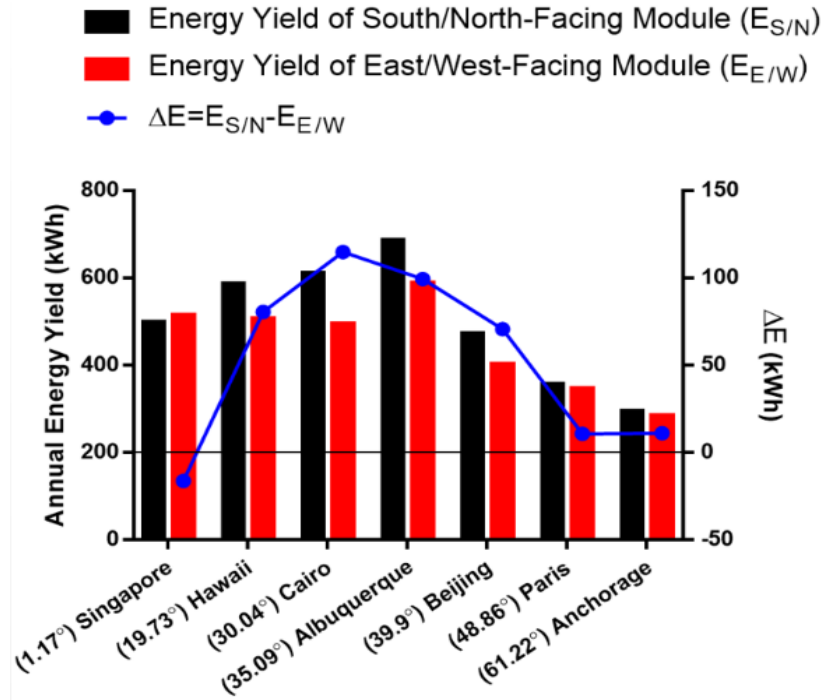
Figure 6.2. Comparison of the performance of $Bi_{S/N}$ and $Bi_{E/W}$ PV systems indicates that for systems installed in Singapore yield of $Bi_{S/N}$ is slightly lower than $Bi_{E/W}$ while for all other locations the $Bi_{S/N}$ systems have higher yield than $Bi_{E/W}$.

6.2 Impact of Surrounding Obstructions

Presence of surrounding obstructions can decrease the field view of the PV module to the sky and hence decrease its annual energy yield. Also, the obstructions may occasionally block the direct light from the Sun which has a significant impact on the PV system performance.

Using the RADIANCE simulation tool, we calculate the annual energy loss due to horizon obstructions. We assume to have cubic shape obstructions which can resemble surrounding buildings. We characterize obstructions with four parameters of height (h), width (w), azimuth angle (φ), and distance from the module (r) as shown in Figure 6.3. The range for these parameters is shown in Figure 6.3 as well. A parametric sweep study over these parameters is performed for both $Bi_{S/N}$ and $Bi_{E/W}$ and the energy loss due to each type of obstruction was calculated. Step size in the sweep for parameters h, w, φ, and r was 5 m, 10 m, 30°, and 10 m, respectively. We chose the material of the obstruction to be concrete which exhibits surface reflection of 28%.

85
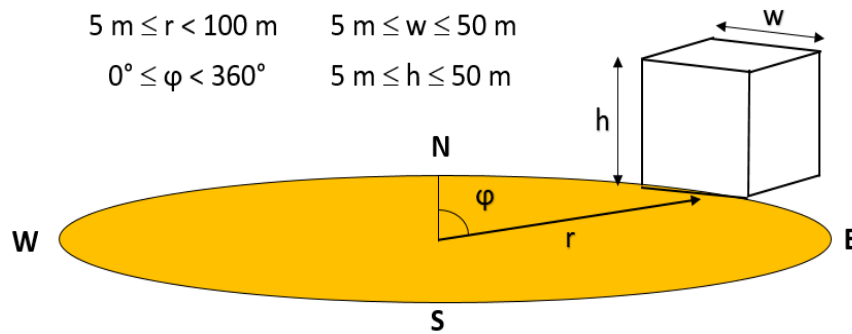
Figure 6.3. Schematic of the horizon obstruction in the simulations and the range of the parameters in the sweep.

As discussed previously, we seek to find the characteristics of the obstructions whose presence cause $Bi_{E/W}$ to perform better than $Bi_{S/N}$. We performed this analysis for two locations of Albuquerque, NM and Anchorage, AK. As shown in Figure 6.2, these two locations represent two extremes in terms of the total energy yield and weather types.

To identify such obstructions, we used J48 classification algorithm [68] in Weka; a data mining software [69]. J48 is an algorithm which generates pruned/unpruned decision trees. Our features are the obstruction's four parameters (h, w, φ, and r) and the class labels are:

- Y: The energy yield of $Bi_{E/W}$ is more than the $Bi_{S/N}$

- N: The energy yield of $Bi_{E/W}$ is less than the $Bi_{S/N}$

We generated heavily pruned decision trees for both locations and identified the Y class labels in the leaves of the tree. The accuracy of the classifiers is 99.3% and 97.8% for Albuquerque, NM and Anchorage, AK, respectively. Figures 6.4 (a) and (b) show the characteristics (feature range) of the obstruction with class label Y (higher energy yield for $Bi_{E/W}$ than for $Bi_{S/N}$) for Albuquerque, NM and Anchorage, AK, respectively.

(1)

$r \leq 5\,m$
$120° < \varphi < 180°$
$w = 5\,m$
$10\,m \leq h$

(2)

$r \leq 5\,m$
$120° < \varphi < 210°$
$5\,m \leq w$
$10\,m \leq h$

(3)

$5\,m \leq r \leq 15\,m$
$120° < \varphi < 210°$
$15\,m \leq w$
$25\,m \leq h$

(a)

Anchorage, AK

(1)

$r \leq 5\,m$
$210° < \varphi \leq 240°$
$15\,m < w$
$5\,m \leq h$

(2)

$r \leq 5\,m$
$180° < \varphi \leq 210°$
$w = 5\,m$
$10\,m < h$

(3)

$r \leq 5\,m$
$120° < \varphi \leq 210°$
$15\,m \leq w$
$5\,m \leq h \leq 10\,m$

(4)

$r \leq 15\,m$
$120° < \varphi \leq 180°$
$w = 5\,m$
$10\,m < h$

(5)

$r \leq 35\,m$
$120° < \varphi \leq 210°$
$5\,m < w$
$10\,m < h$

(6)

$35\,m < r \leq 65\,m$
$120° < \varphi \leq 180°$
$15\,m \leq w$
$25\,m < h$

(b)
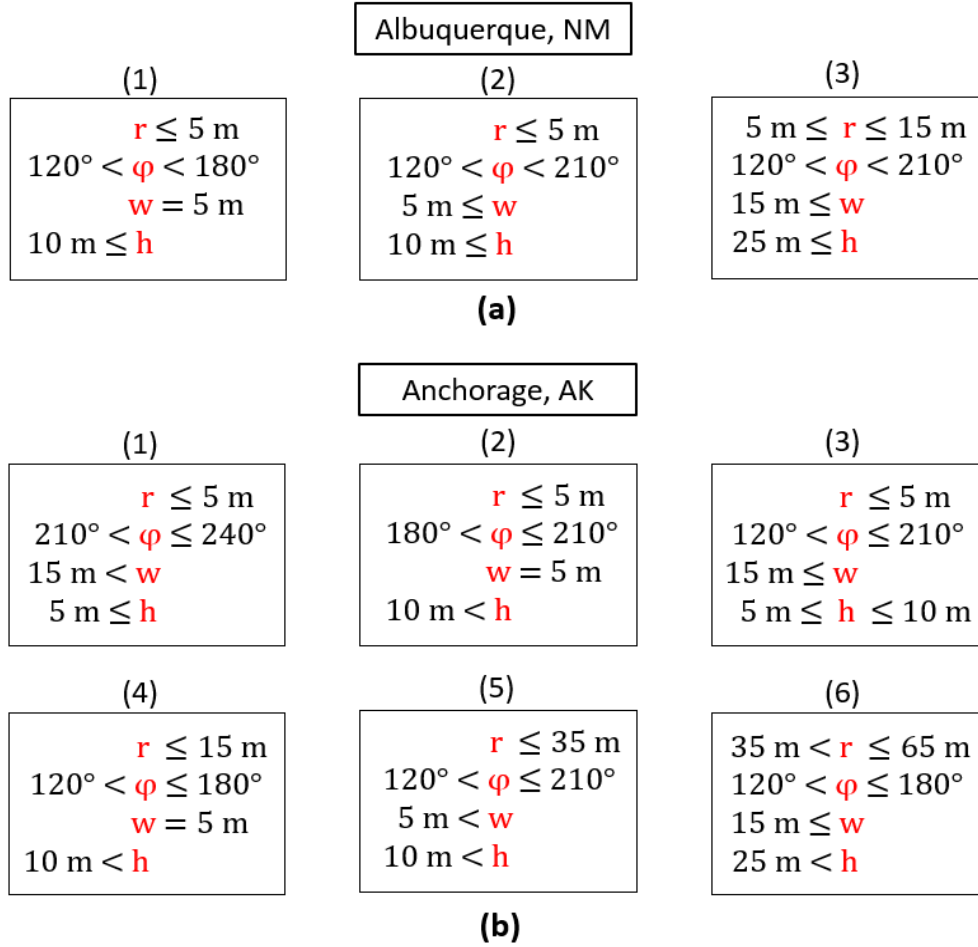
Figure 6.4. Characteristics of the obstruction which cause $Bi_{E/W}$ system to have higher energy yield than $Bi_{S/N}$ for Albuquerque, NM (a) and Anchorage, AK (b).

From Figure 6.4 (a) we observe that we can classify the obstructions which cause $Bi_{E/W}$ to perform better than $Bi_{S/N}$ in Albuquerque, NM into three categories. Investigating the characteristics of these obstructions reveals that all of them correspond to large obstructions in south ($120° < \varphi < 210°$) which are also very close to the module ($r \leq 15$). Having such obstructions block the direct and diffuse light on the modules. However, $Bi_{S/N}$ module is impacted more by the shading. The main irradiance source of the $Bi_{S/N}$ module is from its front side and if that view of the module is blocked then its performance will be decreased significantly. $Bi_{E/W}$ performs better under these shading conditions because it doesn't receive much irradiance from south and blocking that view would have less impact on $Bi_{E/W}$ modules. To compare the size of the obstruction from

the view of the module, elevation angle (El_{obs}) and azimuth span angle (Az_{obs}) of the obstruction with respect to the bottom of the module were calculated using following equations:

$$El_{obs} = Arc\tan(\frac{h-1}{r}) \quad (6.1)$$

$$Az_{obs} = 2Arc\tan(\frac{W}{2r}) \quad (6.2)$$

Schematic of the obstruction with defined parameters of El_{obs} and Az_{obs} are shown in Figure 6.5. Note that the elevation angle is calculated from the bottom of the modules which is one meter above the ground. These parameters are calculated for the middle cell at the bottom of the module. For other cells, the El_{obs} and Az_{obs} parameters will be slightly different.
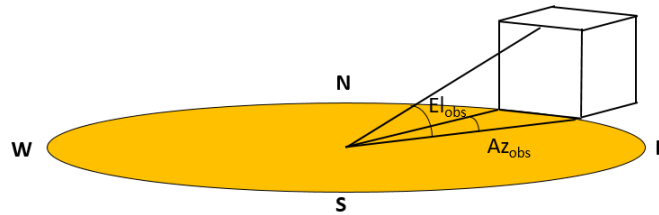
Figure 6.5. Schematic of the obstruction with defined parameters of El_{obs} and Az_{obs}.

Figure 6.6 shows examples of the obstruction from the three categories shown in Figure 6.4 (a). These examples of obstructions have minimum elevation angle and azimuth span angle and the median azimuth angle from the ranges shown in Figure 6.4 (a). These obstructions are plotted in the 2-D plane of the sky dome along with the Sun paths on the summer solstice, and winter solstice for Albuquerque, NM. Any obstruction with higher elevation angle or azimuth span angle will cause $Bi_{E/W}$ to have higher energy yield than $Bi_{S/N}$.
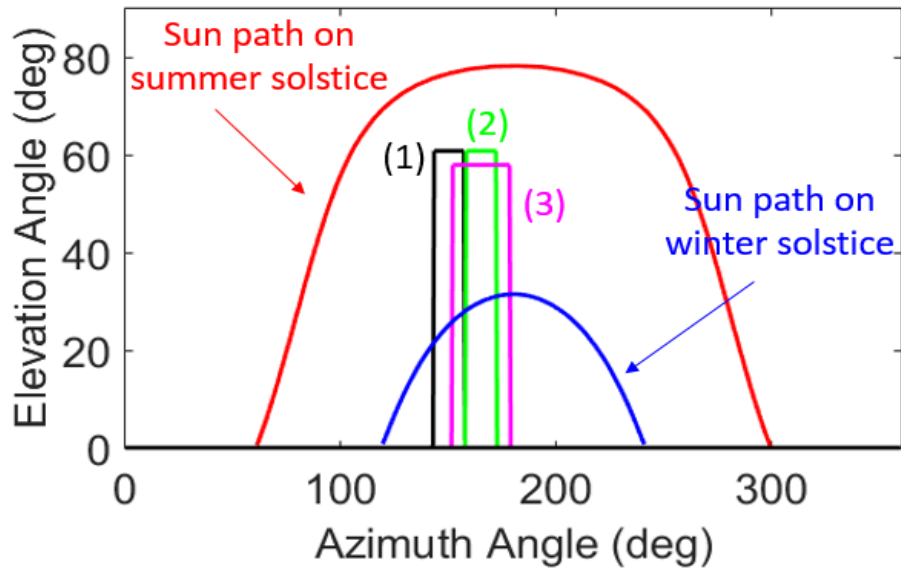
Figure 6.6. Examples of obstructions from three categories in Figure 6.4 (a) (Albuquerque). Any obstruction larger than shown obstructions will result in higher energy yield for $Bi_{E/W}$ than $Bi_{S/N}$.

As discussed previously, we observe from Figure 6.6 that these obstructions are very large and block the Sun path around late morning and solar noon for many days in a year. This means that the modules experience heavy direct shading under these shading scenarios. However, $Bi_{S/N}$ system would be impacted more by this shading since it is facing the obstruction directly and large portion of its front side irradiance is blocked by the obstruction. This finding may not be very valuable, since it is evident that the modules shouldn't be installed close to large obstructions. We are more interested in the shading conditions which may not seem evident.

Following the same procedure, in Figure 6.7, we show examples of the obstruction from the six categories shown in Figure 6.4 (b) for Anchorage, AK. These obstructions have minimum elevation angle and azimuth span angle and the median azimuth angle from the ranges provided in Figure 6.4 (b). Note that the categories shown in Figure 6.4 (b) overlap with each other for certain range of the obstruction characteristics.
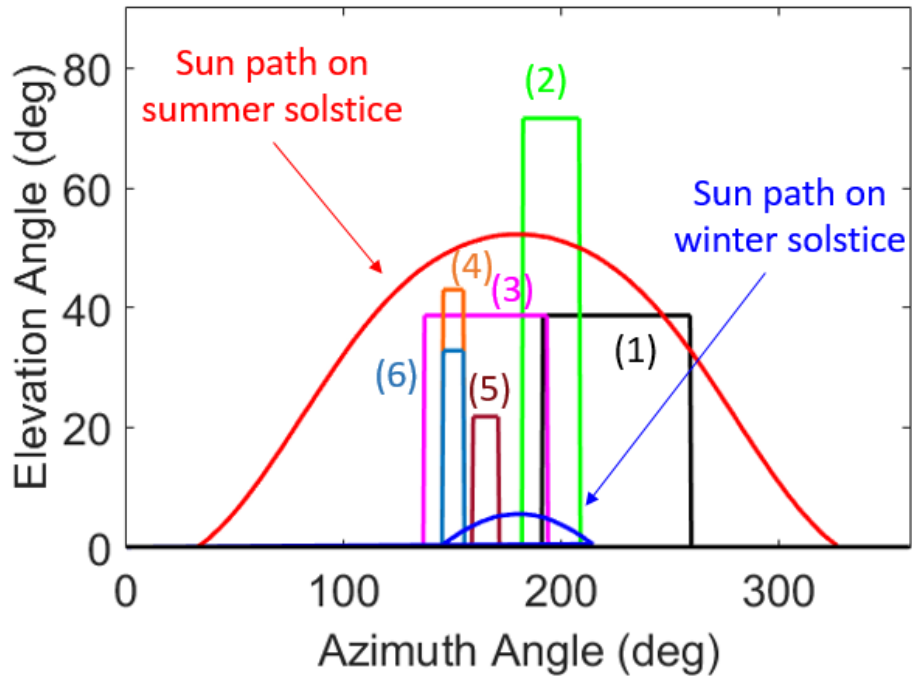
Figure 6.7. Examples of obstructions from six categories in Figure 6.4 (b) (Anchorage). Any obstruction larger than shown obstructions will result in higher energy yield for $Bi_{E/W}$ than $Bi_{S/N}$.

Similar to Figure 6.6, we observe that three examples of (1) - (3) in Figure 6.7 are very large obstructions at south and evident that $Bi_{S/N}$ would perform poorly if installed facing them. However, by comparing Figure 6.7 with Figure 6.6, we see that so much smaller horizon obstructions can also cause $Bi_{E/W}$ to have higher energy yield than $Bi_{S/N}$ (examples (4) - (6) in Figure 6.7). This can be explained by two reasons. First, as we see from Figure 6.2, energy yield difference between $Bi_{E/W}$ and $Bi_{S/N}$ is smaller for higher latitudes locations such as Anchorage and having a much smaller obstruction at south would be enough to cause $Bi_{S/N}$ to have lower yield compared to $Bi_{E/W}$. The second reason is that as shown in Figure 6.7, the elevation angle of the Sun is lower for Anchorage than Albuquerque and having an even small obstruction can cause direct shading on $Bi_{S/N}$ module for long periods throughout the year.

This analysis suggests that in higher latitude locations, for certain obstruction types, $Bi_{E/W}$ becomes a better option in terms of high annual energy yield. In this work, we used annual energy

90

yield as a metric to compare bifacial PV systems. However, $Bi_{E/W}$ produces more energy earlier and later in the day which can be more valuable PV energy production in some locations where energy demand peaks in the morning and evenings. Also, there is a special interest in vertical modules in some locations due to their lower soiling and snow loss compared to tilted modules. [70-72]

7   MODELING BIFACIAL TANDEM PV SYSTEMS

A tandem solar cell consists of different cells which split the solar spectrum and use an optimized absorber material for each section of the solar spectrum to increase the overall efficiency of the solar cell. For example, in a two-layer tandem solar cell, top cell absorbs the photons with higher energy and the bottom cell absorbs the low energy photons. Combining the higher energy yield of bifacial PV systems with higher efficiency of silicon-based tandem devices can further increase the performance of PV systems and lower LCOE. As a collaborative project between Arizona State University and University of Iowa, we modeled the performance of bifacial tandem PV systems. The project work involved RADIANCE modeling of the tandem PV systems by the University of Iowa team and then the results were input to a custom tandem-device model developed by the Arizona State University to compute predicted power output of the tandem PV systems.

7.1   RADIANCE Modeling

Following the method in [39], the algorithm for running a RADIANCE simulation was modified to perform spectrally resolved simulations. A python script was written to repeatedly get the spectrally resolved DNI, DHI, and material reflectivity values to run RADIANCE simulations for each wavelength of interest. The simulations were performed to model the front and backside irradiance from 300 to 1250 nm with 10 nm resolution.

We used typical meteorological year (TMY) spectral weather data from NREL's NSRBD [60] to derive irradiance data for Phoenix, Arizona. Two days close to the fall equinox; one clear, one cloudy were selected for study based on their clear sky index. Spectral reflectance data for the materials in the scene, such as the ground (brown loam, dry grass, or white sand) and racking system, were obtained from the ASTER (Advanced Spaceborne Thermal Emission and Reflection

Radiometer) spectral library published by NASA. [73] For the reflectance of the PV modules, front and rear direct and diffuse reflectances were determined by simulating state-of-the-art perovskite/c-Si tandem modules with the software SunSolve. [74]

The model was used to simulate a utility-scale fixed-tilt system and a single-axis tracking (SAT) system with three rows and 15 modules each. GCR was selected to be 0.35 for these systems. Irradiance was calculated on the front and back sides of the middle module in the middle row as this module is the most representative of the modules in a very large PV plant. Figure 7.1 (a) show a rendered image of a single-axis tracking system (including racking system: piles and torque tube). Figure 7.1 (b) shows spectrally resolved simulated irradiance data for SAT system in Phoenix, AZ at noon for different constant and natural materials.
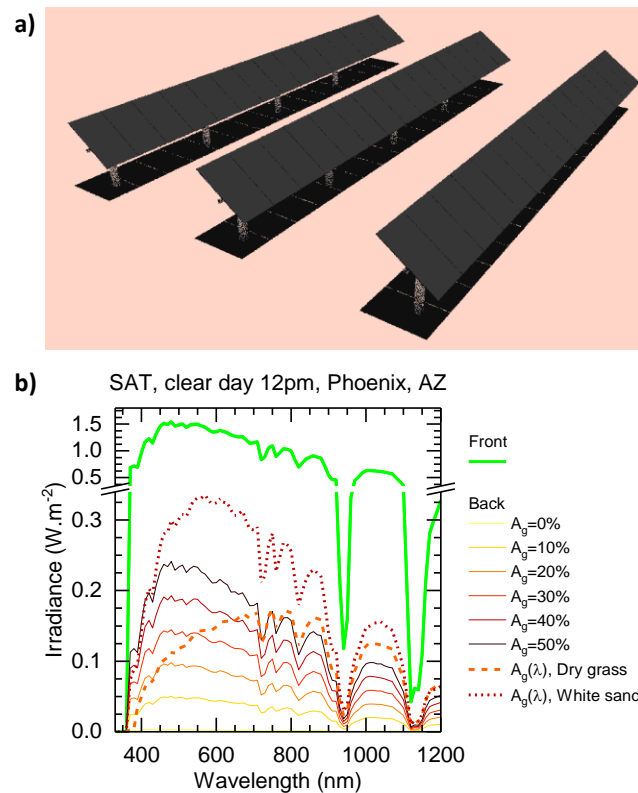
Figure 7.1. (a) Rendered scene of a three-row single-axis tracking system using RADIANCE. (b) Spectrally resolved simulated irradiance data for a single axis-tracking system in Phoenix, AZ at noon.

93

7.2   Custom Tandem Device Model

To take into account current matching between a top cell of arbitrary bandgap and the bottom c-Si cell, which are series-connected in a two-terminal structure, we adopted an approach similar to Onno *et al*. [75] In particular, the $J(V)$ curve of each sub-cell was constructed with a triple-diode model [75]—with each diode representing an independent recombination mechanism—using a short-circuit current density (J_{sc}) determined via SunSolve, and matching the open-circuit voltage (V_{oc}) to that of representative measured sub-cells by adjusting each cell recombination current density $J_{0,SRH}$. With the individual sub-cell $J(V)$ curves in hand, the maximum-power-point and efficiency of the tandem were calculated by enforcing current matching. This procedure was performed for the three device structures illustrated in Figure 7.2.

94
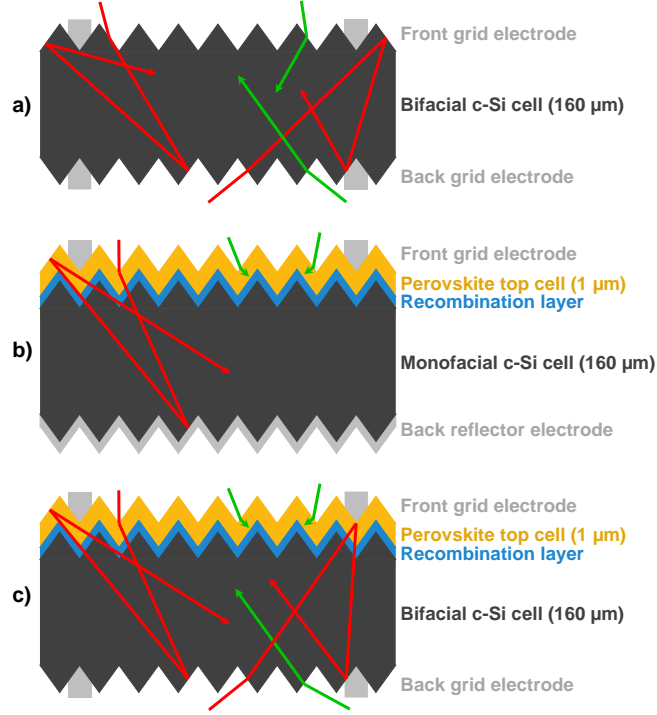
Figure 7.2. Schematics of the three structures modeled: (a) bifacial single-junction c-Si cell, (b) monofacial perovskite/c-Si tandem, (c) bifacial perovskite/c-Si tandem. Examples of pathways for short-wavelength and long-wavelength photons are displayed with green and red arrows, respectively.

7.3 Results and Discussion

7.3.1 Effective Photon-flux Albedo, A_{eff}

In order to compare between these different scenarios, we define a metric of the actual current boost in the bottom cell due to bifaciality under realistic conditions, the *effective photon-flux albedo, A_{eff}*:

$$A_{eff} = \int_{\lambda=300}^{\lambda=1200} \Phi_{back}(\lambda)d\lambda \Bigg/ \int_{\lambda=300}^{\lambda=1200} \Phi_{front}(\lambda)d\lambda \qquad (7.1)$$

Here, $\Phi_{front/back}$ are the photon fluxes on the front and back of the modules, respectively, irrespective of the scenario. Hereafter, we interchangeably use *effective photon-flux albedo* and the simpler *effective albedo* to describe A_{eff}.

95

7.3.2 Impact of Variations in Effective Albedo on the Power Production

The simulations were conducted for various ground albedos (A_g), cloudy versus clear days, fixed-tilt systems versus those on single axis tracking (SAT) systems. An important result of the study is shown in Figure 7.3, which reveals that variations in the effective albedo are relatively benign: for the large majority of the effective albedos encountered on both clear and cloudy days, a bifacial tandem module with the right top-cell bandgap will produce above 95% of its optimum power output. This means, for example, that a bifacial tandem that operates with 30% efficiency at its design albedo will nearly always operate above 28.5% in the field (neglecting, e.g., temperature effects).
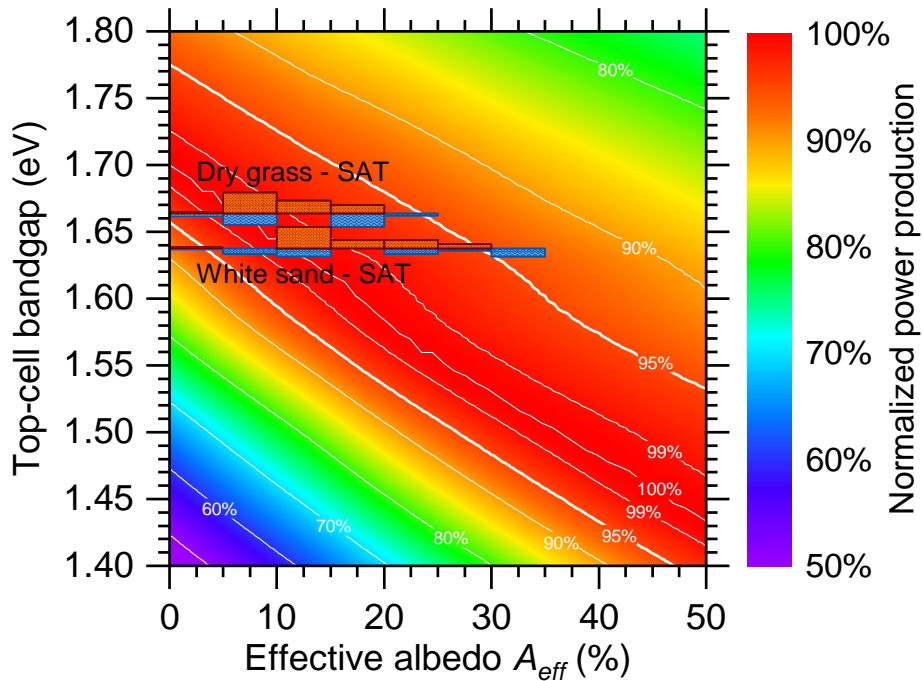
Figure 7.3. Power production of a bifacial tandem module as a function of the top-cell bandgap and effective albedo, normalized to the maximum power possible for each effective albedo. The two widest effective albedo distributions overlaid, with their abscissae at the corresponding optimal top-cell bandgap for the combined clear and cloudy days.

7.3.3 Daily Energy Production of Bifacial versus Monofacial Tandems under Realistic Conditions

Figure 7.4 shows the daily energy production as a function of the top-cell bandgap for bifacial and monofacial tandems. Although the maximum gain in energy production for bifacial tandems—relative to their monofacial cousins—is comparatively small (3.2% to 6.0% for SAT systems, 6.8% to 14.2% for fixed-tilt systems), the gains are present for a broad range of top-cell bandgaps, greatly widening the window of top-cell absorber candidates that can be successfully paired with silicon. In particular, in all cases presented here, the gains from bifaciality overcome the extra losses from current mismatch, even when the tandem is optimized for monofacial use. From our simple, static sensitivity analysis under AM1.5G irradiance, we predict this to be true for any system with A_{eff} >4% on average, which is very low. For A_{eff} <4%, losses from poor light trapping in the bottom cell and sub-cell current mismatch outweigh the gains from bifaciality.

97
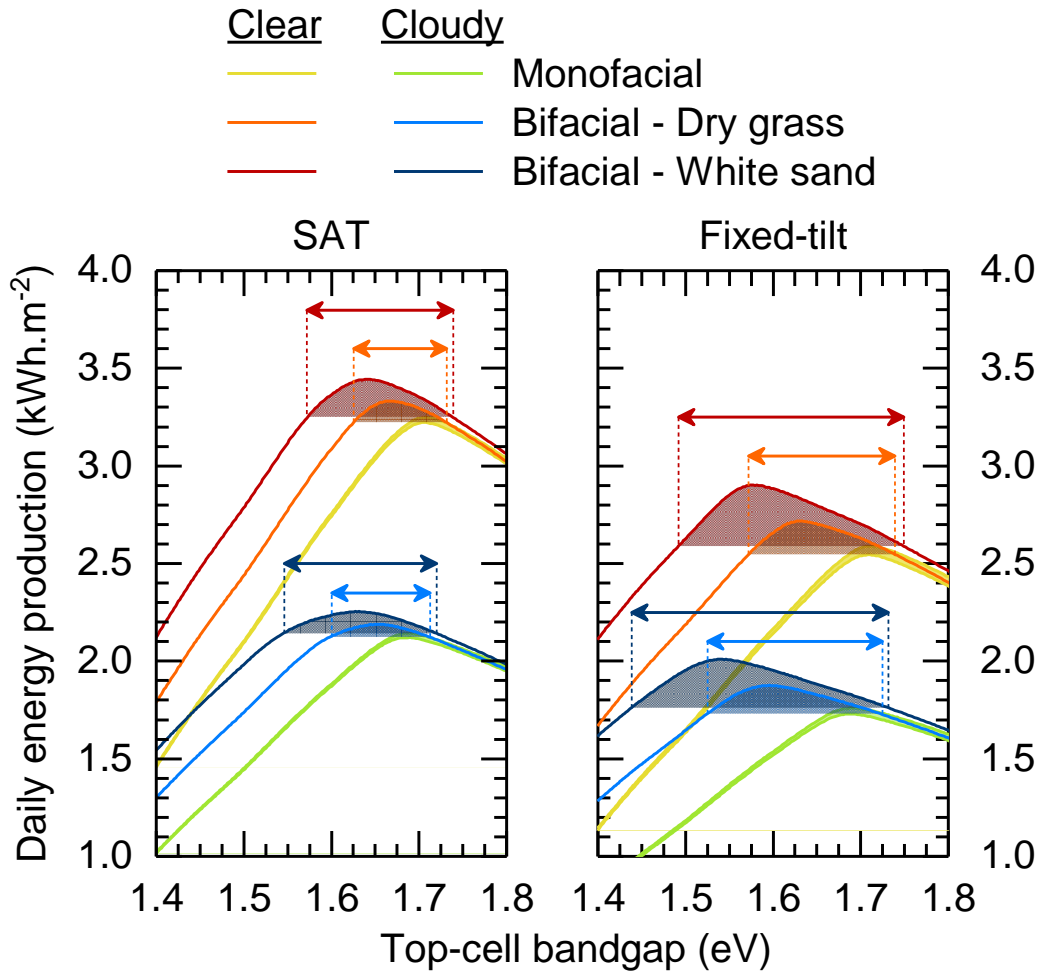
Figure 7.4. Daily energy production as a function of the top-cell bandgap for bifacial tandems on dry grass and white sand, versus the respective monofacial tandems. Each shaded area corresponds to the window of top-cell bandgaps for which the bifacial tandem produces more energy than the optimized monofacial tandem. The thickness of the monofacial curves comes from the slight variation in energy production—due to the difference in albedo—between dry grass and white sand simulations.

Additionally, the width of this appropriate-bandgap window depends mostly on the effective albedo; the ground type matters more than the weather. However, in the SAT case, the top-cell bandgap window only reaches down to 1.55 eV—the bandgap of MAPI—in the *best*-case scenario (white sand, cloudy day). The bandgap window becomes sizably wider for fixed-tilt systems, although the energy production is then considerably lower. Consequently, for utility-scale systems, which are nearly all SAT, transitioning from monofacial to bifacial tandem cell designs

98

is unlikely to end the search for excellent top-cell absorber candidates with bandgaps wider than 1.6 eV. Bifacial tandems with relatively narrow-bandgap top cells could, however, be excellent candidates for non-tracked applications, such as commercial systems on flat rooftops or carports with high-albedo surfaces (e.g. white roofs, concrete parking lots).

7.4   Conclusions

Under realistic conditions, the optimal top-cell bandgap in bifacial tandems decreases with increasing effective albedo. However, in none of the single-axis tracking scenarios investigated is the effective albedo high enough to drop the optimal top-cell bandgap to the 1.40–1.55 eV range where mature or maturing technologies (e.g. GaAs, CdTe, MAPI) are available. Nevertheless, even when unoptimized, bifacial tandems produce more energy than their *optimized* monofacial counterparts for a wide range of top-cell bandgaps, provided that the effective albedo exceeds only 4%. Moreover, the impact of variations in effective albedo throughout the day is minimal, as the power production of tandems is relatively insensitive to small current mismatches. As a result, similar to standard bifacial single-junction c-Si cells, the question resides in the resource and its availability rather than in the technology itself: in the right locations, the gains from bifaciality outweigh the losses from current mismatch and decreased light trapping in the bottom c-Si cell. The best locations for bifacial modules, whether single-junction or tandem, are places with high albedo *and* high fractions of diffuse irradiance. The second requirement points to regions with lower total irradiance, which happens to be where much of the PV market is presently expanding and where fixed-tilt systems still dominate. [76]

There are several opportunities to further expand upon the simulations presented here. Extending the analysis from two representative days to an entire year in multiple locations would give color to the picture we painted. As we have shown, the impact of the effective albedo and of

99

the spectral mismatch can be treated independently with separate models without strongly compromising the accuracy of the simulations. Developing smart modelling tools—such as the clustering of spectral variations presented by Ripalda *et al*. [77]— and combining them with our approach would allow rapid determination of the benefits of bifacial tandems under a wide range of conditions, such as with varying location and ground surface. The question of the impact of inhomogeneities across the modules in a bifacial tandem power plant—in particular due to edge effects—also needs to be addressed. Finally, other system architectures should be investigated, like commercial system on rooftops and on carports.

CONCLUSION

Bifacial PV technology is growing fast, and the industry is adapting to it. This requires rethinking about most of the knowledge we have for monofacial PV systems to be able to modify and apply it to the bifacial products and system designs. Performance modeling is a crucial part of this process.

A benchmark and validation work between major bifacial PV models were performed and it was shown that the raytracing models can model the backside irradiance very accurately at the expense of high computation time and are able to model the impact of racking systems and backside spatial irradiance nonuniformity. On the other hand, view factors models such as bifacialvf, PVsyst and pvfactors have larger errors but they are faster and are good options for modeling large bifacial PV systems.

A set of RADIANCE simulations to study the effect of tilt angle, module height above the ground, albedo, and size of the system on the performance of south-facing bifacial PV systems was performed. We showed the impact of installation parameters on energy yield and bifacial gain for representative days around the summer solstice, fall equinox and winter solstice. We showed that modules installed at the highest possible albedo with high enough clearance from the ground, have higher production. The dependence of the system's energy yield on the albedo is linear with a good approximation. However, we observed a saturating increase in the dependence of the energy yield on the height of the PV system. Unlike albedo and the height, the dependence of the system's performance on the tilt angle is more complicated. Seasonal optimum tilt angles are dependent on other parameters such as height, albedo, size of the system, and time of the year and are usually higher for modules installed closer to the ground. We are the first modeling study to demonstrate that the system size is an important factor that impacts the performance of bifacial PV arrays. Prior

101

published studies focused on either single PV modules or very small systems. Three different-sized systems were modeled, and their performance was compared. We found that for large-scale, south-facing bifacial systems, the optimum tilt angle is usually higher and can be up to 20° more than that for smaller systems. We also observed that energy yield of the center module in a large array can decrease up to 7% (relative to single module system) with a ground albedo of 21%. We also are the first modeling study to definitively demonstrate and quantify the effect of racking material on reducing bifacial performance. We developed a quantitative method for evaluating system performance with and without the effects of racking. We also developed a similar method to identify the source of anomalously high backside irradiance as arising from reflections from the front side of modules in other rows.

In the next work, using RADIANCE raytracing software, we modeled a bifacial PV module with two orientations: optimally tilted facing south/north ($Bi_{S/N}$) and vertically installed facing east/west ($Bi_{E/W}$). We compared the annual energy yield of the two systems under no-shading condition for different locations and observed that $Bi_{S/N}$ module had higher energy yield than $Bi_{E/W}$ for all locations except for Singapore (latitude of 1.17º) for which $Bi_{E/W}$ outperformed $Bi_{S/N}$. Due to very low tilt angle of the module, self-shading effect was very large for this location. We also investigated the performance of two systems under shading conditions caused by horizon obstructions. We assume cubic shape obstruction to simulate buildings around the modules especially in urban areas. We considered two locations of Albuquerque, NM and Anchorage, AK for this purpose. We found out that for a sunnier and lower latitude location such as Albuquerque, only very large obstruction (with respect to the module's view) can cause $Bi_{E/W}$ to have higher energy yield than $Bi_{S/N}$. On the other hand, for a higher latitude location such as Anchorage, even with much smaller obstructions (elevation angle of ~20°) $Bi_{E/W}$ modules performs better than $Bi_{S/N}$.

102

In this study we didn't consider different losses such as soiling and shading that PV system may experience. It has been shown that vertical modules have much less soiling and shading losses which means if under some conditions, $Bi_{E/W}$ and $Bi_{S/N}$ receive same amount of irradiance, $Bi_{E/W}$ would be better option because it will have lower soiling and shading losses.

As a collaborative project between Arizona State University and University of Iowa, we modeled the performance of bifacial tandem PV systems. The work was performed firstly by RADIANCE modeling of the utility-scale bifacial PV systems. The irradiance output from this raytracing model was used as input to a custom tandem-device model to compute predicted power output of the tandem bifacial PV systems. Results suggested that while the energy gain from bifacial tandem systems is not high, range of suitable top-cell bandgaps is greatly broadened. Therefore, more options for top-cell absorber are introduced.

During this project I contributed software solutions to bifacial_radiance, an open source software project that added capabilities to simulate bifacial PV systems with detailed irradiance monitoring. I also validated this simulation tool by modeling various systems with different configuration and orientation and comparing the modeled values to measured irradiance values at these sites. This software is currently being used by other researchers in the PV community.

REFERENCES

[1]   A. Luque, A. Cuevas, and J. M. Ruiz, "Double-sided n+-p-n+ solar cell for bifacial concentration," *Solar Cells,* vol. 2, no. 2, pp. 151-166, 1980/10/01/ 1980.

[2]   C. Reise and A. J. P. s. E. Schmid, Hamburg, Germany, "Realistic yield expectations for bifacial PV systems–An assessment of announced, predicted and observed benefits," vol. 1175, 2015.

[3]   N. Ishikawa and S. Nishiyama, "World First Large Scale 1.25MW Bifacial PV Power Plant on Snowy Area in Japan," presented at the 3rd bifi PV workshop, Miyazaki, Japan, 2016. Available: http://bifipv-workshop.com/fileadmin/images/bifi/miyazaki/presentations/3_1_3_-_ISHIKAWA_-_World_1st_large_scale_Bifacial_PV_power_plant.pdf

[4]   W. J. Cole *et al.*, "SunShot 2030 for Photovoltaics (PV): Envisioning a Low-cost PV Future,"; National Renewable Energy Lab. (NREL), Golden, CO (United States)NREL/TP-6A20-68105 United States 10.2172/1392206 NREL English, 2017, Available: https://www.osti.gov/servlets/purl/1392206.

[5]   R. Guerrero-Lemus, R. Vega, T. Kim, A. Kimm, and L. E. Shephard, "Bifacial solar photovoltaics – A technology review," *Renewable and Sustainable Energy Reviews,* vol. 60, pp. 1533-1549, 2016/07/01/ 2016.

[6]   F. Toor, E. Cahill, C. Liu, M. Feinstein, J. Melnick, and K. See, "Continuing education: going back to school for photovoltaic innovation. State of the Market Report. ," Lux Research2013.

[7]   R. Kopecek and J. Libal, "Towards large-scale deployment of bifacial photovoltaics," *Nature Energy,* vol. 3, no. 6, pp. 443-446, 2018/06/01 2018.

[8]   ITRPV, "International Technology Roadmap for Photovoltaic (ITRPV) 2018 Results," March 2019.

[9]   A. G. Martin and M. J. Keevers, "Optical properties of intrinsic silicon at 300 K," *Progress in Photovoltaics: Research and Applications,* vol. 3, 1995.

[10]   G. Bauer, "Absolutwerte der optischen Absorptionskonstanten von Alkalihalogenidkristallen im Gebiet ihrer ultravioletten Eigenfrequenzen," *Annalen der Physik,* vol. 411, no. 4, 1934.

[11]   L. B. William, G. C. Michael, B. H. Cynthia, and A. L. Israel, "United States Patent: 4137123 - Texture etching of silicon: method," 1979.

[12]   P. Campbell and A. G. Martin, "Light trapping properties of pyramidally textured surfaces," *Journal of Applied Physics,* vol. 62, no. 1, 1987.

[13]   P. Campbell and A. G. Martin, "High performance light trapping textures for monocrystalline silicon solar cells," *Solar Energy Materials and Solar Cells,* vol. 65, no. 1-4, 2001.

[14]   C.-H. Lin, S.-P. Hsu, and H. Wei, "Silicon Solar Cells: Structural Properties of Ag-Contacts/Si-Substrate," 2011.

[15]   B. Yang and M. Lee, "Mask-free fabrication of inverted-pyramid texture on single-crystalline Si wafer," *Optics & Laser Technology,* vol. 63, pp. 120-124, 2014/11/01/ 2014.

[16]   B. B. Pannebakker, A. C. de Waal, and W. G. J. H. M. van Sark, "Photovoltaics in the shade: one bypass diode per solar cell revisited," vol. 25, no. 10, pp. 836-849, 2017.

[17]   S. Y. Guo, T. M. Walsh, and M. Peters, "Vertically mounted bifacial photovoltaic modules: A global analysis," (in English), *Energy,* Article vol. 61, pp. 447-454, Nov 2013.

[18]   T. Dullweber *et al.*, "Bifacial PERC+ solar cells: status of industrial implementation and future perspectives," presented at the 4th Bifi PV Workshop, Konstanz, Germany, 2017.

[19]   A. W. Blakers, A. Wang, A. M. Milne, J. Zhao, and M. A. Green, "22.8% efficient silicon solar cell," vol. 55, no. 13, pp. 1363-1365, 1989.

[20]   W. Cai *et al.*, "22.2% Efficiency n-type PERT Solar Cell," *Energy Procedia,* vol. 92, pp. 399-403, 2016/08/01/ 2016.

[21]   D. Habermannn, "HJT Cost structure and market potential," presented at the 2014 Bifacial PV Workshop, Chambery, France, 2014.

[22]   R. Satpathy, "Additional Energy yield using Bifacial Solar PV Modules & dependency on Albedo,"   Available: https://www.ises.org/sites/default/files/webinars/Presentation%20Rabi%20Satpathy_ISESWebinar_0.pdf.

[23]   T. P. Chang, "The Sun's apparent position and the optimal tilt angle of a solar collector in the northern hemisphere," *Solar Energy,* vol. 83, no. 8, pp. 1274-1284, 2009/08/01/ 2009.

[24]   P. Talebizadeh, M. A. Mehrabian, and M. Abdolzadeh, "Determination of Optimum Slope Angles of Solar Collectors Based on New Correlations," *Energy Sources, Part A: Recovery, Utilization, and Environmental Effects,* vol. 33, no. 17, pp. 1567-1580, 2011/05/23 2011.

[25]   M. Z. Jacobson and V. Jadhav, "World estimates of PV optimal tilt angles and ratios of sunlight incident upon tilted and tracked PV panels relative to horizontal panels," *Solar Energy,* vol. 169, pp. 55-66, 2018/07/15/ 2018.

[26]   E. Lorenzo, L. Narvarte, and J. Muñoz, "Tracking and back-tracking," vol. 19, no. 6, pp. 747-753, 2011.

[27]   S. Bhaduri and A. Kottantharayil, *Mitigation of Soiling by Vertical Mounting of Bifacial Modules*. 2018, pp. 1-5.

[28]   R. Kopecek and J. Libal, "Bifacial PV world 2018," presented at the bifi PV Workshop, Denver, USA, 2018.

[29]   "Sun path chart program," ed: University of Oregon Solar Radiation Monitoring Laboratory.

[30]   S. Wilcox and W. Marion, "Users Manual for TMY3 Data Sets (Revised),"; National Renewable Energy Lab. (NREL), Golden, CO (United States)NREL/TP-581-43156; TRN: US200812%%435 United States 10.2172/928611 TRN: US200812%%435 NREL English, 2008, Available: https://www.osti.gov/servlets/purl/928611.

[31]   M. Hiroshi, U.S. Patent 3,278,811, 1966.

[32]   R. Lal, *Encyclopedia of soil science*. New York: Marcel Dekker, 2002.

[33]   T. C. R. Russell, R. Saive, A. Augusto, S. G. Bowden, and H. A. Atwater, "The Influence of Spectral Albedo on Bifacial Solar Cells: A Theoretical and Experimental Study," *IEEE Journal of Photovoltaics,* vol. 7, no. 6, pp. 1611-1618, 2017.

[34]   L. Kreinin, N. Bordin, A. Karsenty, A. Drori, D. Grobgeld, and N. Eisenberg, "PV module power gain due to bifacial design. Preliminary experimental and simulation data," in *2010 35th IEEE Photovoltaic Specialists Conference*, 2010, pp. 002171-002175.

[35]   G. J. Ward, "The RADIANCE lighting simulation and rendering system," presented at the Proceedings of the 21st annual conference on Computer graphics and interactive techniques, 1994.

[36] C. Deline, S. MacAlpine, B. Marion, F. Toor, A. Asgharzadeh, and J. S. Stein, "Evaluation and field assessment of bifacial photovoltaic module power rating methodologies," in *2016 IEEE 43rd Photovoltaic Specialists Conference (PVSC)*, 2016, pp. 3698-3703.

[37] A. Lindsay *et al.*, "Enhanging bifacial PV modeling with ray-tracing," presented at the 6th PVPMC Workshop, Freiburg, Germany, 2016. Available: https://www.slideshare.net/sandiaecis/enhanging-bifacial-pv-modeling-with-raytracing

[38] "SunSolve," ed: PV Lighthouse.

[39] C. K. Lo, Y. S. Lim, and F. A. Rahman, "New integrated simulation tool for the optimum design of bifacial solar panel with reflectors on a specific site," *Renewable Energy,* vol. 81, pp. 293-307, 2015/09/01/ 2015.

[40] R. Perez, R. Seals, and J. Michalsky, "All-weather model for sky luminance distribution - preliminary configuration and validation," (in English), *Solar Energy,* Article vol. 50, no. 3, pp. 235-245, Mar 1993.

[41] D. Robinson and A. Stone, "Irradiation modelling made simple: the cumulative sky approach and its applications," in *Proccedings PLEA 2004*, Eindhoven, Netherlands, vol. 2, pp. 1255-59.

[42] S. Ayala Pelaez, *Bifacial Solar Panels System Design, Modeling, and Performance*. The University of Arizona.

[43] B. Marion *et al.*, *A Practical Irradiance Model for Bifacial PV Modules: Preprint* (Conference: Presented at 2017 IEEE 44th Photovoltaic Specialists Conference (PVSC), Washington, DC, 25-30 June 2017). ; National Renewable Energy Lab. (NREL), Golden, CO (United States), 2017, p. Medium: ED; Size: 1.1 MB.

[44] C. Hansen *et al.*, *A Detailed Model of Rear-Side Irradiance for Bifacial PV Modules* (Conference: Proposed for presentation at the 44th IEEE Photovoltaic Specialist Conference held June 25-30, 2017 in Washington, DC.). ; Sandia National Lab. (SNL-NM), Albuquerque, NM (United States), 2017, p. Medium: ED; Size: 6 p.

[45] A. Mermoud and B. Wittmer, "Bifacial shed simulations with PVsyst," presented at the Bifacial Workshop 2017, Konstanz, Germany, 25-26.10.2016,

[46] M. A. Anoma, D. Jacob, B. C. Bourne, J. A. Scholl, D. M. Riley, and C. W. Hansen, "View Factor Model and Validation for Bifacial PV and Diffuse Shade on Single-Axis Trackers," presented at the 44th IEEE PVSC Washington, DC, 2017.

[47] B. Zhao, X. Sun, M. R. Khan, and M. A. Alam, "Purdue University Bifacial Module Calculator (PUB)," ed, 2018.

[48] J. E. Castillo-Aguilella and P. S. Hauser, "Multi-Variable Bifacial Photovoltaic Module Test Results and Best-Fit Annual Bifacial Energy Yield Model," (in English), *Ieee Access,* Article vol. 4, pp. 498-506, 2016.

[49] SolarWorld. *CALCULATING THE ADDITIONAL ENERGY YIELD OF BIFACIAL SOLAR MODULES*. Available: http://www.solarworld-usa.com/~/media/www/files/white-papers/calculating-additional-energy-yield-through-bifacial-solar-technology-sw9002us.pdf

[50] M. Kutzer *et al.*, *Ertragssteigerung durch bifaciale Modultechnologie*. 2016.

[51] M. Farrag, D. Mathew, R. C, R. Muthu, Y. Wang, and K. Busawon, *An improved optimization technique for estimation of solar photovoltaic parameters*. 2017, pp. 116-124.

[52] D. S. H. Chan and J. C. H. Phang, "Analytical methods for the extraction of solar-cell single- and double-diode model parameters from I-V characteristics," *IEEE Transactions on Electron Devices,* vol. 34, no. 2, pp. 286-293, 1987.

106

[53]   B. E. Meyers and M. A. Mikofski, "PVMismatch Free Open Source Software," presented at the 8th PV PMC Workshop, Albuquerque, NM May 9th, 2017,

[54]   J. A. Jakubiec and C. F. Reinhart, "Assessing Disability Glare Potential of Reflections from New Construction: Case Study Analysis and Recommendations for the Future," *Transportation Research Record,* vol. 2449, no. 1, pp. 114-122, 2014/01/01 2014.

[55]   I. Reda, "Method to Calculate Uncertainty Estimate of Measuring Shortwave Solar Irradiance using Thermopile and Semiconductor Solar Radiometers,"; National Renewable Energy Lab. (NREL), Golden, CO (United States)NREL/TP-3B10-52194; TRN: US201117%%40 United States 10.2172/1021250 TRN: US201117%%40 NREL English, 2011, Available: https://www.osti.gov/servlets/purl/1021250.

[56]   U. A. Yusufoglu, T. M. Pletzer, L. J. Koduvelikulathu, C. Comparotto, R. Kopecek, and H. Kurz, "Analysis of the Annual Performance of Bifacial Modules and Optimization Methods," (in English), *Ieee Journal of Photovoltaics,* Article vol. 5, no. 1, pp. 320-328, Jan 2015.

[57]   L. Kreinin, A. Karsenty, D. Grobgeld, and N. Eisenberg, "PV systems based on bifacial modules: Performance simulation vs. design factors," in *2016 IEEE 43rd Photovoltaic Specialists Conference (PVSC)*, 2016, pp. 2688-2691.

[58]   A. Asgharzadeh, B. Marion, C. Deline, C. Hansen, J. S. Stein, and F. Toor, "A Sensitivity Study of the Impact of Installation Parameters and System Configuration on the Performance of Bifacial PV Arrays," *IEEE Journal of Photovoltaics,* vol. 8, no. 3, pp. 798-805, 2018.

[59]   J. Galtieri and P. T. Krein, "Designing solar arrays to account for reduced performance from self-shading," in *2015 IEEE Power and Energy Conference at Illinois (PECI)*, 2015, pp. 1-8.

[60]   *National Solar Radiation Data Base (NSRDB).* Available: https://nsrdb.nrel.gov/nsrdb-viewer

[61]   "PV_LIB," ed: Sandia National Laboratories.

[62]   P. Ineichen and R. Perez, "A new airmass independent formulation for the Linke turbidity coefficient," *Solar Energy,* vol. 73, no. 3, pp. 151-157, 2002, Art. no. Pii s0038-092x(02)00045-2.

[63]   R. Perez *et al.*, "A new operational model for satellite-derived irradiances: Description and validation," (in English), *Solar Energy,* Article vol. 73, no. 5, pp. 307-317, 2002, Art. no. Pii s0038-092x(02)00122-6.

[64]   J. A. Jakubiec and C. F. Reinhart, "Assessing Disability Glare Potential Due to Reflections from New Constructions: A Case Study Analysis and Recommendations for the Future," in *2014 Annual Meeting of the Transportation Research Board*, 2014.

[65]   H. R. Ghosh, N. C. Bhowmik, and M. Hussain, "Determining seasonal optimum tilt angles, solar radiations on variously oriented, single and double axis tracking surfaces at Dhaka," *Renewable Energy,* vol. 35, no. 6, pp. 1292-1297, 2010/06/01/ 2010.

[66]   M. C. Peel, B. L. Finlayson, and T. A. McMahon, "Updated world map of the Koppen-Geiger climate classification," (in English), *Hydrology and Earth System Sciences,* Article vol. 11, no. 5, pp. 1633-1644, 2007.

[67]   X. S. Sun, M. R. Khan, C. Deline, and M. A. Alam, "Optimization and performance of bifacial solar modules: A global perspective," (in English), *Applied Energy,* Article vol. 212, pp. 1601-1610, Feb 2018.

[68] S. L. Salzberg, "C4.5: Programs for Machine Learning by J. Ross Quinlan. Morgan Kaufmann Publishers, Inc., 1993," *Machine Learning,* journal article vol. 16, no. 3, pp. 235-240, September 01 1994.

[69] E. Frank *et al.*, *Weka-A Machine Learning Workbench for Data Mining* (Data Mining and Knowledge Discovery Handbook, Second Edition). New York: Springer, 2010, pp. 1269-1277.

[70] N. Bouaouadja, S. Bouzid, M. Hamidouche, C. Bousbaa, and M. Madjoubi, "Effects of sandblasting on the efficiencies of solar panels," (in English), *Applied Energy,* Article; Proceedings Paper vol. 65, no. 1-4, pp. 99-105, Jan-Apr 2000.

[71] H. K. Hajjar, F. A. Dubaikel, I. M. Ballard, and Ieee, *Bifacial Photovoltaic Technology for the Oil and Gas Industry* (2015 Saudi Arabia Smart Grid Conference). New York: Ieee, 2015.

[72] H. Lu, L. Lu, and Y. H. Wang, "Numerical investigation of dust pollution on a solar photovoltaic (PV) system mounted on an isolated building," (in English), *Applied Energy,* Article vol. 180, pp. 27-36, Oct 2016.

[73] A. M. Baldridge, S. J. Hook, C. I. Grove, and G. Rivera, "The ASTER spectral library version 2.0," *Remote Sensing of Environment,* vol. 113, no. 4, pp. 711-715, 2009/04/15/ 2009.

[74] S. C. Baker-Finch and K. R. McIntosh, "A freeware program for precise optical analysis of the front surface of a solar cell," in *35th IEEE Photovoltaic Specialists Conference*, Honolulu, HI, USA, 2010, pp. 2184-2187.

[75] A. Onno, N. P. Harder, L. Oberbeck, and H. Y. Liu, "Simulation study of GaAsP/Si tandem solar cells," (in English), *Solar Energy Materials and Solar Cells,* vol. 145, pp. 206-216, Feb 2016.

[76] M. Bolinger and J. Seel, "Utility-Scale Solar - Empirical Trends in Project Technology, Cost, Performance, and PPA Pricing in the United States " Lawrence Berkeley National Laboratory2018.

[77] J. M. Ripalda, J. Buencuerpo, and I. Garcia, "Solar cell designs by maximizing energy production based on machine learning clustering of spectral variations," (in English), *Nature Communications,* vol. 9, no. 1, p. 5126, Dec 3 2018.